GENERATION AND CHARACTERIZATION OF SUB-70 ISOLATED ATTOSECOND PULSES

by

QI ZHANG
B.S. University of Science of Technology of China, 2007
M.S. Kansas State University, 2009

A dissertation submitted in partial fulfillment of the requirements
for the degree of Doctor of Philosophy
in the College of Optics & Photonics
at the University of Central Florida
Orlando, Florida

Summer Term
2014

Major Professor: Zenghu Chang

ABSTRACT

Dynamics occurring on microscopic scales, such as electronic motion inside atoms and molecules, are governed by quantum mechanics. However, the Schrödinger equation is usually too complicated to solve analytically for systems other than the hydrogen atom. Even for some simple atoms such as helium, it still takes months to do a full numerical analysis. Therefore, practical problems are often solved only after simplification. The results are then compared with the experimental outcome in both the spectral and temporal domain. For accurate experimental comparison, temporal resolution on the attosecond scale is required. This had not been achieved until the first demonstration of the single attosecond pulse in 2001. After this breakthrough, "attophysics" immediately became a hot field in the physics and optics community.

While the attosecond pulse has served as an irreplaceable tool in many fundamental research studies of ultrafast dynamics, the pulse generation process itself is an interesting topic in the ultrafast field. When an intense femtosecond laser is tightly focused on a gaseous target, electrons inside the neutral atoms are ripped away through tunneling ionization. Under certain circumstances, the electrons are able to reunite with the parent ions and release photon bursts lasting only tens to hundreds of attoseconds. This process repeats itself every half cycle of the driving pulse, generating a train of single attosecond pulses which lasts longer than one femtosecond. To achieve true temporal resolution on the attosecond time scale, single isolated attosecond pulses are required, meaning only one attosecond pulse can be produced per driving pulse.

Up to now, there are only a few methods which have been demonstrated experimentally to generate isolated attosecond pulses. Pioneering work generated single attosecond pulse using a

carrier-envelope phase-stabilized 3.3 fs laser pulse, which is out of reach for most research groups. An alternative method termed as polarization gating generated single attosecond pulses with 5 fs driving pulses, which is still difficult to achieve experimentally. Most recently, a new technique termed as Double Optical Gating (DOG) was developed in our group to allow the generation of single attosecond pulse with longer driving pulse durations. For example, isolated 150 as pulses were demonstrated with a 25 fs driving laser directly from a commercially-available Ti:Sapphire amplifier. Isolated attosecond pulses as short as 107 as have been demonstrated with the DOG scheme before this work. Here, we employ this method to shorten the pulse duration even further, demonstrating world-record isolated 67 as pulses.

Optical pulses with attosecond duration are the shortest controllable process up to now and are much faster than the electron response times in any electronic devices. In consequence, it is also a challenge to characterize attosecond pulses experimentally, especially when they feature a broadband spectrum. Similar challenges have previously been met in characterizing femtosecond laser pulses, with many schemes already proposed and well-demonstrated experimentally. Similar schemes can be applied in characterizing attosecond pulses with narrow bandwidth. The limitation of these techniques is presented here, and a method recently developed to overcome those limitations is discussed.

At last, several experimental advances toward the characterization of the isolated 25 as pulses, which is one atomic unit time, are discussed briefly.

ACKNOWLEDGMENTS

I am blessed to be able to join in this exciting group and it has been a tough and yet fruitful five years for me.

It is very helpful and productive to work with my colleagues. Particularly, Dr. Zenghu Chang is my major advisor and has given me countless useful guidance through my PhD study. I also want to thank Dr. Kun Zhao who introduced me to the research from the beginning and worked with me for many late nights for our best datasets. All my skills and methods to solve problems are almost directly learned from him or heavily affected by the experience of working with him. I also want to thank Dr. Yi Wu who built and maintained the laser—my experiments wouldn't go anywhere without his help; Dr. Michael Chini who gave me a lot of help in understanding physical principles hidden under the experimental data; Yang Wang who worked with me closely in this research project. I also like to thank Dr. Xiaowei Wang, Yan Chen, Jie Li, Huaping Zang, Eric Cunningham for all their kinds of support and helpful discussions. I also worked with Prof. Chaoming Li, Prof. Jianhua Zeng, Xianglin Wang and Peng Xu within the last year of my PhD. I would like to thank them for their work.

I have also been very fortunate to work with several former colleagues during the first couple of years during my PhD period. They are Dr. He Wang, Dr. Steve Gilbertson, Dr. Sabih Khan, Dr. Shouyuan Chen, Dr. Chenxia Yun, and Dr. Baozhen Zhao. They all helped me in one way or another. Their kindness is much appreciated. I also acknowledge the effort and support from the technical support staff at both Kansas State University and University of Central Florida.

I would also like to thank Prof. Peter J. Delfyett, Prof. Romain M. Gaume, and Prof. Haripada Saha for agreeing to serve on my dissertation committee.

I also want to thank my wife Dr. Suhao Han for her understanding and support. We have been long distance for a very long time and I have spent way more time in the laboratory than with her during the last five years. But she has been very patient with me and my work couldn't be done today without her.

Finally, I want to thank my parents in China for their life-long support. I haven't been back to China in almost five years and am deeply owed to them. I would like to acknowledge their spiritual support during my whole life.

TABLE OF CONTENTS

LIST OF FIGURES

LIST OF TABLES

CHAPTER 1 INTRODUCTION

The laser is a device that delivers optical sources in both a spatially- and temporally-coherent manner. Since its first invention in 1960, the advance of laser technology has significantly changed and is still changing peoples' lives [1]–[4]. Due to the coherence of the laser light, it can be compressed in a very small spatial area and an extremely short period, making it an ideal tool for studying microscopic phenomena. Today, the focus of a laser light can reach to a scale of less than one micrometer [5], and the period of a laser pulse can be shorter than one hundred attoseconds (10^{-18} s) [6], [7].

Since a laser source can carry a considerable amount of energy in a very short period and small space, it can be used to alter the status of a microscopic target very quickly. This allows us to observe the dynamics of the target in the temporal domain, as long as the pulse duration of the laser is short enough compared to the target response. Fig 1.1 shows different time scales for different dynamics. For example, laser sources with picosecond duration can be used to study the rotational movement of the atoms inside molecules, as shown in Fig. 1.1 (a). Starting from the 1990s, along with the appearance of several techniques such as mode-locking, sub-100-femtosecond (1 fs = 10^{-15} s) laser sources have become available. They can be used to study fast vibrational modes inside different type of molecules as shown in Fig. 1.1 (b) [8]–[12]. However, femtosecond lasers are usually centered at wavelengths of hundreds of nanometer (nm) (e.g., the widely-used Ti:Sapphire laser has a central wavelength of ~800 nm). Therefore, the shortest laser pulse duration from a Ti:Sapphire is fundamentally limited by one optical cycle, which is 2-3 fs [7], [13], [14]. To reach even shorter pulse durations, one unavoidably needs to operate in the Extreme Ultraviolet (XUV) region.

Most recently, an XUV pulse lasting only hundreds of attosecond was demonstrated [15], symbolizing a breakthrough into the attosecond era. Attosecond pulses can be used to study the electron dynamics inside atomic, molecular and condensed matter systems [16]–[26]. For example, it takes an electron in the ground state of a hydrogen atom about 25 as to orbit once around the proton in the classical picture, as shown in Fig. 1.1 (c).

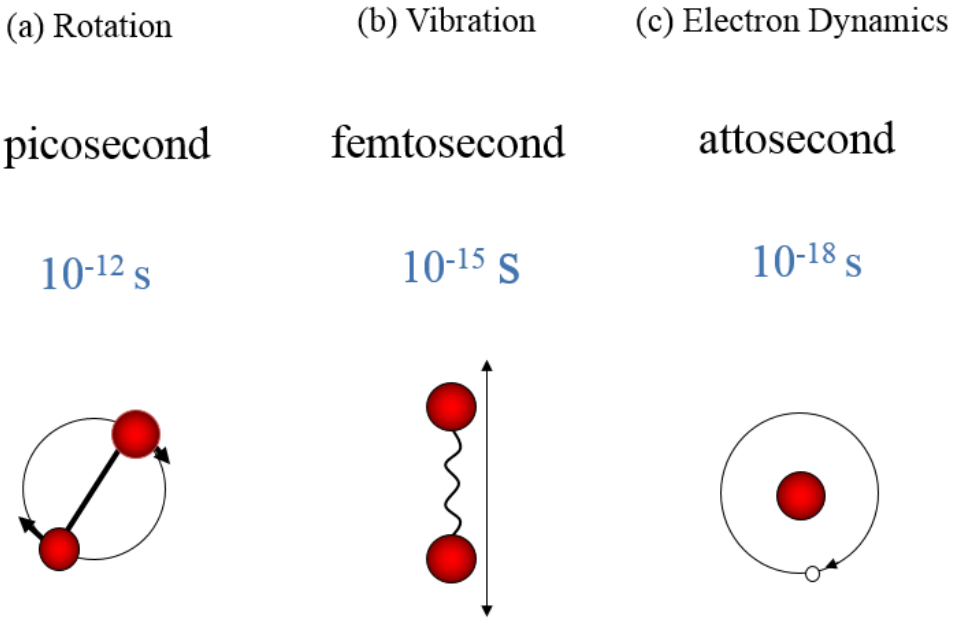

Figure 1.1 Time scale for different dynamics. (a) Picosecond time scale for rotational motion of the atoms inside molecules. (b) Femtosecond time scale for vibrational motion of the atoms inside molecules. (c) Electron dynamics inside atoms.

Unlike commercialized femtosecond or picosecond lasers, an attosecond "laser" source is not a traditionally-defined laser since there is no amplification process. Actually the attosecond source comes from a highly nonlinear process caused by the interaction of an intense electromagnetic field with atoms or molecules, which is termed as High-order Harmonic Generation (HHG) [27]. In order to observe the HHG, the driving field needs a peak intensity

more than 10^{14} W/cm^2. Currently, Ti:Sapphire lasers using Chirped Pulse Amplification (CPA) are widely used due to their relative high pulse energy and short pulse duration [28], [29] .

However, the HHG process repeats itself every half cycle of the driving laser, leading to the generation of a train of attosecond pulse. In order to get true attosecond temporal resolution, a single isolated attosecond pulse is required for, as an example, pump-probe experiments. This is not a straightforward task. Since the first demonstration of the single attosecond pulse, several schemes and techniques have been proposed and demonstrated [7], [30]–[33]. Among them, the Double Optical Gating (DOG) technique proposed recently has been demonstrated experimentally to generate an isolated 130 attosecond pulse [34]. In this work, the implementation of DOG is pushed to another level, generating and characterizing a world record of isolated 67 as pulses [6].

This dissertation will be organized as follows. Chapter 2 introduces the HHG and its mechanism. Chapter 3 explains in detail the principle of DOG and compares it with its counterparts. Chapter 4 focuses on two phase retrieval algorithms for temporal characterization of an attosecond pulse. In Chapter 5, the experimental setup with a high-resolution electron energy spectrometer for attosecond streaking built at the Institute for the Frontier of Attosecond Science and Technology (iFAST) is introduced, and simulations on the spectrometer resolution are compared with experimental results. Chapter 6 presents the experimental results demonstrating the single 67 as pulse. In Chapter 7, some of the most recent progress towards the generation of isolated 25 as pulses is discussed. Finally in Chapter 8, a summary of the chapters is given, and paths for future work are brought up for consideration.

CHAPTER 2 HIGH-ORDER HARMONIC GENERATION

High-order harmonic generation was first observed in the late 1980s [27], much earlier than the first demonstration of single attosecond pulses. A laser with 1067 nm and 50 picosecond duration was focused on an argon gas target, and a series of odd harmonics of the driving laser were then observed. The experimental result, obviously differing from the prediction of perturbation theory, was well explained by the so-called “Three Step Model” brought up in 1993 by Corkum [35]. This model separates the HHG process into three steps: first, the valence electrons from neutral atoms are tunnel-ionized by the strong electric field of the laser; second, the free electrons are then accelerated by the laser field; finally, under certain circumstances the electrons return and recombine with parent ions. The kinetic energy gained during the accelerating process is then released in the form of photon. A schematic drawing is shown in Fig. 1.1(a).

Due to the non-perturbative nature of this process, the harmonic spectrum from the HHG usually shows a relative flat area called the “plateau” after the first several orders drop quickly in intensity [36], [37]. After the plateau, the signal drops quickly again and this area is termed the “cutoff” of the HHG. The schematic drawing of the HHG can be seen in Fig. 1.1 (b). The cutoff is the highest energy that the XUV photon can reach, hence limiting the bandwidth of the final attosecond pulse. A broadband spectrum is not the only requirement to achieve short pulse durations: additionally, minimal spectral dispersion is also needed. The intrinsic chirp of the attosecond pulse from the HHG process is also calculated in this chapter.

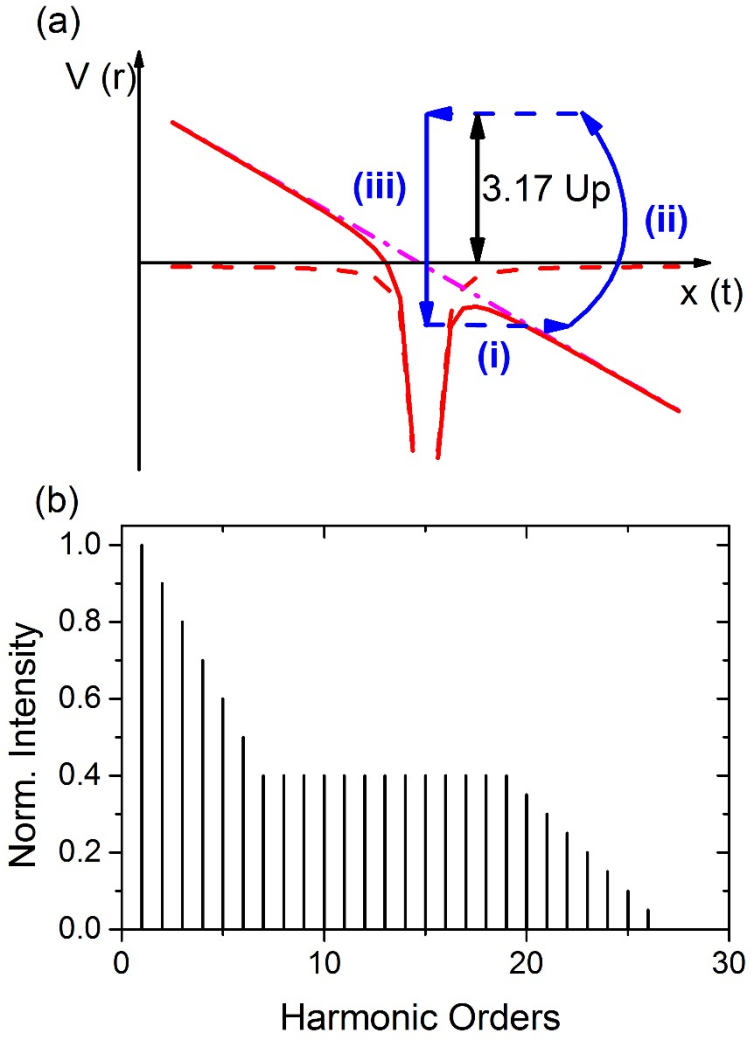

Figure 2.1(a) A schematic drawing illustrating the three step model (i) Tunnel ionization. (ii) Acceleration by the driving field. (iii) Recombination with the parent ion. (b) A schematic plot of a typical intensity spectrum from high-order harmonic generation.

2.1 The Three Step Model

For a simple discussion, a linearly-polarized, plane-wave driving laser is considered here. Assuming the electric field is polarized in the x-axis direction, its electric field at a given spatial point can be expressed by

$$\varepsilon(t) = E_0 \cos(\omega_0 t) \qquad (2.1)$$

We further assume that in the first step, the ground state electron tunnels through the potential barrier instantaneously. After the tunneling, the electron can be treated as a free electron following classical mechanics. The Coulomb potential of the parent ion can be ignored, as long as the Keldysh parameter $\gamma = \sqrt{\frac{2I_p m{\omega_0}^2}{e^2 E_0^2}}$ is less than 1 [38]. For our home-built Ti:Sapphire CPA system centered at 750 nm with 7 fs pulse duration and 1 mJ energy, the angular frequency ω_0 is $6.4 \times 10^{13}\ rad/s$, the ionization potential I_p is 21.5 eV for neon, the electric field amplitude E_0 is estimated to be $8.7 \times 10^{10}\ V/m$ corresponding to a peak intensity of $1 \times 10^{15}\ W/cm^2$, and e and m are the electron charge and mass respectively The Keldysh parameter γ is calculated to be 0.45, indicating that our parameters fit well within the tunneling region.

The free electron motion is treated classically. Therefore, the acceleration of the tunneled electrons should be

$$\frac{d^2x}{dt^2} = -\frac{e}{m}\varepsilon(t) = -\frac{e}{m}E_0 \cos(\omega_0 t) \qquad (2.2)$$

.

The equation is then solved for velocity and displacement as a function of time, as seen below:

$$v(t) = \frac{dx}{dt} = -\frac{eE_0}{m\omega_0}[\sin(\omega_0 t) - \sin(\omega_0 t_0)] \qquad (2.3)$$

$$x(t) = \frac{eE_0}{m\omega_0^2}\{[\cos(\omega_0 t) - \cos(\omega_0 t_0)] + \omega_0 sin(\omega_0 t_0)(t - t_0)\} \qquad (2.4)$$

Here, t_0 is the time when the electron is tunnel-ionized. In the third step, the electron recombines with the parent ion and emits a photon. Solve equation 2.4 using $x(t) = 0$ for the time t, and

then plug into equation 2.3. At the end, the released photon energy is the sum of the kinetic energy of the free electron and the ionization potential of the atom:

$$\hbar\omega(t) = I_P + \frac{1}{2}mv^2(t) = I_p + 2U_p[\sin(\omega_0 t) + \sin(\omega_0 t_0)]^2 \qquad (2.5)$$

where U_p is the pondermotive energy defined as

$$U_p = \frac{(eE_0)^2}{4m\omega_0^2}. \qquad (2.6)$$

It can be seen that once the initial t_0 is known, the recombination time as well as the kinetic energy are readily calculated. The relation between the recombination time and ionization time is plotted in Fig 2.2 (a) and the kinetic energy as a function of emission time is plotted in Fig. 2.2 (b).

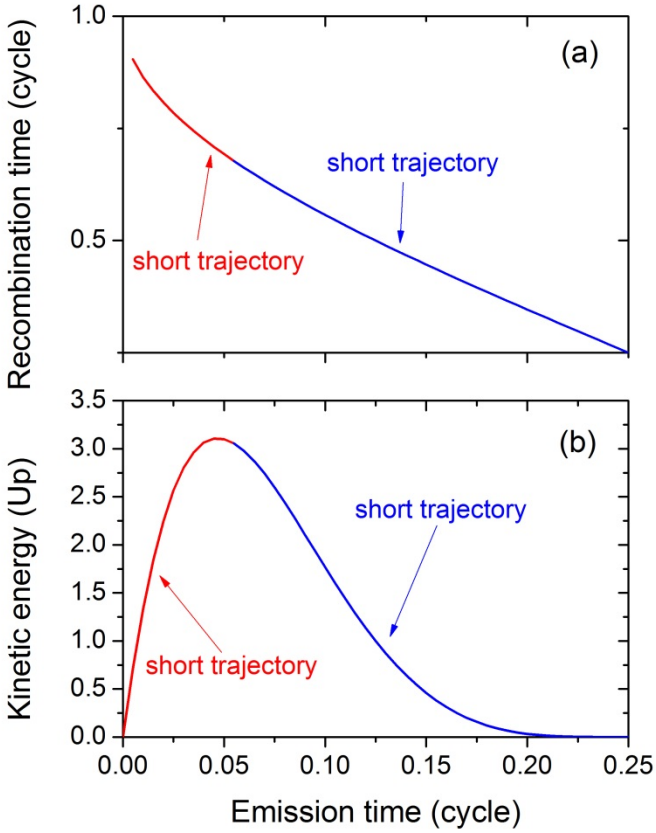

Figure 2.2 Numerically calculated recombination time as a function of the emission time for a tunnel-ionized electron. (b) The kinetic energy of the returned electron before it recombines with the parent ion, as a function of the emission time.

From Fig. 2.2 (b), the maximum kinetic energy is $K_{max} = 3.17U_p$, which is carried by the electron released at $\omega_0 t_0 = 0.05 \times 2\pi$ rad and returns at $\omega_0 t = 0.7 \times 2\pi$. Thus, the HHG cutoff is

$$\hbar\omega_{max} = I_p + 3.17U_p. \quad (2.7)$$

The ponderomotive energy U_p can be simply expressed as:

$$U_P[eV] = 9.33 \times 10^{-14} I_0 \lambda_0^2 \quad (2.8)$$

in which I_0 is the peak intensity of the laser in W/cm^2 and λ_0 is the wavelength of the driving laser in μm. In our cases, if we choose neon as the gas target (I_p=21.5 eV), the peak intensity of $1 \times 10^{15}\ W/cm^2$ and central wavelength of 0.75 μm from a Ti:Sapphire laser , the corresponding cutoff photon energy can be 170 eV. As a reference, the bandwidth required for a transform-limited Gaussian pulse with a Full Width Half Maximum (FWHM) of 25 as is 150 eV!

Moreover, from Fig. 2.2 (b), there are two "paths" to obtain one final kinetic energy. The electron released before 0.05 cycle returns later and electron released after that return earlier, according to the Fig. 2.2 (a). Therefore, the first path is termed as "long trajectory" and the other as "short trajectory". The high-order harmonics from the two trajectories exhibit complete different coherence and diverging angle [39], [40]. The existence of two paths further complicates the single attosecond pulse. Fortunately, the long trajectories can often be suppressed by adjusting phase matching conditions.

To calculate the intrinsic chirp, the kinetic energy as function of recombination time is plotted as below. It can be seen that there is a significant difference between long and short trajectories: the directions of the slope in Fig. 2.3 are opposite to each other, indicating the opposite spectral and temporal chirp for the generated XUV pulse from the two paths. The intrinsic chirp for the short trajectory is calculated from $dt/_{dK(t)}$ and plotted in Fig. 2.4, assuming $1 \times 10^{15}\ W/cm^2$ peak intensity and 0.75 μm central wavelength. It can be seen that the intrinsic chirp is positive for the short trajectory, which is the case in our experiment; therefore, negative material chirp should be applied to compensate the intrinsic chirp for achieving shortest pulse durations. This is very important and will be discussed in more detail in Chapter 6.

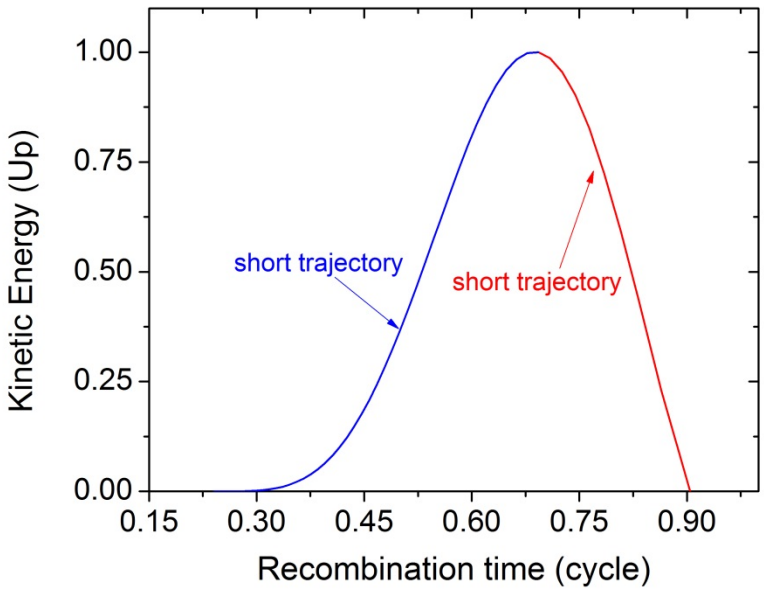

Figure 2.3 The kinetic energy of the recombined electron as a function of recombination time. The short and long trajectories are labeled with blue and red colors separately.

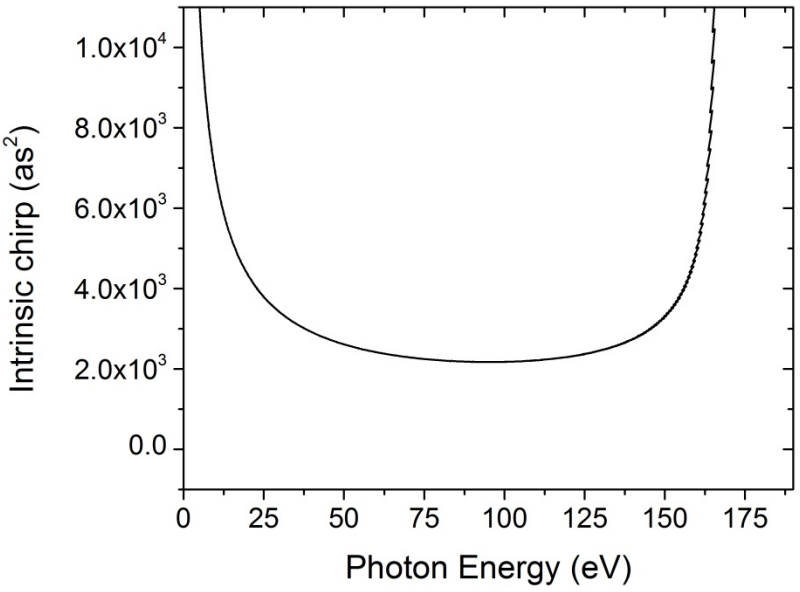

Figure 2.4 The intrinsic chirp as a function of the photon energy for short trajectory only, assuming 0.75 μm central wavelength and assuming $1 \times 10^{15}\ W/cm^2$ peak intensity.

2.2 Attosecond Pulse Train

For a linearly-polarized driving field, the three step process repeat every half cycle. Therefore, a train of attosecond pulses lasting several femtoseconds is directly generated from the HHG [41], [42]. In the spectral domain, this appears as discrete odd-order harmonic peaks. In comparison, a single isolated attosecond pulse corresponds to a supercontinuum spectrum in the XUV region.

A schematic drawing of the experimental configuration for measuring the HHG spectra is shown below in Fig. 2.5. The driving laser is focused on a glass tube filled with neon gas. The interacting length is usually 0.5~2 mm, depending on the experimental goal. A metallic filter such as aluminum with a thickness of 300 nm is used to block the remaining driving field and transmit the XUV pulse. Then the XUV is focused by a toroidal mirror (gold coated, incident angle of 5°) onto a second gas target, which is also typically neon. The photoelectrons of the XUV will then be collected by a Time-Of-Flight (TOF) electron energy spectrometer (not drawn). A hole mirror is used to transmit the XUV pulse when the pump-probe experiment is used.

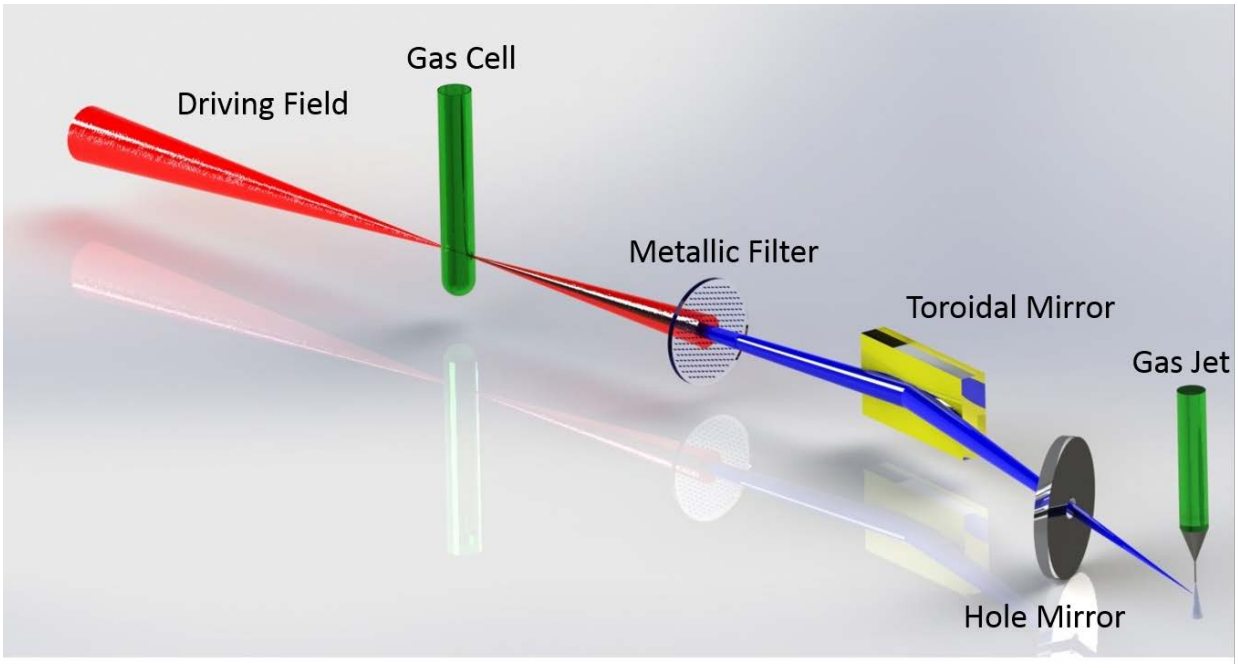

Figure 2.5 Schematic drawing of a typical experimental configuration for generating high-order harmonics and detecting photoelectron spectra.

An experimental photoelectron spectrum of attosecond pulse train is plotted in Fig. 2.6. The driving field is the home-built Ti:Sapphire CPA laser with 1 mJ and 25 fs pulse duration. Neon gas was used for both generation and detection. The details of the setup can be found in Chapter 5.

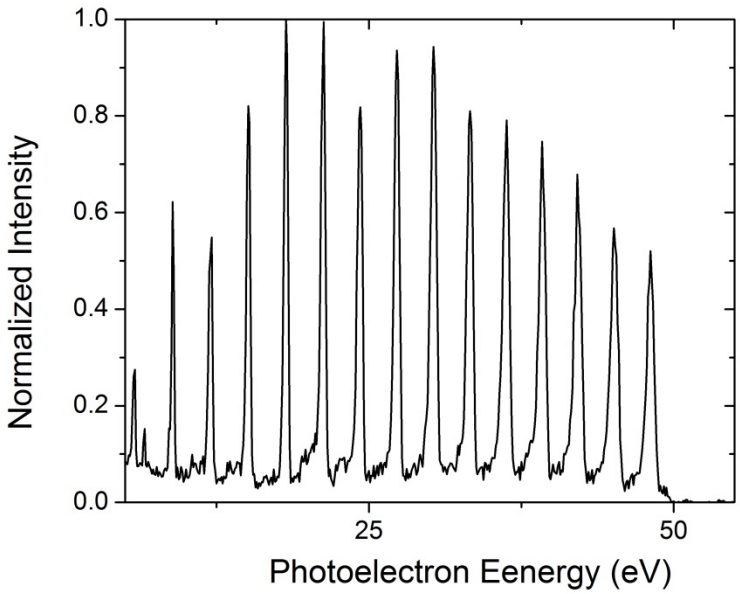

Figure 2.6 Experimental photoelectron spectrum with linearly polarized driving laser (Ti:Sapphire laser with 1 millijoule pulse energy and 25 femtosecond pulse duration). The cutoff at about 50 eV are from Aluminum filter which was used to block the remaining driving field.

Attosecond pulse trains can be very useful in certain scenarios. However, in order to achieve attosecond temporal resolution in pump-probe experiments, single isolated attosecond pulses are needed. In the next chapter, three different schemes for generating single attosecond pulse are explained and compared.

CHAPTER 3 ISOLATED ATTOSECOND PULSES

To obtain single isolated attosecond pulses, the three-step process can only happen once per driving pulse. The most straightforward way is to use a driving pulse of only single-cycle duration. This was done in Ref [7], where a 3.5 fs driving laser was used. Even with such a short pulse, harmonic peaks can still be observed in the low photon energy region. A zirconium filter was applied to filter out the low energy component, and only a single attosecond pulse was transmitted. With this so-called Amplitude Gating (AG) method, 80 as isolated pulses were generated [7]. However, the requirement of AG is extremely difficult to meet. To date, only a few laboratories in the world have demonstrated single attosecond pulse generation with this method. Additionally, since it filters out many low order harmonics, only the cutoff region can contribute to the final single attosecond pulse. It significantly limits the achievable bandwidth for the supercontinuum and hence the pulse duration, since the cutoff region is typically only a small portion of the total high harmonic spectrum.

Another way of solving this problem is to manipulate the ellipticity of the driving electric field. In the last step from the three-step model, the accelerated electron needs to come back and recombine with the parent ion. If ellipticity is introduced to the driving field, the electron can be accelerated in a transverse direction. Therefore, the possibility of recombination is greatly reduced [43]. Experimentally, a significant drop of the HHG signal has been observed along with increasing ellipticity of the driving laser [44]. This opens another way to generate single attosecond pulse without needing single-cycle driving lasers. Two schemes, Polarization Gating (PG) and Double Optical Gating (DOG), have been proposed, and both have been demonstrated experimentally [32], [45]. The PG and DOG not only relax the requirement for the driving laser,

but they can also generate a supercontinuum spectra that covers even the plateau region. Therefore, in this chapter, these two schemes (especially DOG) are explained in detail.

3.1 Few-Cycle Femtosecond Lasers

To drive the generation of isolated attosecond pulses, few-cycle femtosecond lasers, commonly based on Ti:Sapphire, are used. Often Ti:Sapphire is chosen as the gain material due to its long upper-state lifetime, broad gain bandwidth, and high damage threshold. Therefore, in this work a Ti:Sapphire Chirped Pulse Amplification (CPA) system was built and a hollow-core fiber-compressor system was applied to produce about 7 fs, 1 mJ pulse at a 1 kHz repetition rate. A schematic drawing of the whole system is shown below in Fig. 3.1.

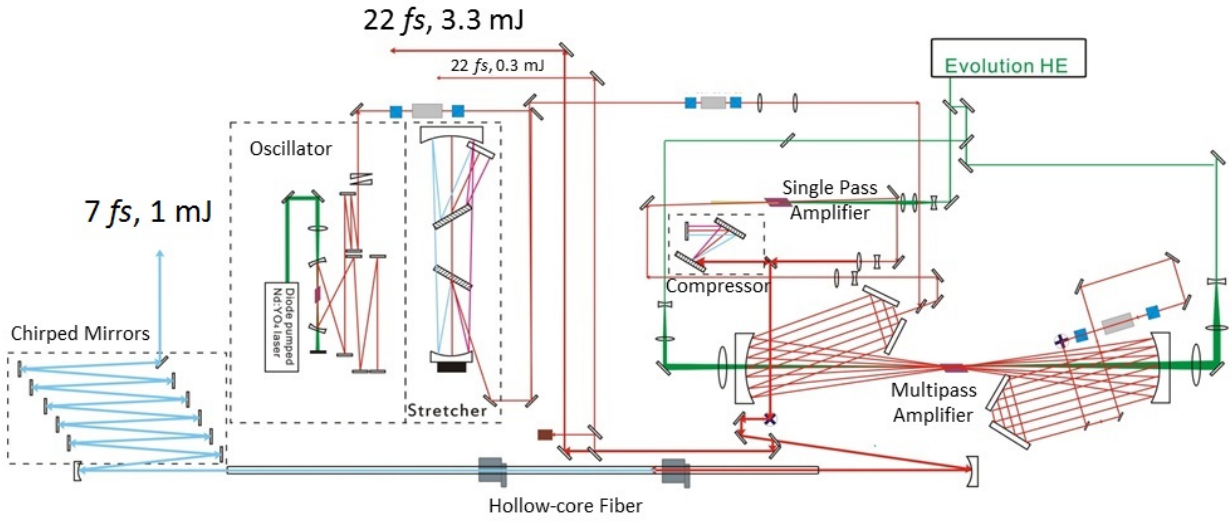

Figure 3.1 Schematic drawing of a Ti:Sapphire few-cycle laser system.

The mode-locked Ti:Sapphire oscillator (Femtolasers Scientific Pro) pumped by a continuous Nd:YVO_4 laser (Coherent Verdi G) at 532 nm produces the 10 fs pulses at around an 80 MHz repetition rate. The pulse energy is about 5 nJ, which is not sufficient for directly exciting the HHG. The oscillator beam then goes through a grating pair which stretches the pulse

duration to ~200 ps. The stretched pulse is then amplified in two stages and reaches a pulse energy of ~5 mJ. Then a grating pair compressor is used to compress the pulse duration to around 25 fs and 3 mJ. The stretcher is used to avoid damaging the Ti:Sapphire crystal during amplification. This technique was invented in early 1980s and is termed as Chirped Pulse Amplification.

To generate isolated attosecond pulses, a few-cycle driving laser should be used. The 25 fs laser pulse from the CPA is focused into a hollow-core fiber filled with neon gas, where its spectrum is broadened by self-phase modulation. The positive chirp of the pulses introduced by this process is compensated by six pairs of chirped mirrors. Finally, around 1 mJ, 7 fs pulses are produced and ready to be used as the driving field in HHG.

The pulse duration of the laser was evaluated by Second-harmonic Frequency Resolved Optical Gating (SHG-FROG) [46]. In SHG-FROG, the input beam is split into two identical pulses which are then recombined in a frequency-doubling crystal. The generated second harmonic beam is then recorded by an imaging spectrometer. The recorded FROG trace is reconstructed with a computer using the Principal Component Generalized Projections Algorithm (PCGPA) [47].

The electric field of a pulse can be written as

$$\varepsilon(t) = E(t)e^{-i\omega t}, \quad (3.1)$$

where E(t) is the complex envelope of the pulse and ω is the carrier frequency of the pulse. Therefore, the complex envelope of the SHG-FROG signal is given by

$$E_{FROG}(t,\tau) = E(t)E(t-\tau), \quad (3.2)$$

where τ is the time delay between the two identical pulses. The FROG trace recorded by the CCD detector can then be expressed as:

$$I_{FROG}(\omega,\tau) = \left|\int_{-\infty}^{\infty} E(t)E(t-\tau)e^{i\omega t}dt\right|^2 \quad (3.3)$$

For a typical FROG, it is not necessary that two identical beams are used. So generally, a FROG trace can be expressed as:

$$I_{FROG}(\omega,\tau) = \left|\int_{-\infty}^{\infty} E(t)G(t)e^{i\omega t}dt\right|^2 \quad (3.4)$$

$E(t)$ is the electric field which needs to be characterized, and $G(t)$ is the gate function, which could be a unknown field. The equation above is important since it will be compared with the atto-streaking trace which is used to characterize the attosecond pulses. Details can be found in Chapter 4.

The FROG trace for the pulse after the hollow-core fiber is shown in Fig. 3.2. The pulse duration used to generate isolated attosecond pulses is ~7 fs, which corresponds to ~3 optical cycles.

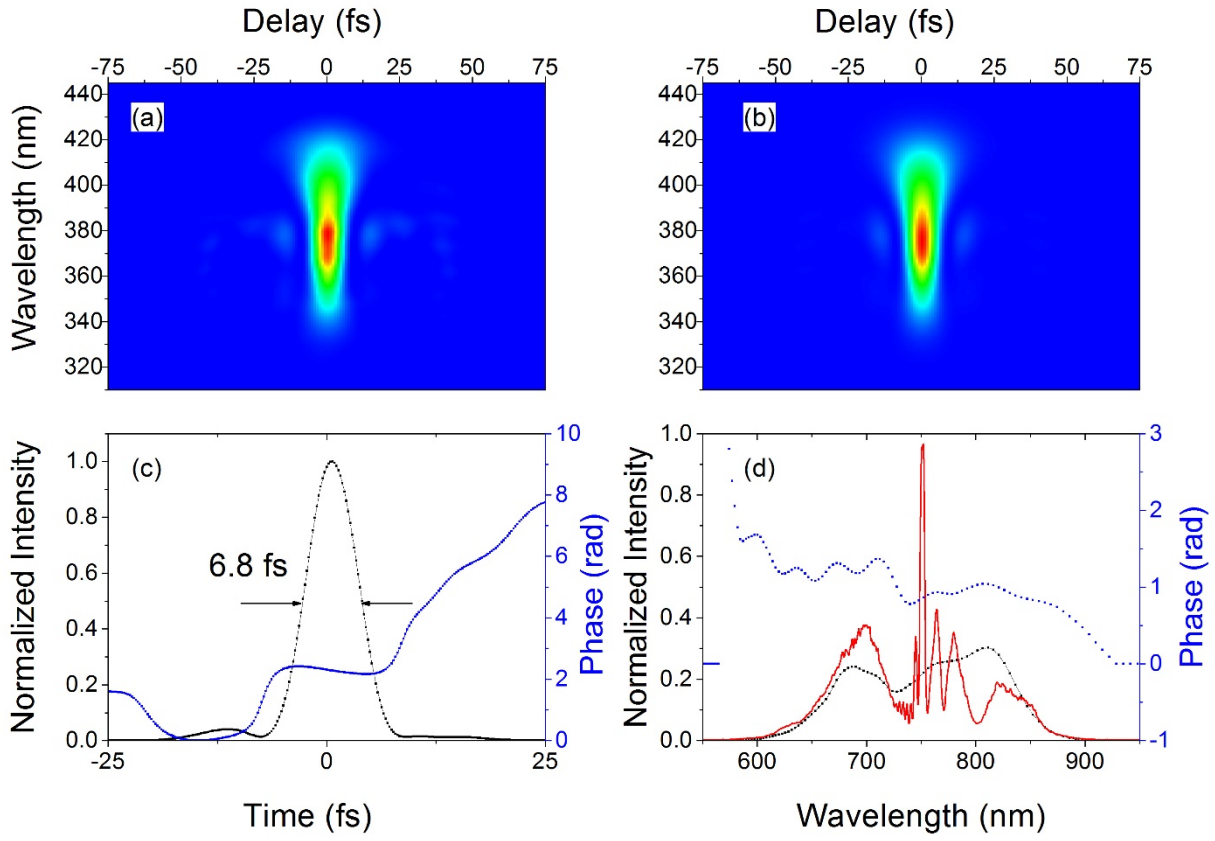

Figure 3.2 The FROG measurement of a few-cycle laser pulse after the hollow-core fiber. (a) The measured FROG trace. (b) The reconstructed FROG trace. (c) The retrieved pulse shape (black dotted curve) and phase (blue dotted curve). (d) The retrieved power spectrum (black dotted curve) and phase (blue dotted line) and independently measured spectrum (red dotted curve).

3.2 Polarization Gating

After the development of the three-step model in 1993, the strong dependence of the HHG efficiency on the ellipticity of the driving field was both theoretically treated and experimentally demonstrated [43], [48], [49]. If the driving field is elliptical, the tunnel-ionized electrons not only gain velocity in the z direction (which is the direction of the laser field with linear polarization), but they also are accelerated in the transverse direction. When the electrons

return, the displacement in the transverse direction significantly reduces the possibility of recombination. This effect has been experimentally observed.

The idea of PG was first proposed in 1994 by Corkum to take advantage of this ellipticity dependence [45], suggesting using two laser pulses with different frequencies. In 1999, Platonenko and Strelkov proposed a different method which superimposes a left- and right-circularly polarized pulse for PG with only one central frequency [50]. This scheme has been adopted by many researchers. In 2006, isolated 130 as pulses using PG method were experimentally demonstrated [30].

Experimentally, PG only needs two optical devices: a full-order quartz plate and a zero-order quarter wave plate. For a linearly-polarized laser field, the optical axis of the first full-order quartz plate is set to be 45° versus the polarization direction of the driving field in the plane perpendicular to the laser propagation direction. Then, due to the birefringence of the quartz plate, the electric fields parallel and perpendicular to the optical axis travel at different velocities. The delay between the two fields, T_d, is determined by the difference in the group velocities along the ordinary and extraordinary axes as well as the thickness of the quartz plate. After that, the zero-order quarter wave plate converts the two delayed pulses into right- and left-circularly polarized laser. Within the temporal region where the two pulses are still overlapped, the ellipticity is cancelled, and a linearly-polarized field is obtained. It is this region of overlap that defines a gate period with linear polarization. All other regions are elliptically polarized and therefore cannot generate the high order harmonics. If the gate is short enough—shorter than half of the optical period—then only one attosecond pulse can be generated. For example: using a Ti:Sapphire laser at a 750 nm center wavelength, the gate width should be narrower than 1.25 fs.

To fully understand this scheme, it is necessary to mathematically solve the final expression of the time-varying polarized laser field. The incoming laser field can be assumed to be a Gaussian pulse expressed as

$$E_0 e^{-2\ln(2)\left(\frac{t}{\tau_p}\right)^2}\cos(\omega_0 t+\varphi_{CE}) \quad (3.5)$$

where E_0 is the peak electric field and τ_p is the pulse duration. After the first quartz plate (which is a full waveplate), the two perpendicular pulses can be expressed as

$$E_o(t)=\frac{\sqrt{2}}{2}E_0 e^{-2\ln(2)\left(\frac{t-T_d/2}{\tau_p}\right)^2}\cos(\omega_0 t+\varphi_{CE}), \quad (3.6)$$

$$E_e(t)=\frac{\sqrt{2}}{2}E_0 e^{-2\ln(2)\left(\frac{t+T_d/2}{\tau_p}\right)^2}\cos(\omega_0 t+\varphi_{CE}) \quad (3.7)$$

where $E_o(t)$ and $E_e(t)$ are the ordinary and extraordinary field, T_d is the delay, ω_0 is carrier frequency, and φ_{CE} is the carrier-envelope phase. After the zero-order quarter waveplate, the final electric fields can be expressed as

$$E_{driving}(t)=\frac{\sqrt{2}}{2}E_0\left[e^{-2\ln(2)\left(\frac{t-T_d/2}{\tau_p}\right)^2}+e^{-2\ln(2)\left(\frac{t+T_d/2}{\tau_p}\right)^2}\right]\cos(\omega_0 t+\varphi_{CE}) \quad (3.8)$$

$$E_{gating}(t)=\frac{\sqrt{2}}{2}E_0\left[e^{-2\ln(2)\left(\frac{t-T_d/2}{\tau_p}\right)^2}-e^{-2\ln(2)\left(\frac{t+T_d/2}{\tau_p}\right)^2}\right]\sin(\omega_0 t+\varphi_{CE}) \quad (3.9)$$

where $E_{drive}(t)$ is along the original polarized direction and $E_{gate}(t)$ is perpendicular to the original polarized direction. Assuming a 3-cycle delay by the full-order quartz plate, the final driving and gating fields are plotted with the red line in Fig. 3.3 (a) and (b). A 3-D plot in Fig.

3.4 below clearly shows that only the center portion of the final laser field is linear, while all other portions are highly elliptical.

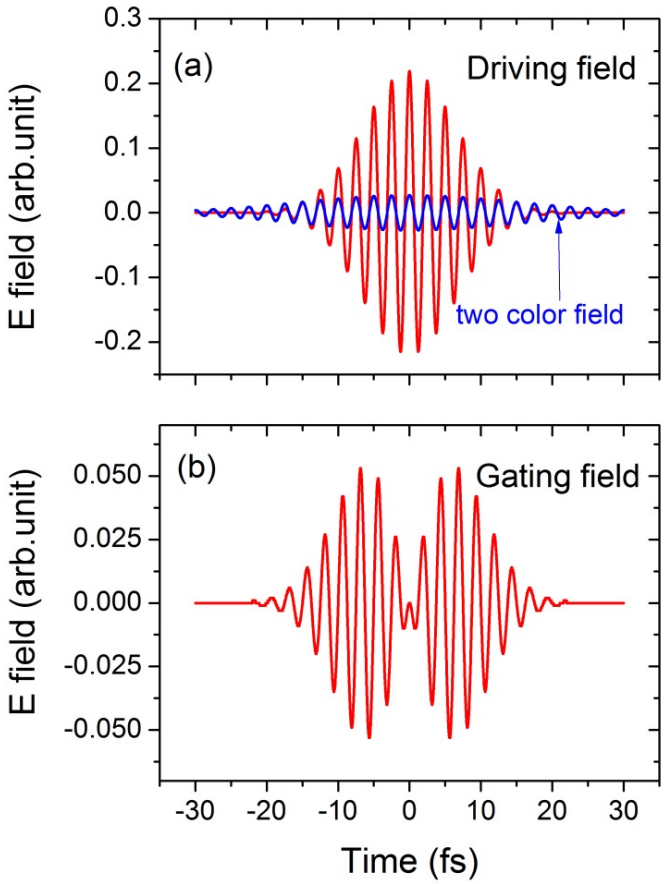

Figure 3.3 Schematic drawings of the (a) driving and (b) gating field for PG and DOG techniques. The blue line in the (a) driving field is the second harmonic of the gating field using only for DOG.

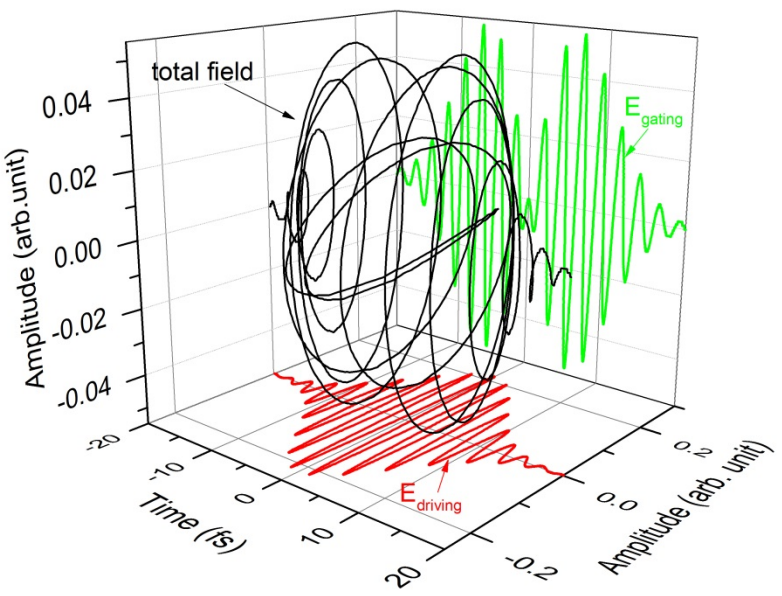

Figure 3.4 The final electric field for PG in a three dimensional frame. The black line is total field. The red (driving field) and green lines (gating field) are its projection on two orthogonal planes. The delay introduced by the first quartz plate is three cycles.

The ellipticity of the final electric field is a time-dependent function and can be calculated as

$$\xi(t) = \frac{E_{gating}}{E_{driving}} = \frac{1-e^{-4\ln(2)\frac{T_d}{\tau_p^2}t}}{1+e^{-4\ln(2)\frac{T_d}{\tau_p^2}t}} \approx \left|2\ln(2)\frac{T_d}{\tau_p^2}t\right| \qquad (3.10)$$

The ellipticity from the above equation should be less than a threshold value determined by the experiment, meaning the efficiency of the HHG should decrease by at least one order of magnitude with this ellipticity. Then the gate width within which the HHG can be generated is

$$\delta t_G \approx \frac{\xi_{th}}{\ln(2)}\frac{\tau_p^2}{T_d} \qquad (3.11)$$

where ξ_{th} is the threshold ellipticity for harmonic generation. To generate a single isolated attosecond pulse, the gate width should be less than the half cycle period of the driving field. In

our case, a Ti:Sapphire laser system is used and this value should be 1.2 fs. As ξ_{th} is ~0.2 for this wavelength, the equation becomes

$$\delta t_G \approx \frac{0.2}{\ln(2)} \frac{\tau_p^2}{T_d} < 1.2\ fs \qquad (3.12)$$

The benefit of PG versus AG is that we can always adjust T_d to meet the requirement in equation 3.8. The required delay T_d as a function of the input laser pulse duration is shown in Fig. 3.5 (a). It can be seen that we can maintain a gate width less than half the laser cycle, even with a very long pulse, if the delay is properly chosen. On the other hand, the delay will also decrease the peak intensity where the high-order harmonics are generated. As shown in Fig. 3.5 (b), the larger the delay is, the smaller the peak intensity becomes. Obviously, higher peak intensity is preferred for a broader XUV bandwidth, smaller intrinsic chirp, and thus shorter pulse duration. Therefore, there is a tradeoff between the two factors, and the delay should be chosen to be as small as possible while still satisfying equation 3.8.

In addition to the gate width, another necessary condition for HHG is that the target atom responsible for attosecond light emission must not be fully ionized when the electric field inside the gate arrives. With the ADK model [51], the ionization probability of neon atoms can be calculated as a function of the peak intensity inside the gate. One such result for input pulse duration of 7 fs is shown with the black line in Fig. 3.6. According to the plot, the highest peak intensity achievable with neon gas for a 7 fs driving pulse is $7 \times 10^{14} W/cm^2$, corresponding to a cutoff photon energy of 150 eV. Using argon, which has a smaller ionization potential, this value is significantly reduced to 60 eV, meaning the shortest pulse duration achievable is only ~200 as. To generate shorter attosecond pulses, shorter driving pulses are needed. For example, in Ref [30], 5 fs driving pulses were used, and isolated 130 as pulses were demonstrated.

However, using atoms with higher ionization potential such as helium decreases the HHG efficiency by at least two orders of magnitude, leading to the practical difficulties in collecting experimental data. This is why neon gas was the most suitable target atom for this work.

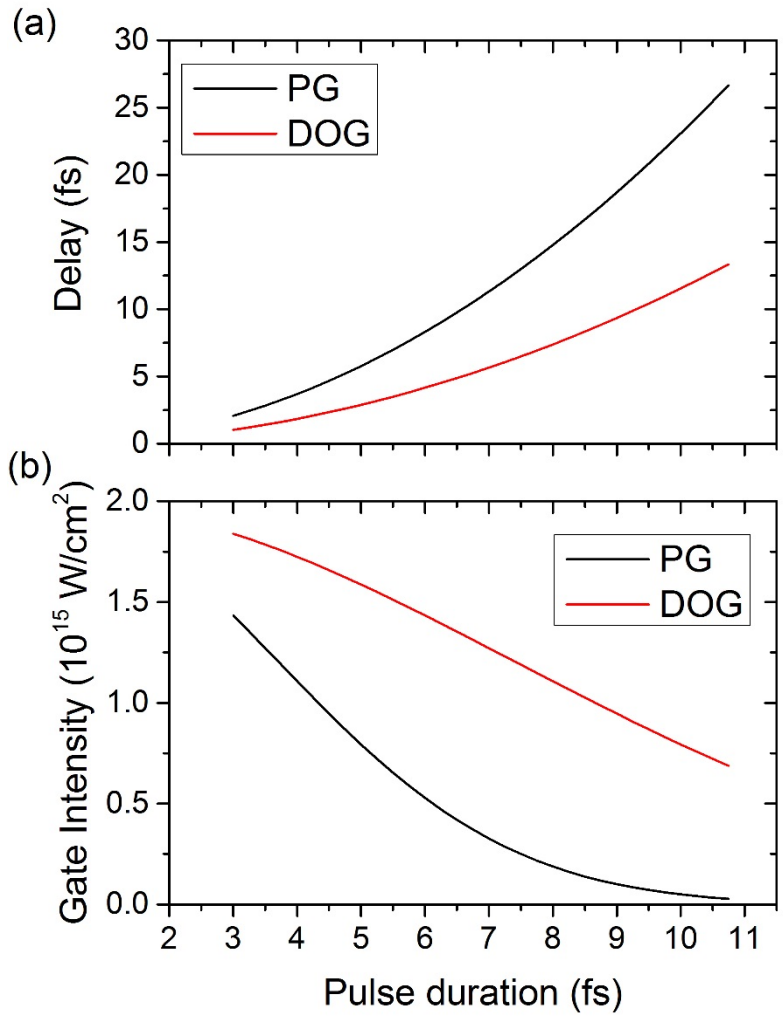

Figure 3.5 (a) Delay of the first quartz plate required for generating single attosecond pulses as a function of the driving pulse duration. Black: PG. Red: DOG. (b) The peak intensity inside of the gate, assuming the peak intensity of the linearly polarized input pulse is $2 \times 10^{15} W/cm^2$. Black: PG. Red: DOG.

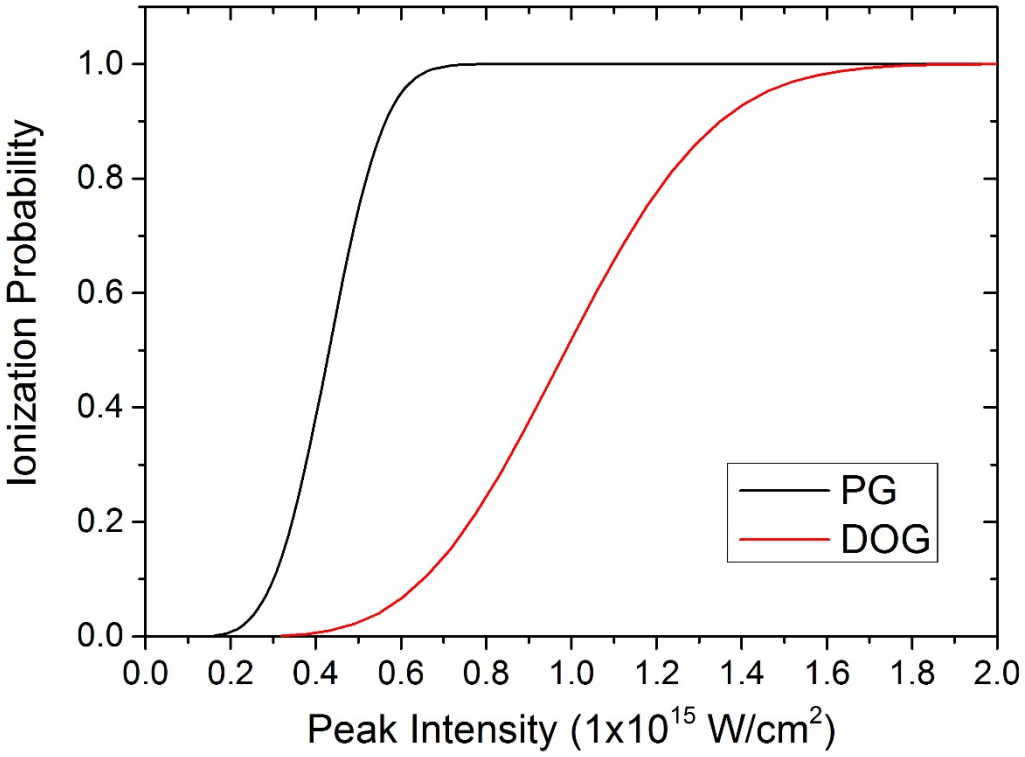

Figure 3.6 The ionization probabilities of a neon atom, calculated with the ADK model, as a function of the peak intensity inside the gate. The pulse duration is assumed to be 7 fs, and the gate width is calculated for PG and DOG to select a single attosecond pulse. Black line: PG. Red line: DOG

It should be noted that the experimentally-measured spectral bandwidth is usually much narrower than the calculation due to phase mismatching. Up to now it has not been demonstrated that PG can generate single attosecond pulses with durations of less than 100 as.

3.3 Double Optical Gating

As discussed in the PG section, the gate width should be less than the half-cycle period of the driving laser since the three steps for generating high-order harmonics repeat every half

cycle. If this periodicity increases to one full cycle, the requirement of the gate width is loosened by a factor of two. This is the idea of the Double Optical Gating [31]–[33].

It is well known that by adding a second harmonic to the driving field, the field symmetry is broken, and only one XUV pulse can be produced within one optical cycle of the driving field. This is termed as “two-color gating”. The DOG method takes advantage of two-color gating and combines it with the PG scheme. Since the driving field is the field actually responsible for harmonic generation, the two-color field should also be superimposed in the same direction. Therefore, the gating field is used to generate its second harmonic through a β-BaB_2O_4 (BBO) crystal optimized for type-I phase matching. A schematic drawing of the two color field is plotted with the blue line in Fig. 3.3 (a).

Experimentally it is simple to achieve DOG conditions. Instead of using a zero-order quarter waveplate, another full-order quartz plate and a BBO combine and function as the quarter waveplate. The typical experimental photoelectron spectra with linear and DOG driving fields are plotted in Fig. 3.7. The details of the setup can be found in Chapter 5. The sharp edge at 52 eV is from the 300 nm thick aluminum filter which is used to block the remaining driving pulse while transmitting the XUV light.

Compared to PG, the most obvious advantage of the DOG technique is that longer driving pulses are allowed for single attosecond pulse generation, as shown in Fig. 3.5 (a). This is very critical since PG practically requires 5 fs driving pulse, which, while not impossible, is still quite a challenge. This is because a longer driving pulse requires a larger delay, which reduces the peak intensity. In contrast, DOG allows for 7-10 fs driving pulses while still generating a strong signal and high HHG cutoff. Such pulse durations can be routinely produced from the hollow core fiber and compressor system.

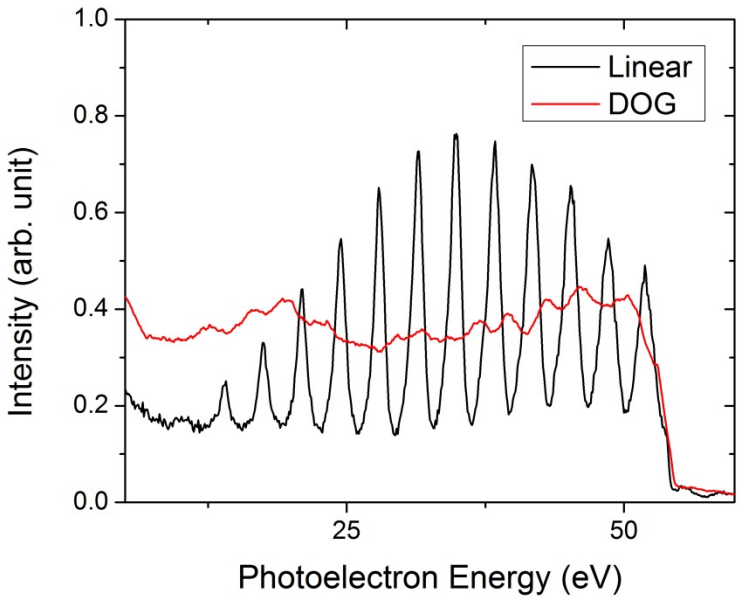

Figure 3.7 The photoelectron spectra of HHG generated with linear polarized driving laser (black line) and DOG driving laser (red line). The 300 nm thick Aluminum filter is used to block the remaining driving pulse and transmitting the XUV.

Furthermore, DOG can be appreciated from another point of view: for equal pulse durations, DOG allows the use of less delay time T_d compared to PG, hence increasing the peak intensity inside the gate with the same pulse energy (as shown in Fig. 3.5 (b) with the red curve). More importantly, the shorter delay time required by DOG significantly reduces the ionization before the gate under the same peak intensity (as calculated by the ADK model and shown in the red curve in the Fig. 3.6). In other words, this calculation shows that higher peak intensity inside the gate can be used for DOG than PG, which is crucial for generating a broadband supercontinuum from HHG.

Since DOG is much better than PG, it is applied throughout the work shown in this dissertation. Experimental results are presented in Chapter 5 and 6.

CHAPTER 4 TEMPORAL CHARACTERIZATION OF ATTOSECOND PULSES

To characterize femtosecond pulses, FROG is often used, as discussed in Chapter 3.1. However, using FROG to measure attosecond pulses is difficult due to low photon fluxes. Since the spectra of the attosecond pulses can be easily measured, only the spectral phase information is needed for complete characterization. Currently, the technique used for measuring the spectral phase is termed as “attosecond streaking”, which is similar to the concept of FROG for measuring the spectral phase of the femtosecond laser. It should be noted that with attosecond pulses today, the electric fields of the femtosecond lasers can be directly mapped out without any ambiguity in the attosecond streaking experiments [52]. In this section, a simple technique to characterize the attosecond pulse train termed as Reconstruction of attosecond beating by interference of two-photon transition (RABITT) was first introduced. Then the principle of the attosecond streaking technique for measuring the spectral phase for isolated attosecond pulses was discussed, and two algorithms to retrieve the phase are discussed and compared.

4.1 RABITT

Reconstruction of attosecond beating by interference of two-photon transition (RABITT) was developed for characterizing the average duration of the attosecond pulses in a train generated from the HHG. In the spectrum domain, the attosecond pulse train corresponds to discrete harmonic peaks separated by two photon energies of the driving laser. The power

spectrum can be easily measured with an electron TOF spectrometer as shown in Fig. 2.6. A typical experimental configuration can be found in Fig 2.5.

To characterize the attosecond pulse duration, only the phase information is needed. In RABITT, in addition to the XUV attosecond train, an extra weak IR laser is introduced in the detection. Due to the laser symmetry, only the odd order harmonic can be observed for the HHG. In the detection, a ground state electron inside the atom of a target gas (i.e. Neon atom) is photoionized by the XUV pulse. With the presence of the extra IR laser, it is possible to photoionize ground state electron to a continuum state between two harmonic. This is called the "sideband", which is the transition caused by one XUV and one IR photon, as shown in Fig. 4.1 below. The electron in the ground state can absorb an XUV photon $E_{q-1}e^{i(q-1)\omega t+\emptyset_{q-1}}$ and an IR photon $E_1 e^{i\omega t}$ or absorb an XUV photon $E_{q-1}e^{i(q+1)\omega t+\emptyset_{q+1}}$ and emit an IR photon $E_1 e^{i\omega t}$. So the final sideband can be expressed as (assuming the intensity of each harmonic peak is the same)

$$b_{sideband}(\omega,\tau) \propto \int_{-\infty}^{\infty}(E_{q-1}E_1 e^{iq\omega t+\emptyset_{q-1}} + E_{q+1}E_1 e^{iq\omega t+\emptyset_{q+1}})\, e^{-i\omega t}dt \qquad (4.1)$$

The $\tau$is the delay between the XUV and the IR. As the delay is scanned, the intensity of the sideband in the spectrum domain can be expressed as

$$I_{sideband}(\omega,\tau) \propto \left|\int_{-\infty}^{\infty}\left(E_{q-1}E_1 e^{iq\omega t+\emptyset_{q-1}} + E_{q+1}E_1 e^{iq\omega t+\emptyset_{q+1}}\right) e^{-i\omega t}dt\right|^2 \propto [1 + \cos(2\omega\tau + \emptyset_{q+1} - \emptyset_{q-1})] \qquad (4.2)$$

It can be seen that the intensity of the sideband is oscillating depending on the spectral phase difference $\emptyset_{q+1} - \emptyset_{q-1}$. Therefore the relative temporal position of each sideband determine the spectral phase difference between each adjacent harmonics from the HHG.

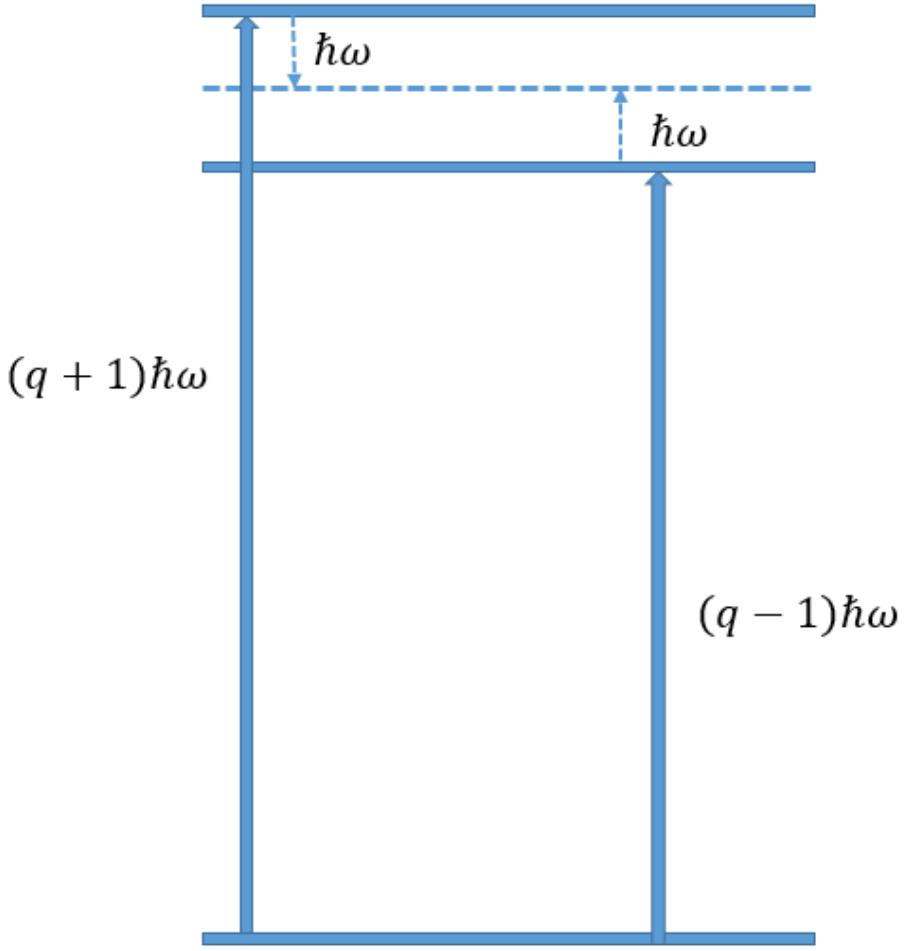

Figure 4.1 A schematic drawing of the RABITT photon transition. The sideband (dashed line) can be produced by one XUV photon adding one IR photon.

4.2 The Principle of Attosecond Streaking

To characterize the isolated attosecond pulse, RABITT cannot be used since the spectra now are continuous. To solve this issue, the attosecond streaking can be used.Traditionally speaking, a streak camera is a device used to streak the fast electron pulses by applying a fast-varying high voltage perpendicular to the electron propagation direction [53]. The streaked electrons are spatially displaced depending on their experience in the fast-varying voltage. This way, the temporal information of the electrons can be obtained from their spatial distribution. The resolution of a streak camera is determined by the streaking speed (if the instrumental resolution is infinitely small). In other words, the gradient of this fast-varying sweeping voltage will determine the resolution. For measuring attosecond pulse, there is no such device that can supply a sweeping voltage on the attosecond scale. However, the fast-varying electric field of a laser which is phase-locked with the attosecond pulse can be used as the “sweeping voltage”. This is the basic idea of the attosecond streaking [54], [55]. Practically, this phase-locked streaking pulse usually comes from a small portion of the driving laser itself. To completely understand this process, quantum mechanics should be applied [56], [57].

As shown in Fig. 4.2 (a), the photoelectrons generated by the XUV pulse are dressed by the streaking field, and their momentum is altered. By scanning the delay between the XUV and the streaking field in Fig. 4.2 (a), a two-dimensional spectrogram can be obtained, as plotted in Fig. 4.2 (b). This so-called “streaking trace” contains the complete information for characterization.

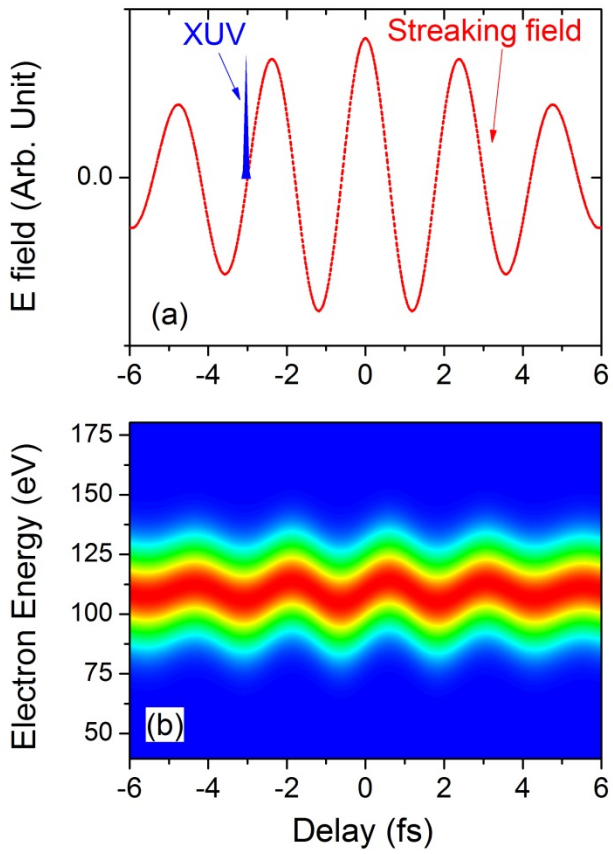

Figure 4.2 A schematic drawing depicting the principle of attosecond streaking (a) XUV (blue) and streaking field (red dashed) (b) The streaking trace obtained by scanning the delay between XUV and streaking field and recording photoelectron spectra at each delay.

4.3 Complete Reconstruction of Attosecond Bursts

In a streaking experiment, the attosecond XUV pulse is focused onto a gaseous target to photoionize the neutral atoms. The photoelectrons generated are then streaked by a phase-locked few-cycle intense IR laser field, giving a momentum shift to the electrons. Assuming a linear streaking field is applied, the momentum change can be expressed as [54], [58]

$$\Delta p(t) = \int_t^\infty e\varepsilon(t')dt' = eA_L(t) \qquad (4.3)$$

where $A_L(t)$ is the vector potential of the laser field. This momentum shift can be recorded as a function of delay between the XUV pulse and the streaking field by a Time-Of-Flight (TOF) electron spectrometer. In atomic units, the final streaking trace can be expressed as a function of energy and delay as

$$S(W,\tau_D) \approx \left|\int_{-\infty}^{\infty} dt E_X(t-\tau)\, d[p + A_L(t)] e^{i\varphi(p,t)} e^{-i(W+I_p)t}\right|^2 \qquad (4.4)$$

$$\varphi(p,t) = -\int_t^\infty dt' \left[pA_L(t')\cos\theta + {A_L}^2(t')/2\right] \qquad (4.5)$$

where E_X is the complex field amplitude of the XUV pulse, τ is the delay between the XUV and streaking pulses, W is the kinetic energy of the photoelectron, and I_p is the ionization potential of the target gas. For a narrow bandwidth XUV spectrum, we can replace the momentum in equation 4.3 with the central momentum p_0 and the dipole transition element $d(p)$ with a constant d_0. This condition is called the Central Momentum Approximation (CMA). Under the CMA, we rewrite equation 4.3 to be

$$S(W,\tau_D) \propto \left|\int_{-\infty}^{\infty} dt E_X(t-\tau)\, G\,(t) e^{-i(W+I_p)t}\right|^2 \qquad (4.6)$$

Assuming only electrons parallel to the streaking field are detected, the gating function $G(t)$ can be expressed as:

$$G(t) = \exp\{-i \int_t^{\infty} dt' \left[p_0 A_L(t') + {A_L}^2(t')/2\right]\}. \qquad (4.7)$$

Note that $G(t)$ is a function of time but independent of the momentum. It can be seen that Equation 4.4 has the same form as the Equation 3.4, which is used in Frequency-Resolved Optical Gating (FROG) to characterize the femtosecond laser pulse. The phase modulation function $G(t)$ works as a temporal gate (using FROG terminology). The streaking trace can then be treated as a FROG trace and both $E_X(t-\tau)$ and $G\ (t)$ can be retrieved using the well-known Principal Component Generalized Projections Algorithm (PCGPA) [47], [59], [60]. This technique is termed as the Complete Reconstruction of Attosecond Bursts (CRAB) [58].

PCGPA is very robust against noise [59]. However, the CMA must be obeyed for CRAB to perform correctly. When an ultrabroadband continuum is generated and its spectral phase needs to be retrieved, the CRAB method does not work properly. In this case, a new technique for phase retrieval without the CMA is necessary.

4.4 Phase Retrieval by Omega Oscillation Filtering

As explained in the above section, a streaking trace collects the oscillations of the photoelectron spectra as the delay between the XUV and streaking IR pulses is altered. However, in the limit of low streaking intensity, similar to the RABITT, this oscillation can also be interpreted as the interference of different quantum paths to the same final electron state [61]. Mathematically speaking, the gate function can be rewritten as follows:

$$G(t) = e^{i\phi(t)} \approx 1 + i\phi(t) \qquad (4.8)$$

In the lower limit the of the streaking field, $\phi(t)$ can be estimated by

$$\phi(t) \approx \frac{\sqrt{8WU_p(t)}}{\omega_L}\cos\theta\cos(\omega_L t) = \frac{\sqrt{8WU_p(t)}}{2\omega_L}\cos\theta\,(e^{i\omega_L t} + e^{-i\omega_L t}) \qquad (4.9)$$

where U_p is the ponderomotive energy and ω_L is the angular frequency of the streaking field. Plugging this into equation 4.4 yields [61]

$$S(W,\tau_D) = \left|\int_{-\infty}^{\infty} dt E_X(t-\tau)\,G\,(t)e^{-i(W+I_p)t}\right|^2 \approx S_0 + S_{\omega_L} + S_{2\omega_L}. \qquad (4.10)$$

where S_0, S_{ω_L}, $S_{2\omega_L}$ are streaking trace components which oscillate with DC, one dressing laser frequency, and two dressing laser frequencies. Higher-order components are ignored here. The trace S_{ω_L} contains the complete information of the XUV pulse. To retrieve the spectral phase difference, it is only needed to guess the spectral phase that matchesS_{ω_L}. Retrieving the spectral phase from these oscillations then reduces to a minimization problem.

Unlike FROG-CRAB, the PROOF method does not use FROG phase retrieval algorithms, and the central momentum approximation is not needed. Furthermore, observation of this oscillation does not require high streaking intensities, as only one NIR photon is needed to couple the continuum states. This has a significant advantage since the strong streaking field can also photoionize the target gas. Similar to HHG, the electric field first tunnel ionizes the ground state electron, then this electron is accelerated in the remaining laser field. Under certain circumstances (see equation 2.4 and related discussion), this accelerated electrons can come back to the parent ion. However, instead of recombining with the ion like in HHG, it is scattered

away. This process of generating free electrons is termed as Above Threshold Ionization (ATI). Obviously, the lower intensities can reduce the electron noise from the ATI significantly.

To understand the PROOF from a physical standpoint: for low streaking intensities, one can interpret the streaking as the interference of electrons ionized through different pathways. As explained in Ref [61], the electron signal at a given energy may come from direct ionization from one XUV photon, one XUV plus one IR photon, and one XUV minus one IR photon. Therefore, when the component of oscillation with the dressing laser center frequency ω_L is extracted, the phase angle of the sinusoidal oscillation $\alpha(v)$ is related to the spectral phases $\varphi(\omega_v - \omega_L)$, $\varphi(\omega_v)$, and $\varphi(\omega_v + \omega_L)$ of the three XUV frequency components separated by one laser photon energy and the intensities $I(\omega_v - \omega_L)$, $I(\omega_v + \omega_L)$:

$$\tan[\alpha(v)] = \frac{\sqrt{I(\omega_v+\omega_L)}\sin[\varphi(\omega_v)-\varphi(\omega_v+\omega_L)]-\sqrt{I(\omega_v-\omega_L)}\sin[\varphi(\omega_v-\omega_L)-\varphi(\omega_v)]}{\sqrt{I(\omega_v+\omega_L)}\cos[\varphi(\omega_v)-\varphi(\omega_v+\omega_L)]-\sqrt{I(\omega_v-\omega_L)}\cos[\varphi(\omega_v-\omega_L)-\varphi(\omega_v)]} \qquad (4.11)$$

The equation can be understood as the interference between the single-photon (XUV only) and two-photon (XUV plus NIR) transitions from the atomic ground state to the continuum state $\omega_v - I_p$.

Initially, the PROOF algorithm was written to minimize only the difference between the experimental phase angle and the guessed one. However, the robustness against many practical parameters was untested. In contrast, the PCGPA algorithm applied in the CRAB method has been demonstrated to be very robust against noise and other imperfections. Therefore, it would be ideal to use the PCGPA algorithm in the PROOF. Since the spectral and phase information are completely encoded in $S_{\omega_L}(v,\tau)$, we intentionally construct a new streaking trace termed as PROOF trace, $S_{PROOF}(v,\tau_D) = S_0 + \frac{v_0}{v}S_{\omega_L} + \frac{v_0^2}{v^2}S_{2\omega_L}$, in which the phase gate function is

independent of the momentum. Therefore, PCGPA can directly work on the PROOF trace without the central momentum approximation. This way, we take advantage of the robustness of the PCGPA while still avoiding the CMA. This method has been applied in retrieving the single 67 as pulse.

4.5 Reconstruction Error

Since the FROG was first introduced during the early 1990's for femtosecond laser characterization, there is a fundamental question needs to ask: how accurate is the phase retrieval of the PCGPA program? To answer this question, the FROG error, a criterion for describing if FROG algorithm converges successfully, was proposed [46]. The FROG error can be expressed as [62]:

$$\epsilon_{FROG} = \left\{\frac{1}{N^2}\sum_{i=1}^{N}\sum_{j=1}^{N}\left[I(\omega_i,\tau_j) - I'(\omega_i,\tau_j)\right]^2\right\}^{1/2} \qquad (4.12)$$

where N is the pixel number of the spectrogram, $I(\omega_i,\tau_j)$ and $I'(\omega_i,\tau_j)$ are the (i, j) component in the experimental and retrieved trace. Extensive tests have been done to determine the value of the ϵ_{FROG} when the retrieval is considered converged. Since there is only one converging solution for the FROG, the convergence leads to the correct phase retrieval.

When the FROG idea was further applied in attosecond regime at 2005, considering the similarity between a streaking trace and a FROG trace with a pure phase gate, it seems natural to follow the FROG error criterion in the attosecond region. However we noticed that the FROG error is often used in the case with a real gate function such as Polarization Gating and Second Harmonic Gating. For an attosecond streaking measurement, it actually has a gating function

with only a phase term $e^{i\phi(t)}$. From the analysis in the section above, the zero-order component of the streaking trace I_0, while the largest component in the spectrogram, does not contain any XUV phase information of the XUV pulse since it does not oscillating with time delay τ. This suggests the largest contribution of the FROG error, which is inherited from the DC component of the streaking trace, does not reflect the accuracy of the reconstruction either. The main term containing the XUV phase information is the one oscillating with one IR laser frequency, so it is apparent that we should use a similar expression but replace the whole streaking trace with only the one ω_L term. The PROOF error can be therefore expressed as:

$$\epsilon_{FROG} = \left\{\frac{1}{N^2}\sum_{i=1}^{N}\sum_{j=1}^{N}\left[I_{\omega_L}(\omega_i,\tau_j) - I'_{\omega_L}(\omega_i,\tau_j)\right]^2\right\}^{1/2} \qquad (4.13)$$

where $I_{\omega_L}(\omega_i,\tau_j)$ is the (i, j) component in the one ω_L trace extracted from the new built spectrogram $I_{PROOF}(v,\tau_D)$ and $I'_{\omega_L}(\omega_i,\tau_j)$ is the reconstructed one.

CHAPTER 5 EXPERIMENTAL CONFIGURATION

A broadband supercontinuum supporting single attosecond pulse can be generated with DOG and characterized by CRAB and PROOF. To experimentally demonstrate it, an attosecond streak camera was built based on Magnetic Bottle Energy Spectrometer (MBES). MBES is chosen to record the photoelectron generated by the attosecond XUV pulse because of its high resolution and collection efficiency. In this chapter, we first introduce the experimental configuration. Then in the second section, we focus on the MBES and explain its principle and present some simulated results. The resolution of the whole system is discussed at the end.

5.1 Experimental Configuration

A schematic drawing of the experimental configuration for the attosecond streaking experiment is shown in Fig. 5.1. Laser pulses with 25 fs duration and 1 kHz repetition rate are produced by a Ti:Sapphire multi-pass CPA system centered at 780 nm. The laser from the amplifier is then focused onto a hollow-core fiber filled with neon gas. The spectral bandwidth is expanded by self-phase modulation, and six pairs of chirped-mirrors compress the fiber output pulse to around 7 fs in duration. This compressed beam is then split into two arms by a broadband beam splitter. The transmitted beam (containing 90% of the total energy) propagates through the DOG optics and is focused to a neon gas target for generation of the isolated attosecond pulses. The reflected arm (containing the other 10% of the pulse energy) is phase-locked to the generation beam using a stabilized interferometer (as shown by the green beam following the same path) and recombines with the XUV pulses by a hole-drilled mirror.

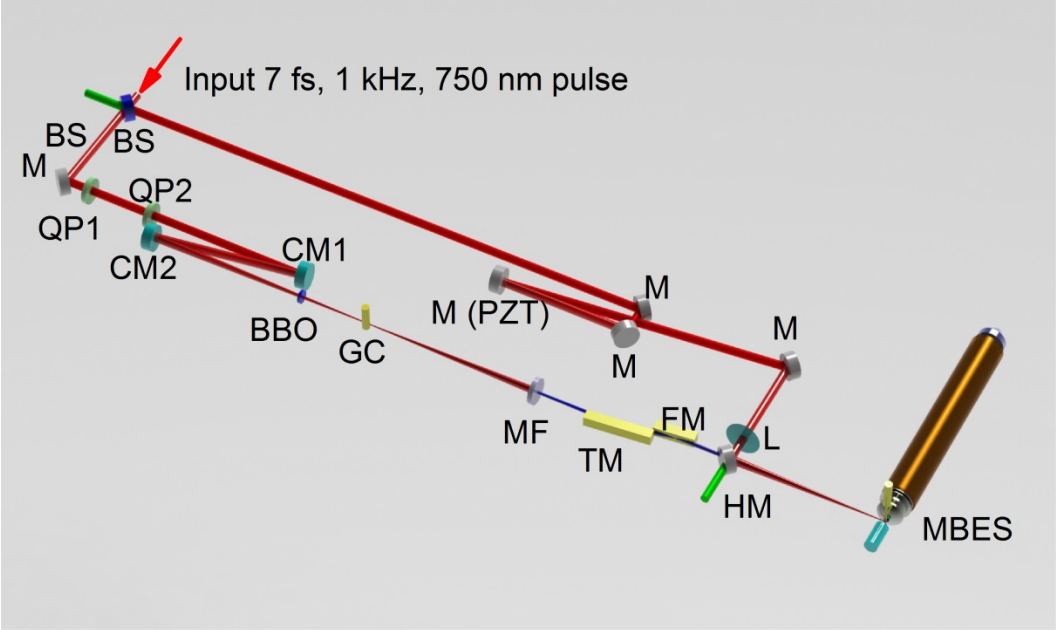

Figure 5.1 A schematic drawing of the experimental configuration for the attosecond streaking experiment based on a Magnetic Bottle Energy Spectrometer (MBES). BS: Beam Splitter; QP: Quartz Plate; M: Silver Mirror; CM1: convex mirror with -150 mm focal length, CM2: concave mirror with 250 mm focal length; GC: Gas Cell; MF: Metallic Filter; TM: Toroidal Mirror; FM: Flat Mirror; L: Focus Lens; HM: Hole drilled Mirror; MBES: Magnetic Bottle Electron Energy Spectrometer.

The laser field in the generation arm goes through the DOG optics (QP1 and QP2) and is focused by a convex (f = -150 mm) and a concave mirror (f = 250 mm). The effective focal length equals to 175 mm. Then the focusing beam passes through a BBO crystal with a thickness of 141 μm, which forms a zero-order quarter wave plate with the second quartz plate. A 0.5~1 mm-thick glass cell is positioned roughly 1 mm after the laser focal spot to ensure good phase matching of the HHG. After that, a thin film metal filter (usually aluminum or zirconium) is used to block the remaining driving pulse while transmitting the XUV light, which is then focused by a gold-coated toroidal mirror onto the second gas target for photoionization. In the reflected arm, the streaking beam passes through the exact optical path length and is focused by a 300 mm focal lens onto the same spatial spot as the XUV beam. The photoelectron generated by the XUV

pulse will be momentum-shifted by the streaking field and then collected by a Magnetic-Bottle Energy Spectrometer (MBES).

The chosen focal length and the distance between the BBO and the gas cell are related to each other and crucial to the success of the DOG. The laser should be tightly focused on to the gas target for high HHG cutoff. However, using mirrors unavoidably introduces astigmatism to the focal spot. Tighter focus means larger astigmatism. Additionally, the highest peak intensity that DOG can take for neon gas before fully depleting the ground state electrons is about $2 \times 10^{15}\ W/cm^2$, as shown in Fig. 3.7. Considering the pulse energy of the driving beam is about 0.8 mJ, the beam size needed to reach this intensity is roughly around 20 μm. Therefore, the focal length is chosen to be around 150 mm to 200 mm. This sets a limitation for the distance between the BBO and the gas cell. Also the beam size of the driving laser on BBO needs to be small so that the intensity is high enough to produce sufficient second harmonic for the two-color gating. On the other hand, the intensity cannot be too high without damaging the BBO. The distance between the BBO and the gas cell is experimentally determined to satisfy the two requirements above. The beam size is usually about 4 mm on the BBO.

Since the second harmonic and the fundamental beam have different refractive indices in air, it is necessary to keep the BBO under the vacuum so the second harmonic and the fundamental driving pulses are temporally overlapped on the gas target. If the focusing optics are outside the vacuum chamber, two curved mirrors such as the systems shown in our experimental configuration Fig. 5.1 need to be used to reduce the astigmatism. If the focusing optics can be put inside the vacuum, such as in Ref [34], one single concave mirror can be used. However, this type of system is complicated to construct and difficult to align. Alternatively, a focusing lens

could be used with easy operation. The lens configuration was first considered to destroy the few-cycle pulses at the focus, but exact calculation showed that laser pulses as short as 5 fs can still be obtained under certain conditions using the lens focusing. This is discussed in Chapter 7.

In the streaking experiment, the delay between the XUV and the streaking arm needs to be stabilized during each delay step. To achieve this, an independent continuous laser centered at 532 nm follows the same path as the IR laser after the beam splitter and recombines after the hole mirror, where an interference pattern is generated. The 532 nm wavelength is used to separate itself with the driving laser, which usually cover the spectra from 600 nm to 900 nm. The fringe of the interference is used to stabilize the time jitter between the XUV and streaking arms, and about 20 as RMS stability can be obtained [63]. Simulations have been done to ensure this level of time jitter can be tolerated for accurate reconstruction of the streaking trace [64], [65]. The delay between the XUV and streaking beams as well as the stabilization are both controlled by a piezo-transducer (PZT) attached to one of the flat silver mirrors in the streaking arm, as shown in Fig. 5.1.

The Magnetic-Bottle (MB) TOF spectrometer has many advantages over the traditional TOF spectrometers [66]. Firstly, the MBES can collect larger than 2π solid angle, leading to a collection efficiency of over 50%. This is considerably higher than field-free spectrometers. Since the conversion efficiency of the HHG is rather low and the energy of the generated XUV pulse is on the order of only one nanojoule, the count rates of electrons are low. Therefore, it is important to collect as many electrons as possible (although in attosecond streaking, electrons with emission angle larger than 90° have opposite streaking direction and are therefore highly undesirable). Secondly, a reasonably high resolution can be obtained if the MBES is properly designed and a long flight tube is adapted [66]–[71]. Note that in MBES, the flight tube length

does not affect the collecting efficiency, which is opposite from its field-free counterpart. As a result, it is possible to obtain high collection efficiency and good resolution simultaneously.

5.2 Principle of Magnetic Bottle Energy Spectrometer

The basic operating principle of MBES is illustrated in Ref [41] and will not be explained in detail here. In our system, a strong permanent magnet (neodymium-iron-boron, NdFeB) and a conical-shaped pole piece together produce a strong diverging magnetic field. The pole piece (made of soft iron) is used to focus the magnetic field from the permanent magnet into the tip surface of the cone since higher resolution can be expected for a stronger initial B field at the electron birthplace [66], [72], [73]. The strong B field is cylindrically symmetric around the axis of the cone and decreases quickly after the tip surface. The photoelectrons are generated about 1 mm away from the tip and collimated by the diverging B field. After the collimation, a weak but constant magnetic field generated by a solenoid is used to guide the electrons through a three-meter-long flight tube until reaching the Microchannel Plate (MCP). The earth's field is shielded by μ-metal wrapped around the flight tube. Each hit by an electron is amplified by the MCP and detected by the Data-Acquisition (DAQ) electronics. A schematic drawing of the MBES is shown in Fig. 5.2 (a) below. The ratio of the magnetic field at the electron birth place to the solenoid B field determines how good the parallelization is, and the collection efficiency (which should always be larger than 50%) is precisely determined by the B field and the distance between the photoelectron birthplace and the cone. As shown in Fig. 5.2 (b), our collection angle is 107°.

Since the magnetic field from the permanent magnet is the most critical parameter in the MBES, it is carefully calculated using SATE software [74]. The solenoid magnetic field can be calculated analytically. As shown in Fig. 5.3, the field along the flight axis, B_z, is plotted as a function of the flying distance. The blue line shows the magnetic field from the permanent magnet, and the red line is from the solenoid. The black solid line is the total B field. It can be seen that the total B field drops quickly until around 100 mm and then stays constant for the rest of the flight. The red dotted-line in the inset of the Fig 5.3 shows the comparison between calculation and measurement. It can be seen these two agree very well. The measurement of the magnetic field was only measured for the first 25 mm where the magnetic field changes quickly.

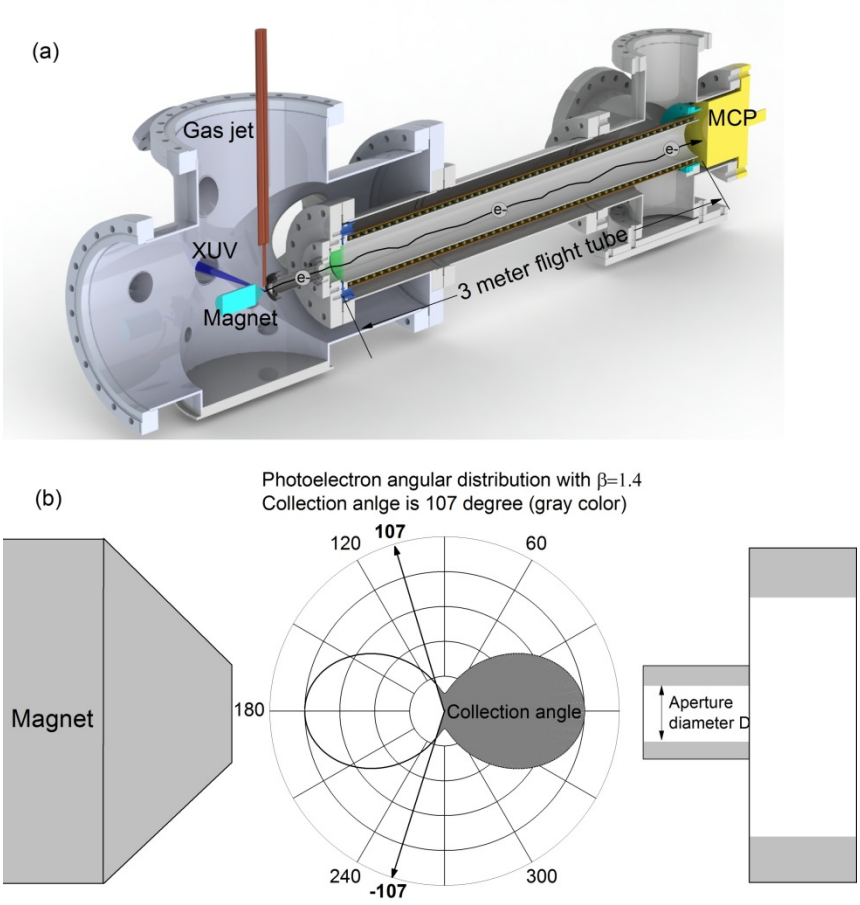

Figure 5.2 (a) Diagram of Magnetic Bottle Electron Spectrometer (MBES) with a three-meter-long flight tube. The XUV beam is focused 1 mm away from the magnet which produces a highly diverging magnetic field, and a 50 micrometer diameter stainless steel gas jet is placed on top of the XUV beam. Photoelectrons enter an aperture with a diameter D and fly through the three-meter-long tube before reaching the MCP detector. A solenoid coil with 0.8 A current is wrapped around the flight tube to supply a 10 Gauss magnetic field. A μ-metal tube is placed outside the flight tube to shield the earth's magnetic field. (b) An enlarged schematic diagram of the magnet and aperture. The plot in polar coordinates shows the photoelectron angular distribution with an asymmetric parameter of 1.4, as defined in equation 5.2. The collection angle of the MBES is calculated to be 107°. The solid angle within which the photoelectrons can be collected by the MBES is shown in gray color. (Reprinted from Journal of Electron Spectroscopy and Related Phenomena, Vol. 195, Q Zhang etc. "High resolution electron spectrometers for characterizing the contrast of isolated 25 as pulses", Copyright (2014), with permission from Elsevier)

Furthermore, the transverse distributions of B_z are also measured and compared with the calculation at different distances, as shown in Fig. 5.4 and Fig 5.5. The black line shows the calculation result. The red and blue dotted lines show B_z from two orthogonal directions in the transverse plane perpendicular to the z axis. The agreement between the blue and reds lines demonstrates the symmetry of the real B field, and their agreement with the black lines show that the total B field is the same as the design. Therefore high resolution should be expected from the MBES.

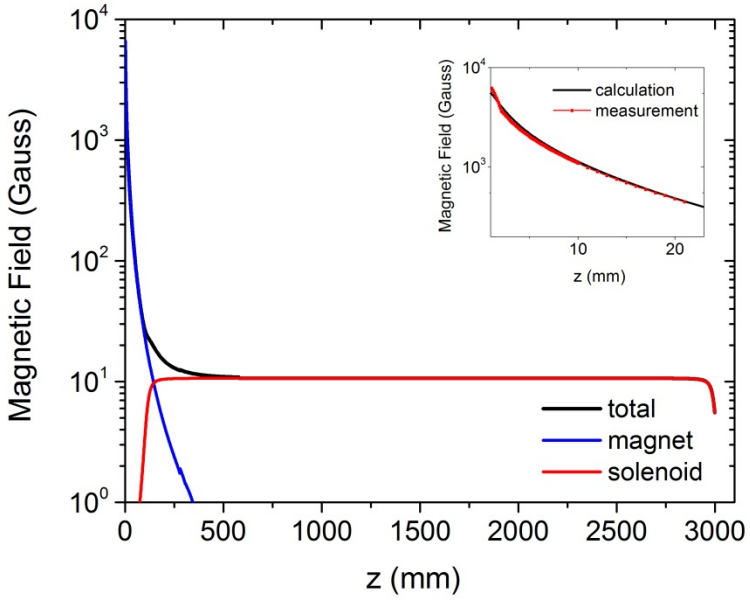

Figure 5.3 Calculated magnetic field along the z-axis (B_z). The blue line represents B_z generated from the permanent magnet, the red line shows B_z from the solenoid, and the black line is the total field of the two. Inset: comparison of calculation and measurement of B_z between z from 1 mm to 25 mm. The black solid line is the calculation and the red line with dot is the measurement.

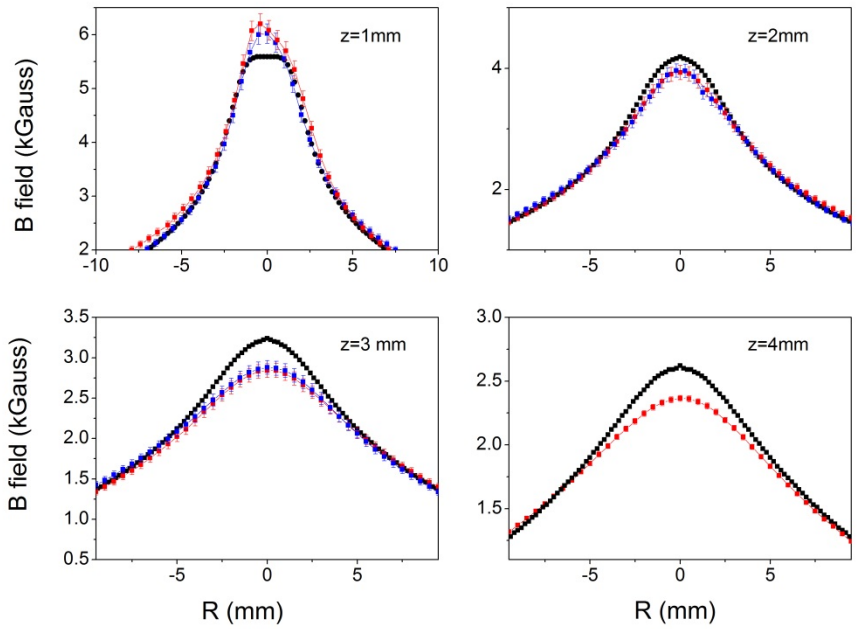

Figure 5.4 The comparison between the calculation and measurements of B_z in the transverse plane at distances from 1 to 4 mm. The black line shows the calculated result. The red and blue dotted lines show B_z from two orthogonal directions in the transverse plane which is perpendicular to the z axis.

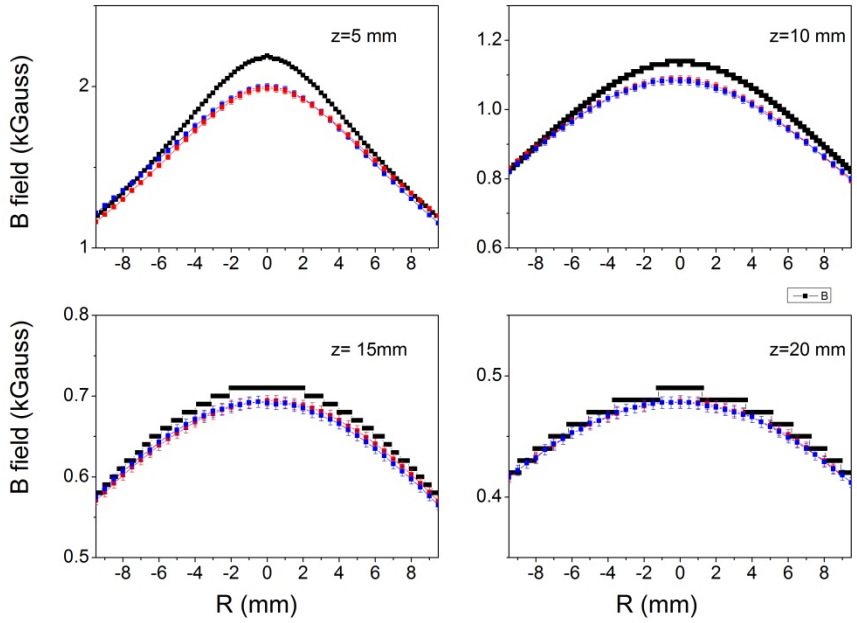

Figure 5.5 The comparison between the calculation and measurements of B_z in the transverse plane at distances from 5 to 20 mm. The black line shows the calculated result.

The red and blue dotted lines show B_z from two orthoganal directions separately in the transverse surface which is perpendicular to the z axis.

5.3 Resolution of MBES

For TOF spectrometers, the energy information is obtained through recording the flying time for electrons emitted along the TOF axis. Therefore, the energy and temporal resolution are actually equivalent for this discussion. For our MBES, the flight time accuracy is most obviously affected by the parallelization of the photoelectrons. Electrons with different emission angles take different times to reach the MCP. Therefore, there is an intrinsic resolution of the MBES determined by the equation [18], [66]

$$\frac{\Delta E}{E} = 2\frac{\Delta t_{MB}}{T} = \frac{B_f}{B_i} \approx 0.25\% \qquad (5.1)$$

where Δt_{MB} is the intrinsic temporal solution, T is the total flight time, B_f and B_i are final and initial B fields respectively. Note this equation is derived for the case of infinitely long flight distance after the parallelization. Of course, this is not practical. The longer the flight tube is, the better the temporal resolution is until reaching the limit set by equation 5.1. In our system, a three-meter-long flight tube was adapted considering the spatial limitation of the laboratory when it was designed.

The electron flight time as a function of emission angle was simulated by Simion software as shown in Fig. 5.6 (a) for an electron with kinetic energy of 150 eV [75]. The time for the electron will 0°emission angle is termed as T_0, and the flight time for other angles is termed as T_{TOF}. Figuew 5.6 (a) shows the ratio of T_{TOF} and T_0 as a function of the emission angle. It can

be seen that this ratio increases about 0.4% from 0° to 107°, indicating photoelectrons with larger angles take longer to reach the MCP.

In order to obtain the response function at this energy, the angular distribution of the photoelectron needs to be known. In our system, neon is used for producing photoelectrons due to its relatively high and flat photoionization cross section. The angular distribution of the photoelectrons can be expressed as [76]

$$\frac{d\sigma}{d\Omega} \propto 1 + \frac{\beta}{2}[3\,cos^2(\theta) - 1] \qquad (5.2)$$

where $\frac{d\sigma}{d\Omega}$ is the differential photoionization cross section, θ is the emission angle, and β is the asymmetric parameter. The asymmetry parameter β of neon can be obtained from Ref [51]. The angular distribution was plotted in Fig. 5.2 (b) to show the detection range of the MBES. With this information, combined with the relation of flight time and emission angle in Fig. 5.6 (a), we can calculate the response function at 150 eV, as shown in Fig. 5.6 (b).

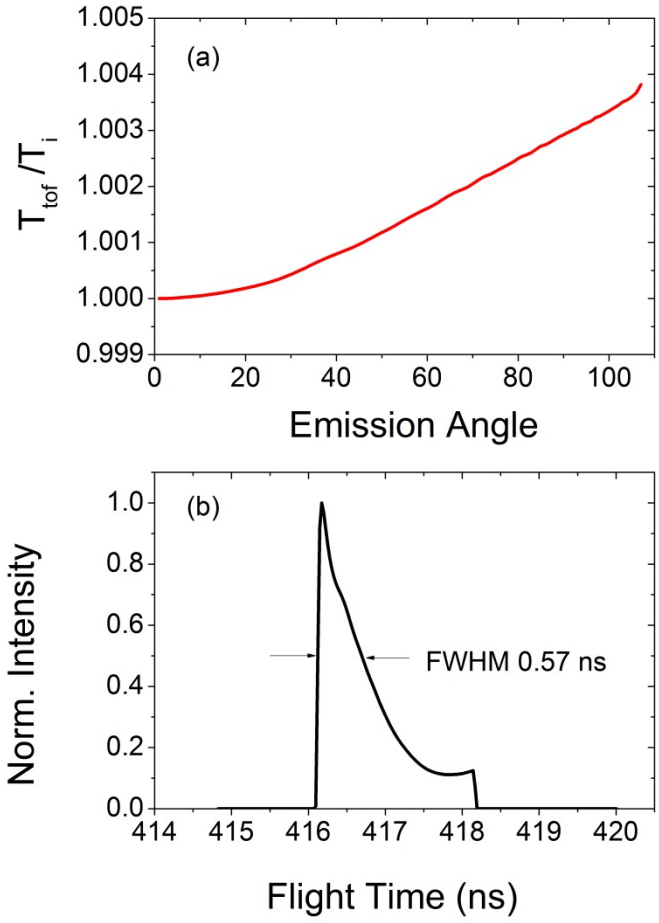

Figure 5.6 The calculated ratio between measured energy E_{TOF} and initial electron energy as a function of emission angle of the photoelectron.(b) The calculated response function of 100 eV electrons with all possible emission angles.

The FWHM of the response function is about 500 ps. The long tails are due to the electrons with large emission angle. It should be noted that the FWHM does not define the resolution correctly in this case since it cannot reflect the contribution of the long tail. Moreover, this response function only shows the spreading effect from the magnetic field, which is termed as Δt_{MB}. The final system resolution is its convolution with the temporal resolution of the data acquisition systems.

When a photoelectron travels through the flight tube and hits on the MCP, it can be amplified by the MCP, and a fast voltage signal is then generated. The amplitude of the signal voltage varies due to the cascading process of the MCP amplification. A Constant Fraction Discriminator (CFD) is then used to accurately determine the arriving time of the signal regardless of the varying amplitude. The analog system is then digitized by a Time-to-Digital-Converter (TDC), and the time histogram is stored in the computer. The resolution of the whole DAQ system can be determined by a third harmonic of the femtosecond IR laser [77]. A schematic drawing of the system is shown in Fig. 5.7. The UV light generated from a 25 fs laser can be seen as a delta function in time since it is much faster than the MCP response time. Then the spectrum collected from the TDC is the response function of the DAQ, as shown in Fig. 5.8. The FWHM of this spectrum is around 200 ps, which is two times smaller than the FWHM of the intrinsic response function of our MBES Δt_{MB}. In consequence, the DAQ resolution can be ignored for most of our discussion (except when extremely high kinetic energies such as 500 eV are considered).

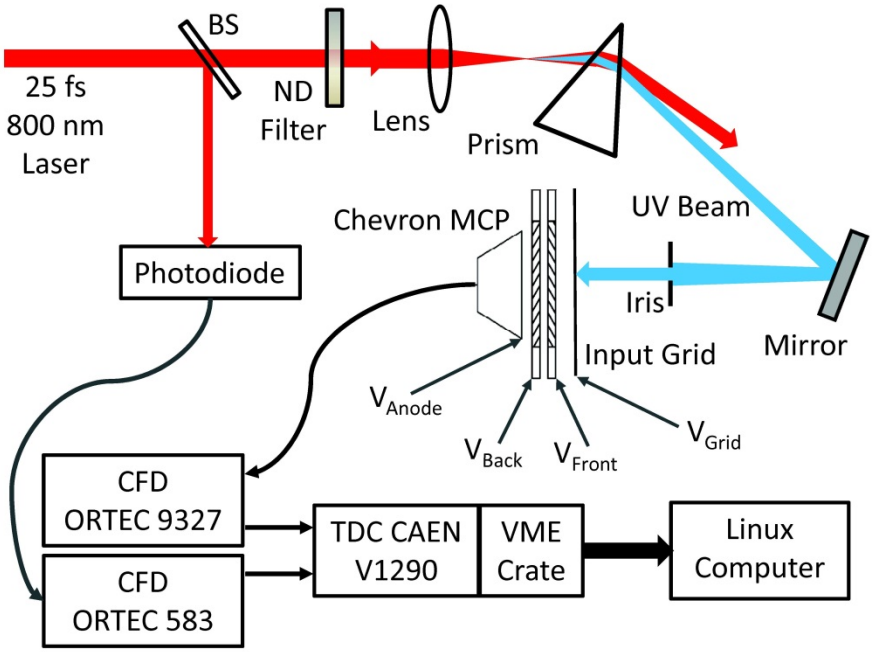

Figure 5.7 Experimental setup to measure the temporal resolution of the MCP electron detection system. Laser pulses of 25 fs at 800 nm are focused in air by a lens (f =100 mm) and generate UV photons at 267 nm. Part of the laser beam is reflected by a beam splitter (BS) to a photodiode. The laser intensity can be adjusted by a variable neutral density (ND) filter. A prism separates the 800 and 267 nm beams and the UV beam is reflected to the MCP detector by a mirror. The detector is housed in a vacuum chamber. Signals from the photodiode and the MCP were processed by two CFDs and sent to the TDC as the start and stop signals, respectively. A VME crate transmits the TDC data to a computer for analysis. (Reproduced with permission from [DETERMINING TIME RESOLUTION OF MICROCHANNEL PLATE DETECTORS FOR ELECTRON TIME-OF-FLIGHT SPECTROMETER, Review of Scientific Instruments **81**, 073112 (2009)]. Copyright [2009], AIP Publishing LLC, http://dx.doi.org/10.1063/1.3463690)

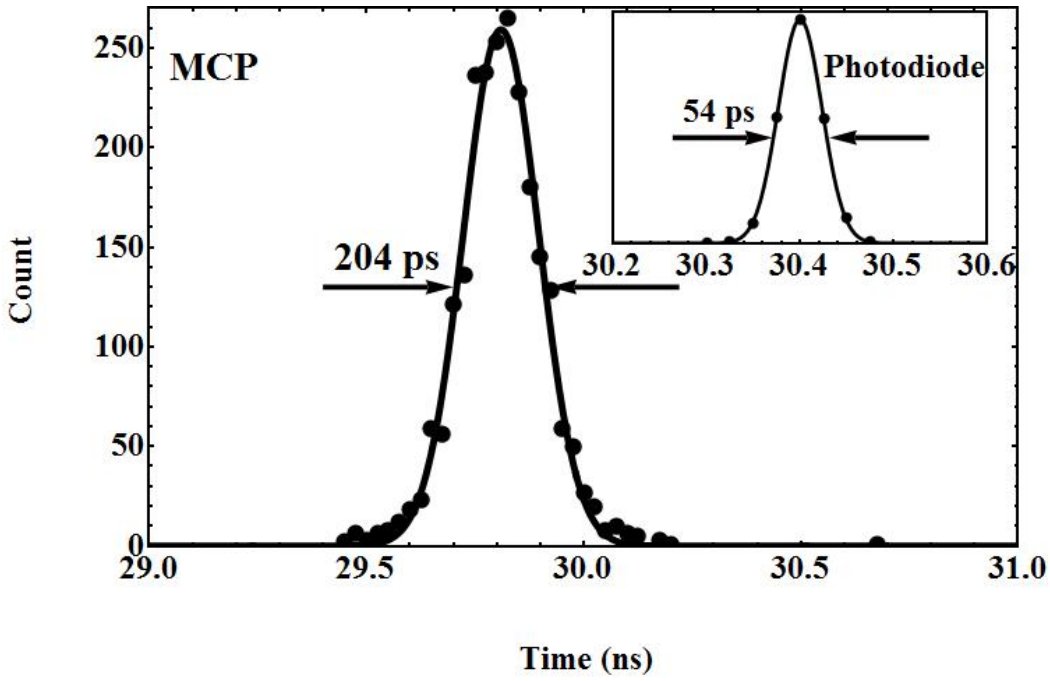

Figure 5.8 UV photon TOF spectrum (dots) obtained by the setup shown in Fig.1. The FWHM is 204 ps, obtained by fitting the experimental spectrum with a Gaussian function $Ae^{-(t-t_0)^2/2w^2}$, (solid curve) so that ΔT(FWHM) = 2.355w. The MCP voltage was 1800 V. The threshold of CFD 9327 was -75 mV. Inset: TDC spectrum (dots) obtained by feeding photodiode output through both 9327 and 583 CFDs. The FWHM is 54 ps, obtained by fitting the experimental spectrum with a Gaussian function (solid curve). (Reprinted from Q. Zhang, K. Zhao, and Z. Chang, "Determining Time Resolution of Microchannel Plate Detectors for Electron Time-of-Flight Spectrometer" Review of Scientific Instruments **81**, 073112 (2009))

Experimentally it is difficult to measure the spectrometer resolution directly due to the lack of a narrow band XUV light sources in most laser labs. However, certain comparisons between experimental results and simulations can still be made, and good agreements between them are observed. In the TOF spectrometers, the flight time can be increased by intentionally retarding the charged particles. In the MBES, two metal meshes separated by around 5 mm are placed right after the entrance of the solenoid wrap, as seen in Fig. 5.2 (a). The first mesh is grounded along with the magnet, gas jet, and cone. A retarding potential is applied to the second

mesh, which is electrically connected to the rest of the flying tube. Electrons flying with a retarding potential take longer time to reach the MCP, therefore increasing the resolution.

To test the resolution of the MBES, an intentionally stretched pulse from the Ti:Sapphire amplifier was used to drive HHG to produce narrow harmonic peaks at around 32.6 eV [78] Then a 30 V retarding potential was applied, as shown in Fig. 5.9 (a). For the harmonic peak around 33 eV, the measured spectrum should be the convolution of the response function of the MBES and the XUV harmonic peak. Since the latter one is unknown, we assumed a Gaussian spectrum in order to match the convoluted spectrum with the measurement performed with the 30 V retarding potential, as shown in Fig. 5.9 (b). Then the convolution can be done for the case of no retarding potential. The simulated and measured spectra are plotted in Fig. 5.3 (c) for comparison, and reasonable good agreement can be observed. The same agreement can be observed at 70 eV using a zirconium filter.

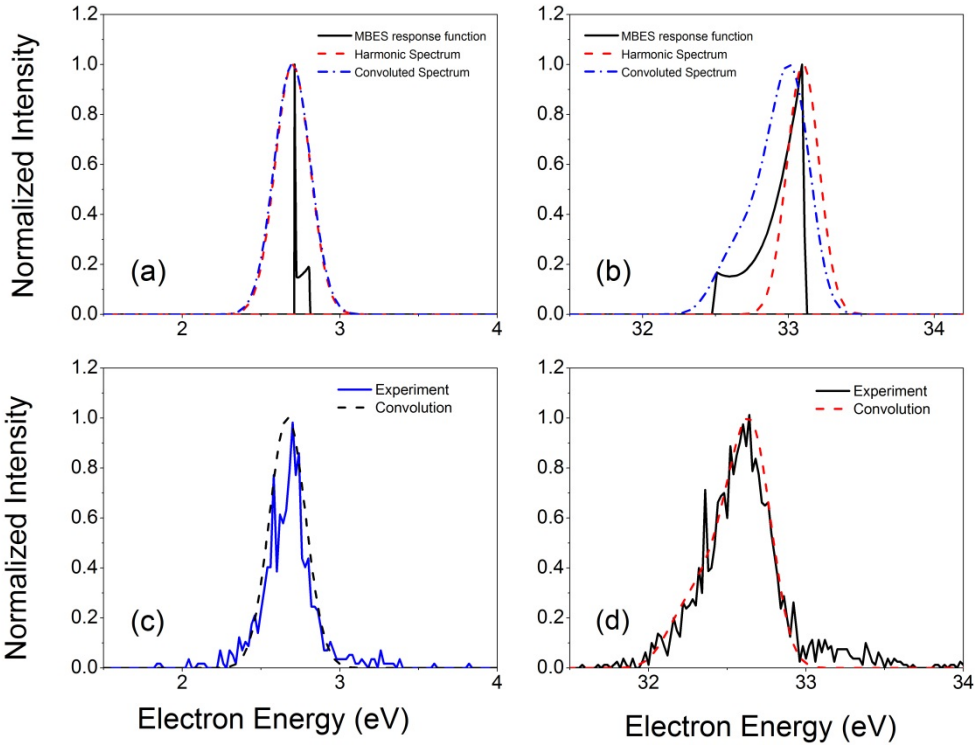

Figure 5.9 The comparison of experiment and simulation for harmonic peak at 32.6 eV. (a) The convolution (blue) of the MBES response function at 32.6 eV with 30 V retarding potential (black) and harmonic spectrum (red).(b) The convolution (blue) of the MBES response function at 32.6 eV with no retarding potential (black) and harmonic spectrum (red) (c) Comparison of experimental measurement of harmonic at 32.6 eV with 30 V retarding potential (red) and convolution (blue) from (a). (d) Comparison of experimental measurement of harmonic at 32.6 eV with no retarding potential (black) and convolution (red) from (b).

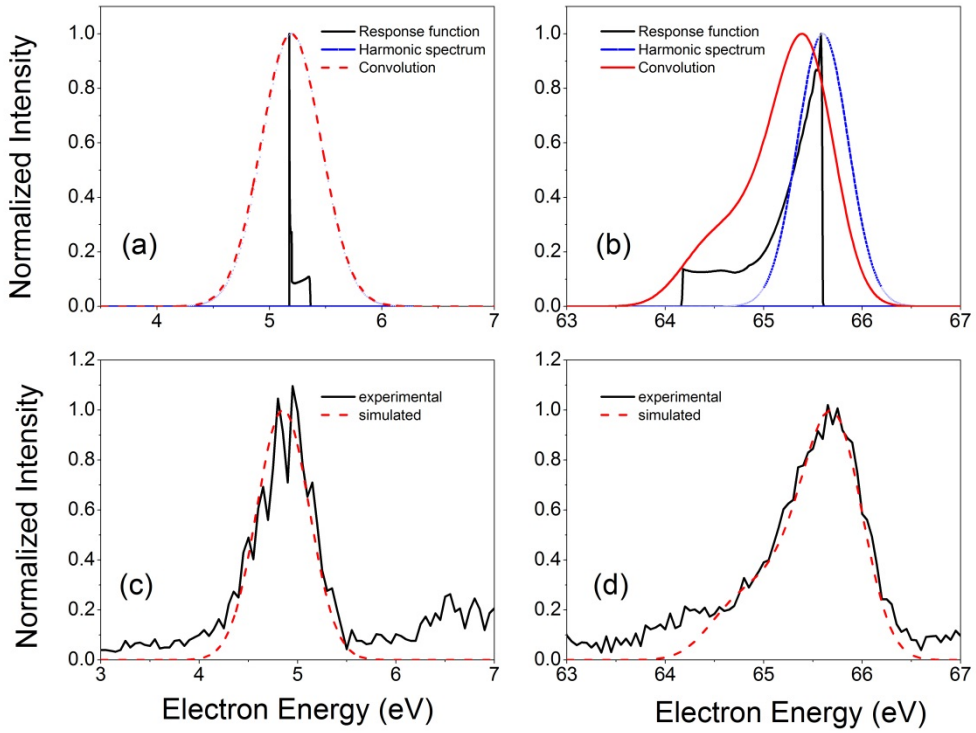

Figure 5.10 The comparison of experiment and simulation for harmonic peak at 65.7 eV. (a) The convolution (blue) of the MBES response function at 65.7 eV with 60 V retarding potential (black) and harmonic spectrum (red).(b) The convolution (blue) of the MBES response function at 65.7 eV with no retarding potential (black) and harmonic spectrum (red) (c) Comparison of experimental measurement of harmonic at 65.7 eV with 60 V retarding potential (red) and convolution (blue) from (a). (d) Comparison of experimental measurement of harmonic at 65.7 eV with no retarding potential (black) and convolution (red) from (b).

CHAPTER 6 GENERATION AND CHARACTERIZATION OF 67 ATTOSECOND PULSE

From Chapter 2 to Chapter 4, we discussed the principle of generating broadband supercontinuum with DOG, the methods for characterizing the attosecond pulse, and the experimental setup—the streak camera based on MBES with high resolution and collection efficiency. However, there is still one more thing that should be taken care of for generating short pulses: the attosecond intrinsic chirp. As discussed with the three-step model in Chapter 2, the electrons with different kinetic energy recombine with the parent ion at different times, as shown in Fig 2.3. Therefore, the attosecond XUV pulse emitted from HHG is chirped, as shown in Fig. 2.4. In order to achieve short pulses, this chirp must be compensated.

It is noted that besides solely using metallic filters [79], [80], other methods such as using gas, material chirp, or multilayer mirrors have been proposed and demonstrated experimentally [79], [81], [82]

6.1 Generation and Characterization of Isolated 67 Attosecond Pulses

As shown in the typical HHG experimental configuration depicted in Fig 5.1, a metallic filter with a thickness of hundreds of nanometers is usually used to block the remaining driving field while transmitting the XUV. The Group Delay Dispersion (GDD) of the filter is usually negative. Therefore, it is feasible to compensate the positive HHG intrinsic chirp with the negative GDD of the filters. Figure 6.1 plots the GDD as a function of photon energy for aluminum (Al), zirconium (Zr), titanium (Ti), and molybdenum (Mo) separately. The data for the calculation are from Ref [83]. Each filter has the same thickness of 300 nm. Among them, the Al

filter can only transmit photon energies up to 70 eV, making it unsuitable for generating the shortest attosecond pulses. However, it is the most robust filter of the group, so it is usually used to test the system. The Zr filter has a relatively higher transmission from 60 to 200 eV which is the spectral window where the HHG continuum usually covers. The GDD is also negative for lower photon energies and gradually reach to zero around 130 eV. As a result, the Zr filter is a good candidate for best compensation. Note that before 2012, the shortest single attosecond pulses (with duration of 80 as) were generated using the AG technique with a 300 nm Zr filter. The Ti filter is very similar to the Zr filter, but with lower transmission. The Mo filter transmits the XUV photon energy above 75 eV. So it is suitable to be used for compensating a supercontinuum generated at a higher energy band.

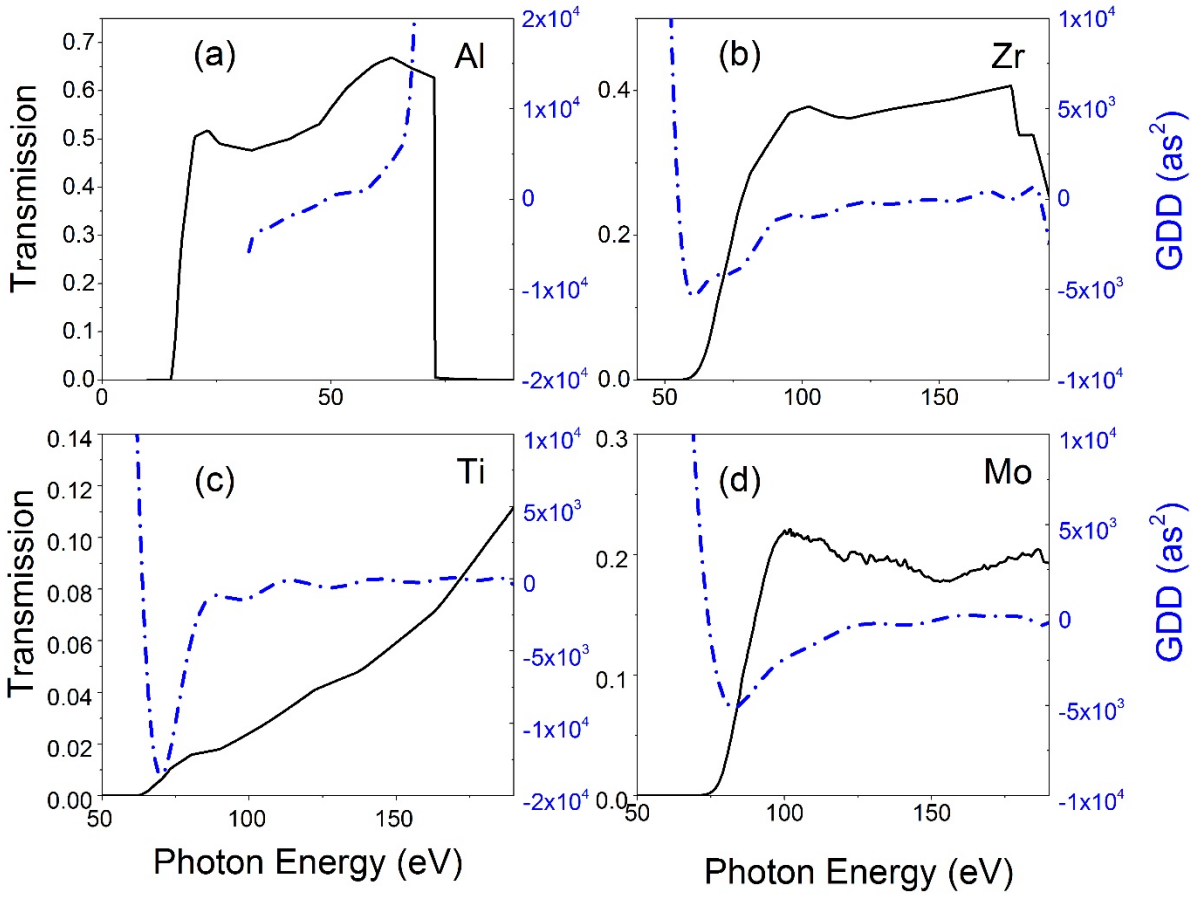

Figure 6.1 The transmission (black solid line) and material GDD (blue dash-dotted line) of (a) aluminum (b) zirconium (c) titanium, and (d) molybdenum.

Using metallic filters, the attochirp can be well compensated at lower energy which seems to lead to a low cutoff. However, higher peak intensity inside the gate of DOG is still needed for smaller attochirp. Therefore, an independent method for adjusting the spectral cutoff of the HHG is needed under the condition of high peak intensity.

It is known that in high-order harmonic generation, the observable spectral cutoff is not only determined by the response of individual atoms, but also by the coherent build-up of the XUV photons along the generating media. As a result, the true experimental cutoff under realistic conditions is usually smaller than the theoretically calculated value for a single atom.

The macroscopic cutoff can be expressed as $I_p + \alpha U_p$, with α smaller than 3.17 depending on experimental phase-matching conditions [84]–[86]. Therefore, intentional phase mismatch can be used to reduce the spectral region where the attochirp is not well compensated. Experimentally this is achieved by simply adjusting the gas pressure inside the gas media interacting with the driving laser.

A 7 fs IR laser with about 900 μJ pulse energy after the beam splitter (seen in Fig. 5.1) is used as the driving field with the Double Optical Gating technique. The beam size after the beam splitter is about 10 mm. An aperture with tunable diameter is used to limit the beam size for the highest count rate. This phenomena has been observed by many researchers [87]–[90]: the highest harmonic yield is reached with the balance of focal geometry and ionization (which favors smaller apertures) and the harmonic dipole amplitude and phase (which favors large apertures) [91]. In our experiments, a telescope is used to focus the beam, and it has been noticed there is considerable astigmatism at the focal point which can be eliminated by limiting the beam size after the aperture. Of course, a smaller beam size also leads to a lower peak intensity, so there is a trade-off. Experimentally, the optimal aperture size is determined on a daily basis to obtain a high cutoff as well as a reasonable count rate. Usually 500 μJ energy can be used after the pinhole for attosecond pulse generation, and the peak intensity inside the gate is estimated to be $1 \times 10^{15} W/cm^2$.

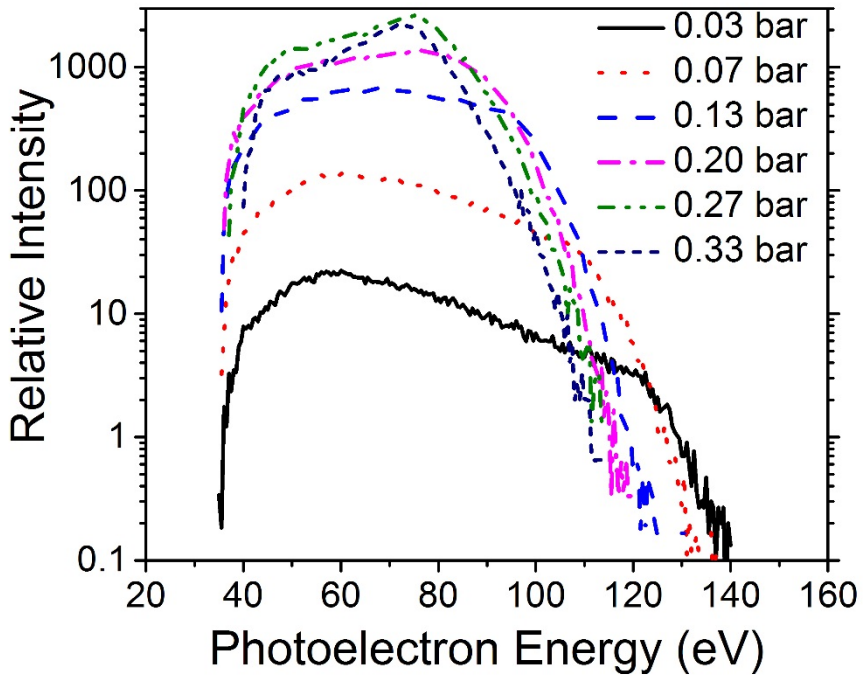

Figure 6.2 XUV photoelectron spectrum generated by DOG in Ne gas with six different pressures. The length of the gas cell is 1 mm. The peak intensity at the center of the polarization gate is about $1 \times 10^{15} W/cm^2$. (Reproduced from Zhao, Zhang, Chini, Wu, Wang & Chang, "Tailoring a 67 attosecond pulse through advantageous phase-mismatch. Optics Letters", 37(18), 3891, 2012)

Under this condition, the photoelectron spectra with different gas pressure were recorded by the MBES, as shown in Fig. 6.2. The Neon gas was used as the generating media, as discussed in Chapter 3. It can be seen that when the neon backing pressure in the gas cell was tuned from 0.03 to 0.33 bar, the cutoff photon energy was observed to decrease from 160 to 120 eV, corresponding to $I_p + 2.6U_p$ to $I_p + 1.8U_p$. If a proper backing pressure was chosen, the HHG spectrum covered the bandwidth which can be best compensated.

As shown in Fig. 5.3, the GDD of a 300 nm Zr filter (pink dashed line) and the attochirp (blue solid line) calculated with a peak intensity of $1 \times 10^{15} W/cm^2$ are plotted. It can be seen

that the GDD of the filter is negative below 130 eV, which can compensate the positive attochirp. In contrast, at an energy higher than 130 eV, the chirp is not well compensated. Therefore, the spectrum (red solid line) should be chosen to match the area where the attochirp is best compensated for generating the shortest attosecond pulses.

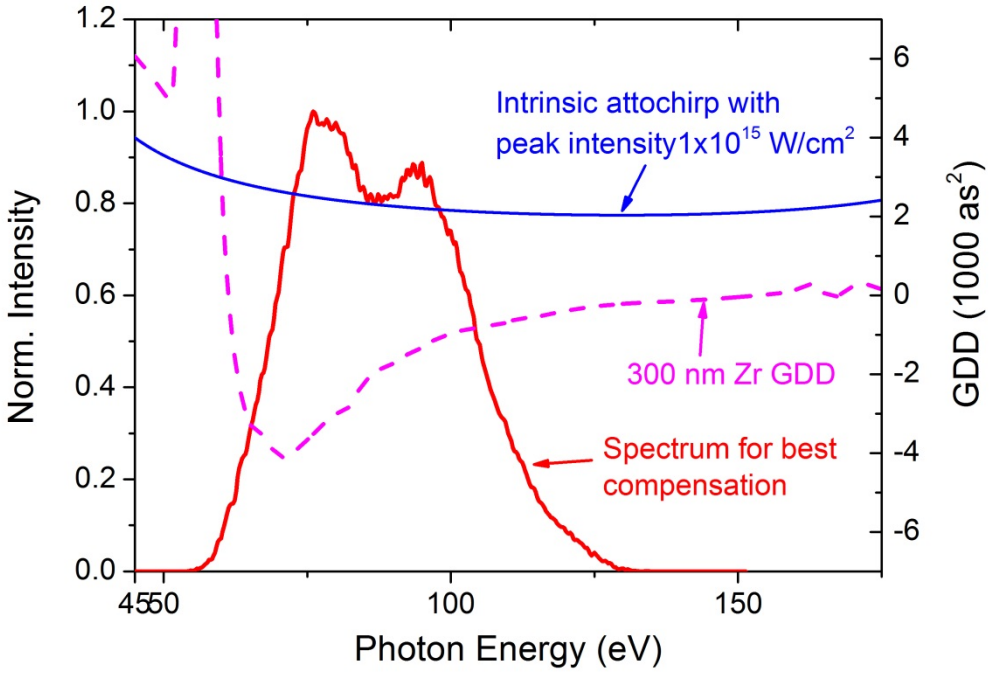

Figure 6.3 Attosecond intrinsic chirp compensated by a 300 nm Zr filter. The spectrum is specially chosen to cover the area where the attochirp is best compensated. Black solid line: XUV spectrum taken with 300 nm Zr filter. Red dashed line: intrinsic chirp of the attosecond pulses. Blue dash-dotted line: GDD of 300 nm Zr filter.

From Fig. 6.2, it can be seen that the backing pressure of 0.2 bar should be used in the streaking experiment for the best match with the spectral range where the Zr filter can best compensate the attochirp. An attosecond streaking experiment was done under this condition to characterize the pulse duration. The streaking trace was shown in Fig. 6.4 (a), and retrieved spectrum and temporal phase are shown in Fig. 5.6 (c) and (d) respectively. The CRAB and

PROOF methods were both applied to the experimental data and the same result of a single 67 as pulse was obtained. In Fig. 5.6 (b), the filtered streaking trace with one omega frequency $I_{\omega_L}(v,\tau)$ (left) was compared with the retrieved one (right). The good agreement between those two indicates the validity of the retrieval.

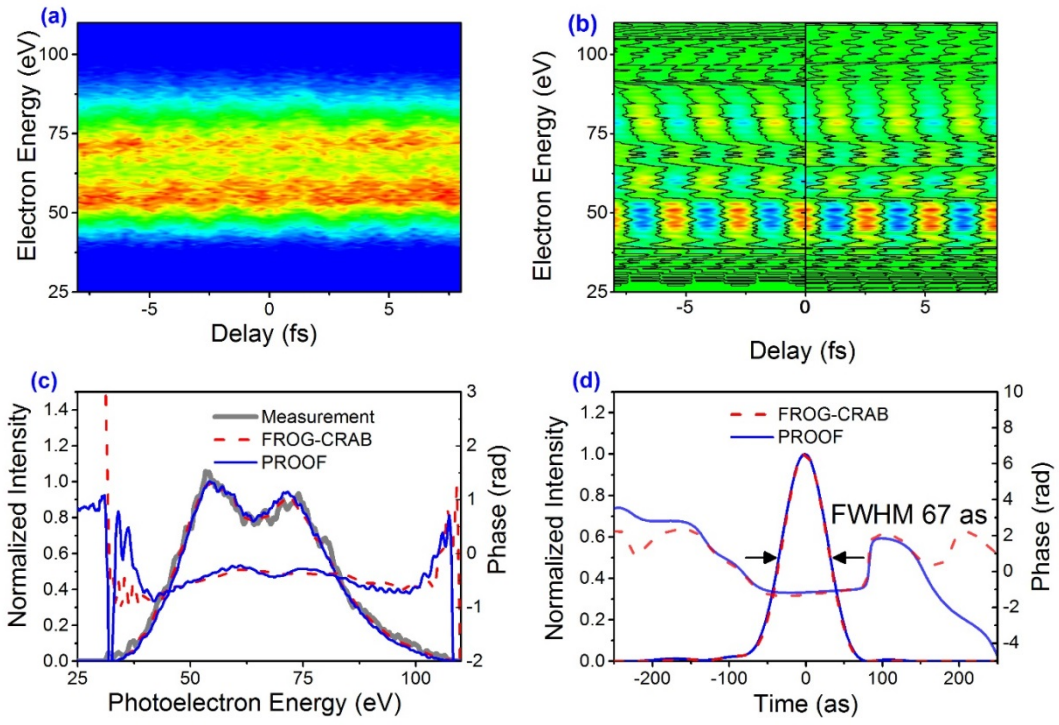

Figure 6.4 Characterization of a 67 as XUV pulse. (a) Streaked photoelectron spectrogram obtained experimentally. (b) Filtered $I_{\omega_L}(v,\tau)$ trace (left) from the spectrogram in (a) and the retrieved $I_{\omega_L}(v,\tau)$ trace (right). (c) Photoelectron spectrum obtained experimentally (thick grey solid) and retrieved spectra and spectral phases from PROOF (blue solid) and FROG-CRAB (red dashed). (d) Retrieved temporal profiles and phases from PROOF (blue solid) and FROG-CRAB (red dashed). (Reproduced from Zhao, Zhang, Chini, Wu, Wang & Chang, Tailoring a 67 attosecond pulse through advantageous phase-mismatch. Optics Letters, 37(18), 3891, 2012)

CHAPTER 7 ROUTE TO ATTOSEOCND PULSES WITH ONE ATOMIC UNIT OF TIME

With the Double Optical Gating technique, we have successfully demonstrated a single isolated 67 as pulse. However, to reach even shorter pulse durations like 25 as, or one atomic unit time, there are significant technical challenges.

First of all, for a transform-limited Gaussian pulse, 25 as in the time domain corresponds to a 75 eV FWHM in the spectral domain, which means that a total bandwidth of about 150 eV is required. As discussed in Chapter 6, a Zr filter cannot be used for even shorter pulses since the attochirp cannot be well compensated at energies above 130 eV. In addition, it filters out low energy photons. Therefore, in order to reach 150 eV bandwidth, the photon spectrum needs to extend to over 200 eV. This means higher peak intensities of the driving laser should be used and a better filter for phase compensation needs to be implemented. It is noted that the attochirp is inversely proportional to the intensity. Therefore, increasing intensity will benefit our goal in both ways.

Secondly, the resolution for accurately retrieving a 25 as pulse is not easy to experimentally achieve for such a high energy range. Simulations have been done to quantitatively determine the necessary resolution for retrieving the contrast of isolated attosecond pulse with 1% accuracy. A new type of MBES has been proposed to meet this requirement, and preliminary results were obtained.

Finally, a new scheme for suppressing the driving field while transmitting the XUV has been proposed to replace the metallic filters. This new scheme allows the transmission of photons

within the entire XUV spectral range, unlike the metal filters where only part of the photons can be utilized. This new scheme is very useful to generate a super-broadband continuum spectrum.

In this chapter, we present the preliminary results regarding the route to achieving pulses with a temporal duration of one atomic unit, discussing the three aspects mentioned above.

7.1 Broadband Supercontinuum Generation with Lens Focusing

In order to generate an even broader-bandwidth attosecond continuum, higher intensity is needed inside the gate. The easiest way is to use a tighter focusing configuration for the input driving laser. However, due to space limitations, further shortening the focal length using the two-mirror configuration would introduce significant astigmatism. To reduce the astigmatism, a lens can be used. However, it is commonly accepted that using lenses in ultrafast optics field leads to a distortion of wavefront and a broadening effect of the pulse duration at the focus, due to the material dispersion. However, it has been recently shown with calculation that pulses as short as 5 fs can be obtained at the focus as long as the input beam size and the focal length are properly chosen [92].

Following the same procedure in Ref [92], we calculated the pulse duration near the focus using the realistic parameters in our experiment. The input pulse is assumed to be a transform-limited 7 fs Gaussian pulse and a 140 mm focal length was chosen. The beam size of the input beam is assumed to be 6 mm in diameter, which is roughly the same as the current case after the aperture. Therefore, the same pulse energy of around 500 μJ should be expected for the lens focusing. As shown in Fig. 7.1, both the pulse duration and the spectrum at the focus are nearly identical to the input beam. The lens here works like a slab with the same thickness to the driving

pulse. Therefore, a lens can be used in generating supercontinuum spectra and single attosecond pulses.

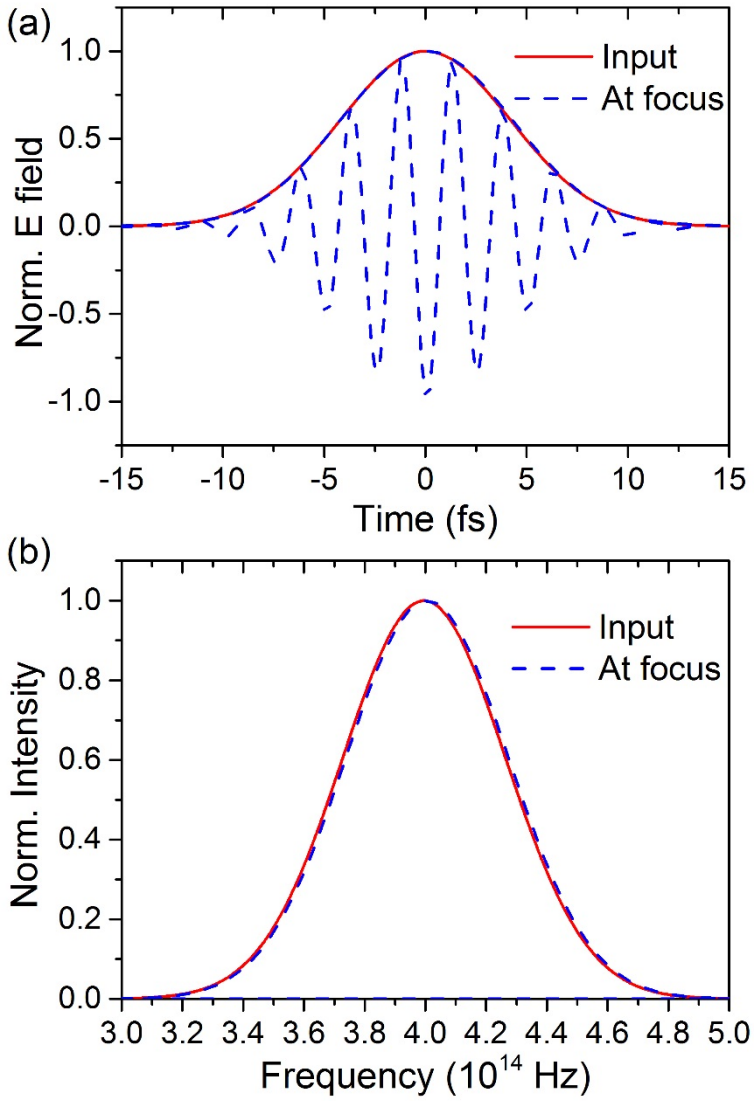

Figure 7.1 Performance of the lens focusing a 7 fs TL input pulse, with a 3 mm beam waist on the lens surface. (a) The electric field in the temporal domain. Red solid line: input field. Blue dashed line: electric field at the focus. (b) The laser spectra. Red solid line: input field. Blue dashed line: electric field at the focus.

The new experimental configuration with the lens focusing is plotted in Fig. 7.2. The gold-coated flat mirror after the toroidal mirror was removed to increase the photon flux for

generating photoelectrons. Under this condition, a photoelectron spectrum was taken by our TOF spectrometer with a Mo filter, as shown in Fig. 5.8. The cutoff extended to 180 eV photon energy, supporting 40 as pulses. The reason why the Mo filter was used here is that Mo filter provides better phase compensation at higher photon energies.

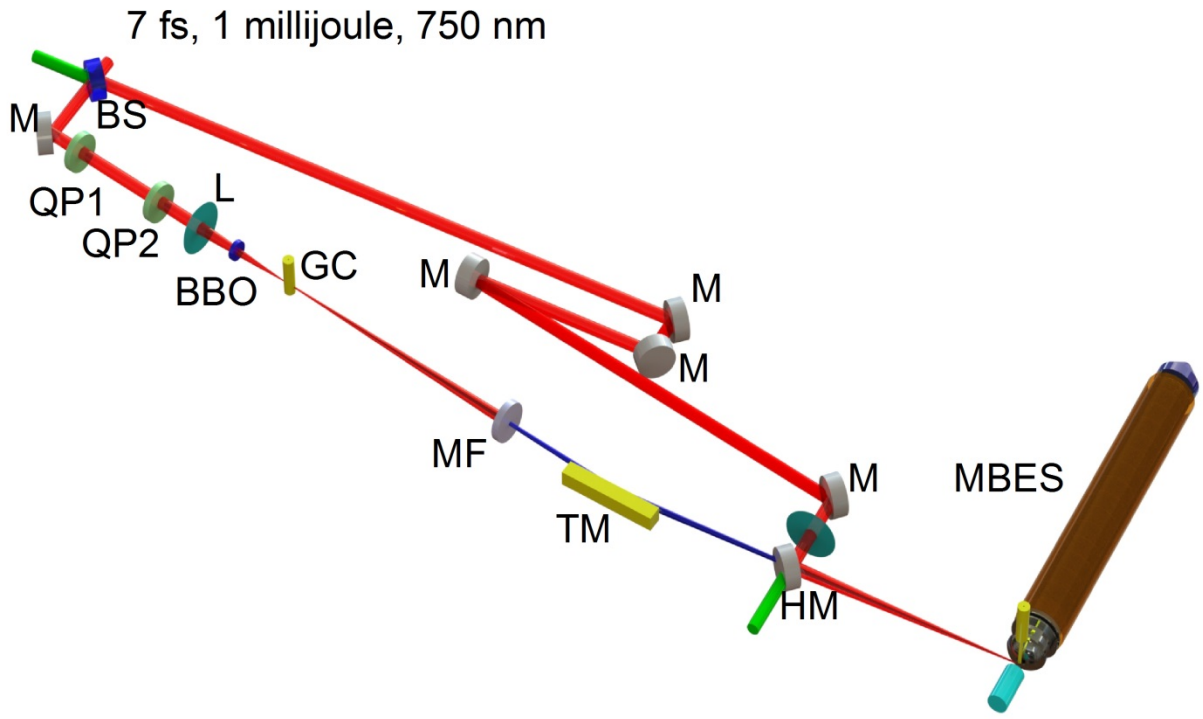

Figure 7.2 A schematic drawing of the experimental configuration with the lens focusing configuration. BS: Beam Splitter; QP: Quartz Plate; M: Silver Mirror; L: lens with 140 mm focal length; GC: Gas Cell; MF: Metallic Filter; TM: Toroidal Mirror; HM: Hole drilled Mirror; MBES: Magnetic Bottle Electron Energy Spectrometer.

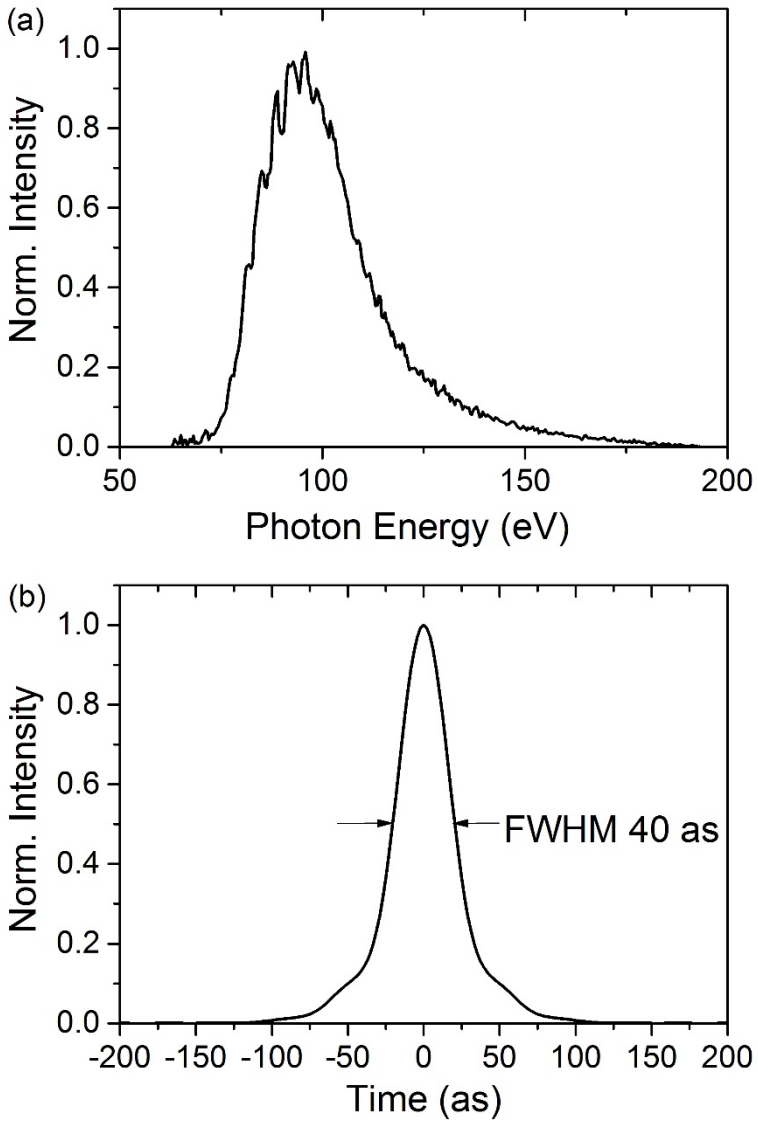

Figure 7.3 The supercontinuum spectrum measured with a 140 mm focal lens and a 300 nm molybdenum filter. The cutoff has extended to 180 eV photon energy. (b) The Fourier-transformed temporal spectrum assuming a TL pulse duration for the spectrum in (a). The FWHM is 40 as.

7.2 Characterizing the Contrast of 25 Attosecond Isolated Pulses

Isolated attosecond pulses can be used in pump-probe experiments to study fast electron dynamics. This requires that the system cannot be disturbed besides the pump or probe beam.

However, for attosecond generation from HHG, it is always the case that certain satellite pulses are generated along the main pulse, regardless of which gating technique is adopted. Therefore, it is important to know the relative intensity of those satellite pulses. Typically the intensity of those satellite pulses should be less than 10% of the main pulse to avoid disturbing the system under investigation by the attosecond pump-attosecond probe experiments. To accurately characterize the contrast of the attosecond pulse, there is one key factor for consideration, which is the experimental spectral resolution, especially for 25 as pulses due to the ultra-broad spectral range.

We simulated a 25 as transform-limited (TL) Gaussian pulse, with central energy at 150 eV, having pre- and post-pulses with 1% intensity contrast to the main pulse. The satellite pulses are set to be 50 as in duration since the satellite pulses are usually generated with lower intensities. With the DOG technique, the satellite pulse should be one full optical cycle away from the main pulse, since the second harmonic break the symmetry of the driving laser. The central wavelength of the driving laser is assumed to be 750 nm, which is the case for Ti:Sapphire lasers. Therefore, the satellite pulses are 2,500 as away from the main pulse, as depicted in Fig. 7.4 (a) (blue solid line). The Fourier-transform spectrum is shown in Fig. 7.4 (b) (blue solid line), which extends from 30 eV to 220 eV. However, the spectrum can only be measured experimentally with limited resolution. As a result, the final measurement should be the convolution of the real spectrum and the MBES resolution, as discussed in Chapter 5.3. Since the resolution depends on the spectral energy, the convolution is done by multiplying each element in the spectrum by its corresponding response function and then adding them together. Each response function has to be normalized to its area before the multiplication to ensure the equal weight for all energies.

The red dashed line in Fig. 7.4 (b) represents the spectrum after the convolution. Obviously it can been seen that the interference depth is reduced due to the limited instrumental resolution.

To retrieve the satellite pulse contrast in the temporal domain, it is not sufficient to perform a Fourier transform. Instead, a streaking spectrogram is generated with the XUV pulse and a 5 fs, 750 nm near-infrared (NIR) streaking pulse which has a peak intensity of $5 \times 10^{11} W/cm^2$. The spectrum at each delay in the streaking spectrogram is independently convoluted with the response function. Then the spectrum phase is characterized by the FROG-CRAB technique, and the retrieved temporal intensity profile is plotted in Fig. 7.3 (a) (red dashed line), as a comparison with the input pulse. It can be seen that the satellite pulse contrast retrieved from the convoluted spectrum is only 0.16%, much smaller than the 1% true value. The reason is the interference pattern between the satellite pulses and the main pulse is greatly smeared out by the response function. Therefore, retrieval from the recorded spectrum significantly underestimate the satellite pules contrast. (Best seen from the inset of Fig. 7.4 (b)).

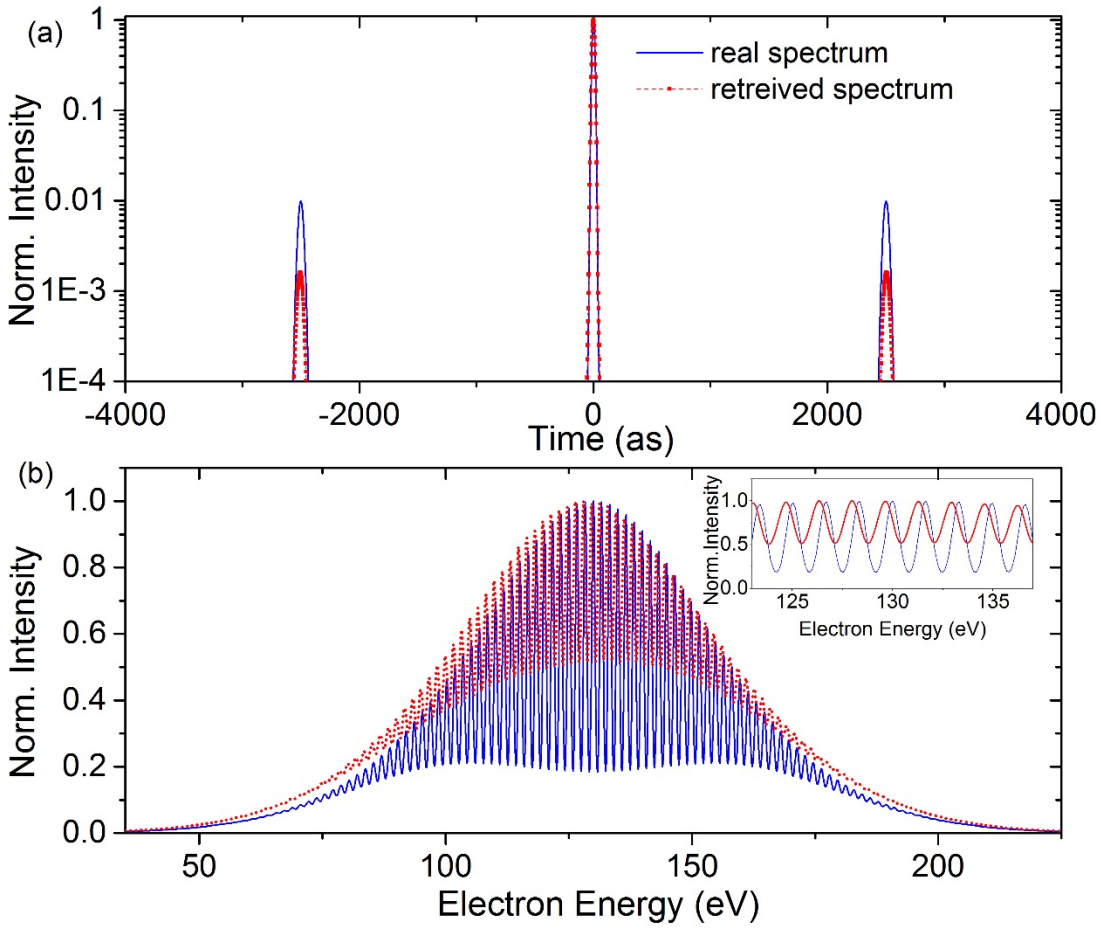

Figure 7.4 Effects of the response function on characterizing satellite pulses (1% satellite pulse is assumed). (a) The blue solid line shows the input temporal pulse. The red dashed line with dot is the retrieved temporal pulse from the streaking trace. (b) The blue solid line shows the spectrum of the input pulse, and the red dashed line is the convoluted spectrum in a 3 m TOF. Inset shows the enlarged spectra from 120 to 140 eV.

Our simulation indicates that for 25 as pulses, better spectral resolution is desired for the accurate characterization of the satellite pulses. To improve the spectrometer resolution, one commonly increases the length of the flight tube of MBES. As explained in Chapter 5.2, the photoelectrons with larger emission angles takes longer time to reach the MCP for detection. This deviation Δt are contributed from two parts: Δt_1, the term before the parallelization

(roughly from 0 to 100 mm from the photoelectron birthplace), and Δt_2, the term after the parallelization (farther than 100 mm away). Increasing the length of the flight tube actually increases Δt_2 proportional to the total flight time T, while keep the Δt_1unchanged. As a result, the overall ratio which determines the spectral resolution $\Delta t/T$ is smaller, hence improving the resolution. A comparison of the spectral deviation and response function (in other words, the instrumental resolution) at 150 eV for three-meter and eight-meter flight tubes are shown in Fig. 7.5. It can be seen that the eight-meter MBES clearly measures the electron kinetic energy more accurately, and the response function is narrower. Further simulation with the streaking trace retrieval shows that with an eight-meter-long flight tube, the retrieved 1% satellite pulse is 0.36%. Even though the satellite pulse is retrieved more accurately than with the three-meter flight tube, it is still three times smaller than the real value.

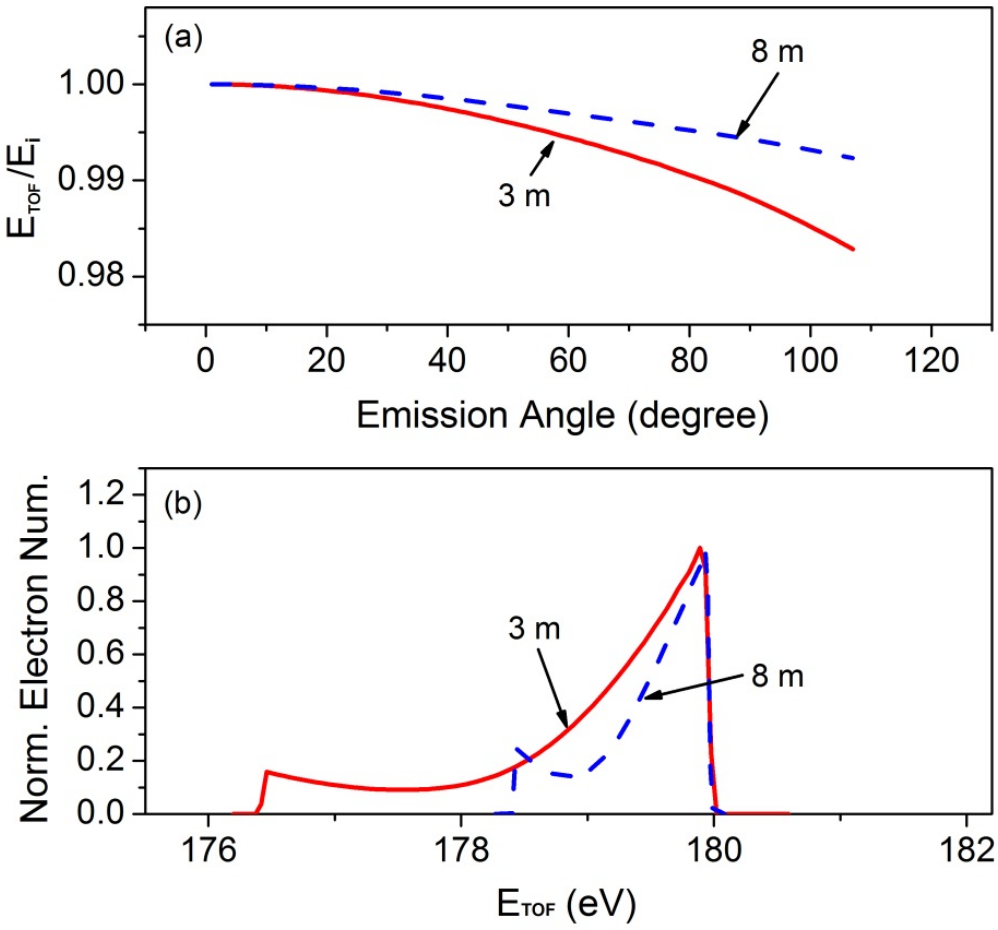

Figure 7.5(a) Ratio of the energy calculated from the flight time (E_{TOF}) to the real value (E_i) as a function of the emission angle. Electrons with emission angles larger than 107° cannot be detected by the MCP. (b) Energy distribution of 180 eV monoenergetic electrons calculated assuming the angular distribution of Ne photoionization with an asymmetric parameter of 1.4, which is referred to as the response function. The solid line is for a spectrometer with 3 m flight distance; and the dashed line is for an 8 m TOF. (Reprinted from Q Zhang, K. Zhao, and Z. Chang, "High resolution electron spectrometers for characterizing the contrast of isolated 25 as pulses". Journal of Electron Spectroscopy and Related Phenomena, **195**, pp 48-54. DOI: 10.1016/j.elspec.2014.05.008)

Further increasing the flight tube could not significantly improve the energy resolution because the error introduced during the increased flight distance starts to play a role. This means $\Delta t_2 \gg \Delta t_1$, therefore, $\frac{\Delta t}{T} \approx \frac{\Delta t_2}{T}$. In this scenario, increasing the length of the flight tube

increases the Δt_2 and T. However, their ratio $\frac{\Delta t}{T}$ and hence the spectral resolution stays unchanged.

Alternately, the response function of the TOF can be further improved by eliminating electrons with large emission angles. Actually, in the attosecond streaking experiment, electrons emitted with large angles are highly unwanted because the streaking effects decrease with emission angle. Electrons emitted with angles larger than 90° will be streaked in the opposite direction. Therefore it would be ideal to block the large angle electrons for both the benefit of the streaking data quality and energy resolution. Given the fact that electrons with larger emission angle deviate transversely away from the axis of the flight tube more as they fly in the magnetic field, a pinhole can effectively block those electrons. Theoretically the pinhole can be put anywhere between the generation point of the photoelectrons and the electron detector. However, experimentally it is much easier to put it at the beginning of the electron trajectory. We plotted the relation between the pinhole size and the collection angle as shown in Fig. 7.6 (a) and (b). The pinhole size varies from 0.15 to 0.4 mm and is placed 2 mm away from the electron birthplace. Then the new response function with different pinhole size can be calculated from the revised collection angle. Particularly, the response functions of 180 eV electrons for a 0.25 mm pinhole in an eight-meter TOF, are shown in Fig. 7.7. Comparing with the response function without the pinhole (red dashed line in Fig. 7.7), it can be seen that the long tail of the response function is eliminated, and the FWHM is 0.19 eV for the eight-meter TOF.

To study the effects of the pinhole size on the accuracy of satellite pulse contrast measurements, we simulated the streaking trace using the spectra convoluted with the new response functions and plotted the retrieved satellite pulse contrast as a function of pinhole size

in Fig. 7.8. To compare, the real value is also plotted for satellite pulses with intensities of 1% of the main pulses. This figure shows that as pinhole size decreases, the satellite pulse characterization becomes more accurate, as expected. Particularly, a 0.25 mm pinhole in an eight-meter TOF can be chosen to retrieve the satellite pulse ratio with less than 10% error. On the other hand, the collection efficiency is also reduced to 15%.

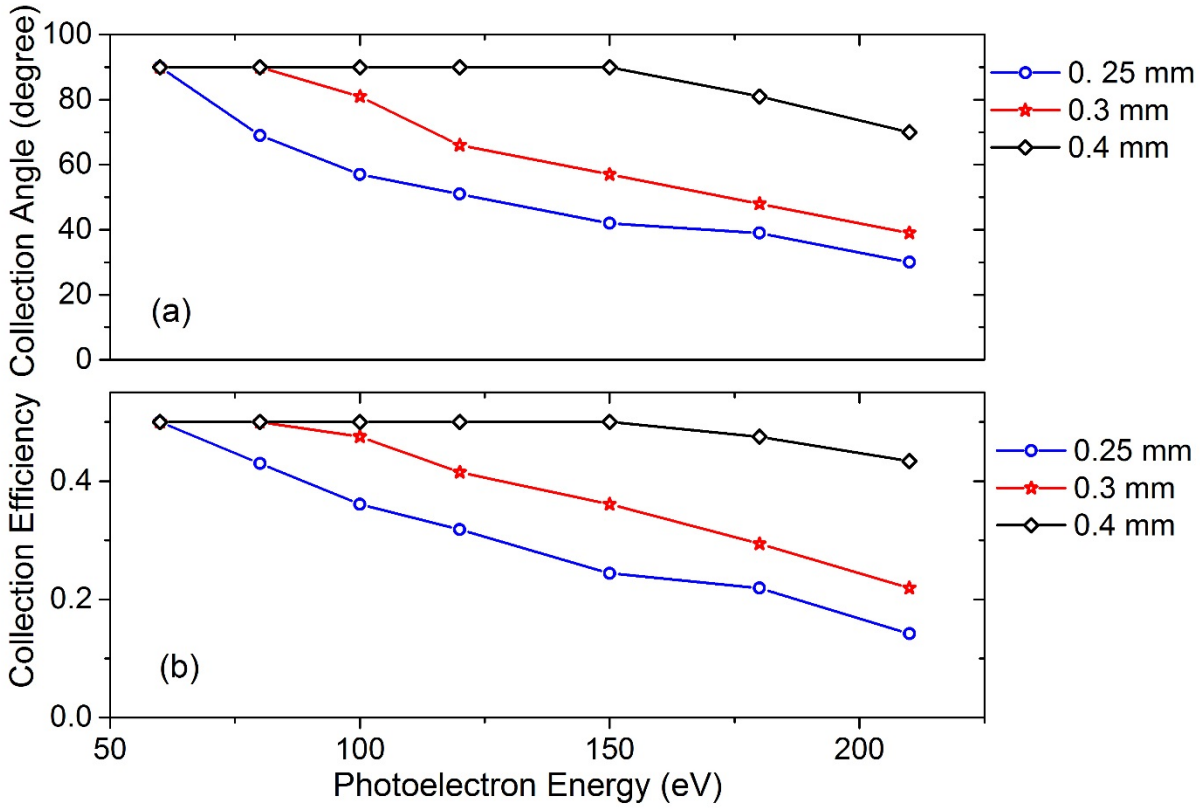

Figure 7.6 (a) Collection angle and (b) collection efficiency as functions of the electron energy for different pinhole diameters.

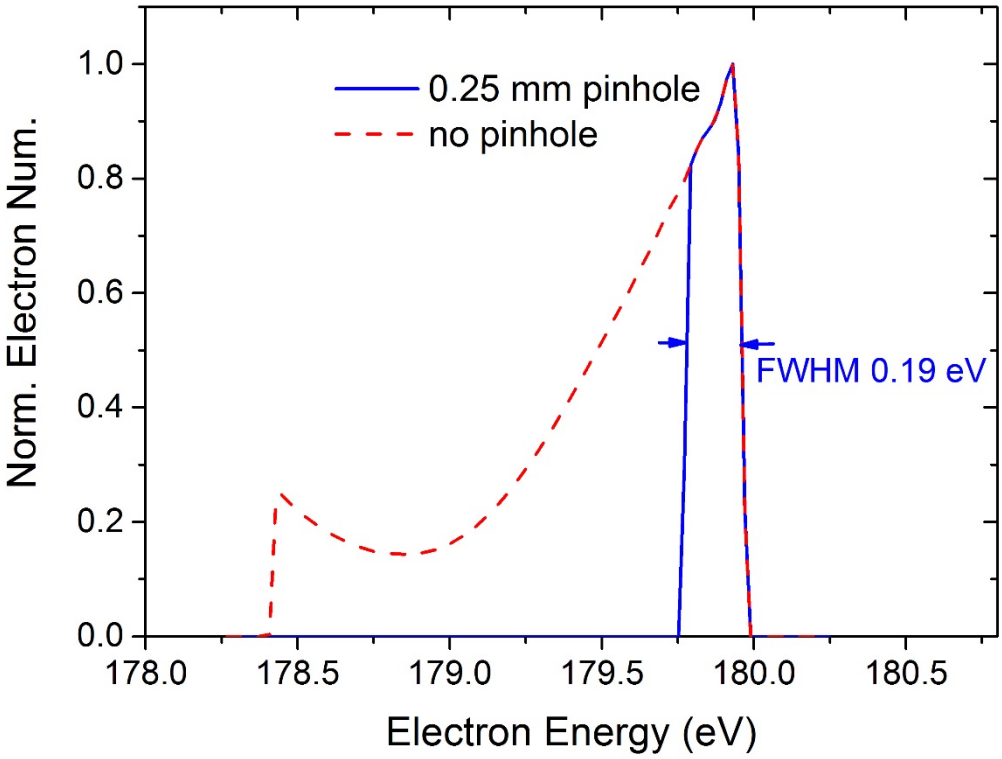

Figure 7.7 Response function calculated with a 0.25 mm pinhole in the 8 m TOF, for 180 eV electrons (blue solid line). The response function without is plotted with red dashed line for comparison.

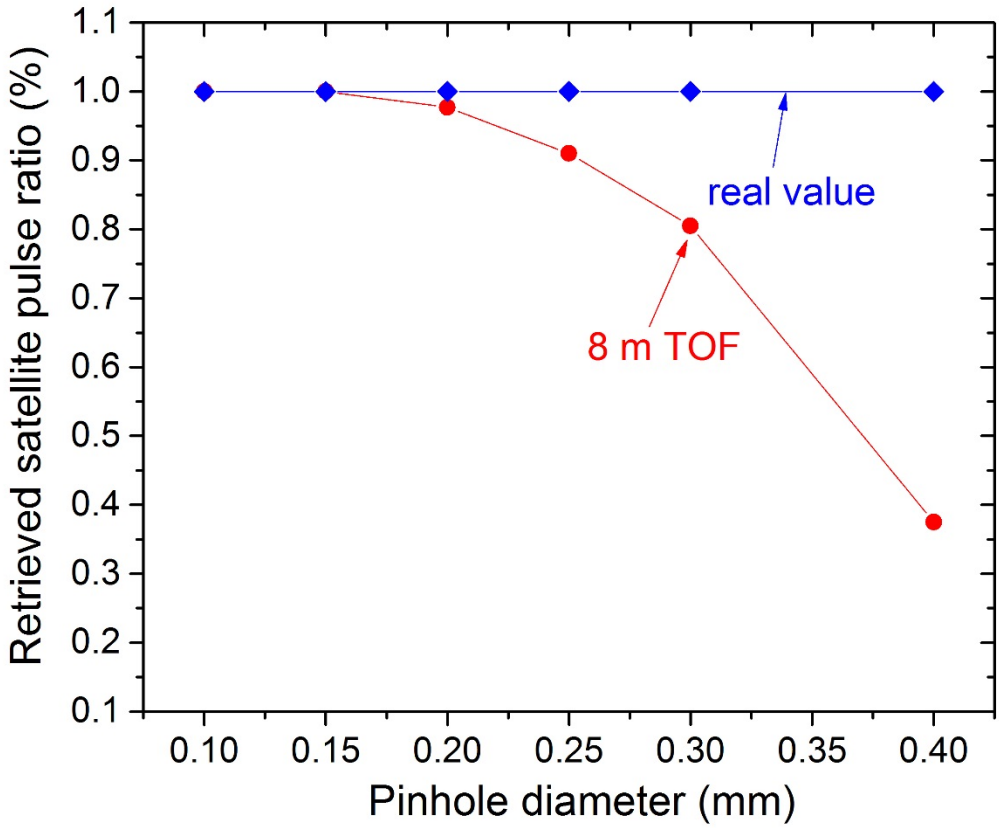

Figure 7.8 Comparison of the retrieved satellite pulse contrast limited by MBES resolution with real values. The red line with circles shows the retrieved contrast with an 8 m TOF. The blue line with diamonds shows the real value of 1% contrast as a comparison.

Experimentally it is difficult for us to evaluate the spectral resolution of our MBES directly. However, the relative collection efficiency can still be recorded and compared with our calculation. The simulation shows the collection efficiency is nearly the same for all the energies with cone sizes 0.5 mm or larger. Therefore, to retrieve the collection efficiency of a 0.15 mm cone, two spectra were recorded with a 0.5 mm and a 0.15 mm cone under the same condition. The intensity ratio between the two should agree with the calculated collection efficiency in Fig

7.6. As it can be seen in Fig. 7.9 (b), the agreement between the experiment and the calculation are reasonable. The difference between the two might be due to the fact that the photoelectrons are born in a line along the XUV propagation rather than a single spot. The offset of the electron starting position further complicates the problem and is difficult to simulate. Further experimental tests are still needed to best understand this process.

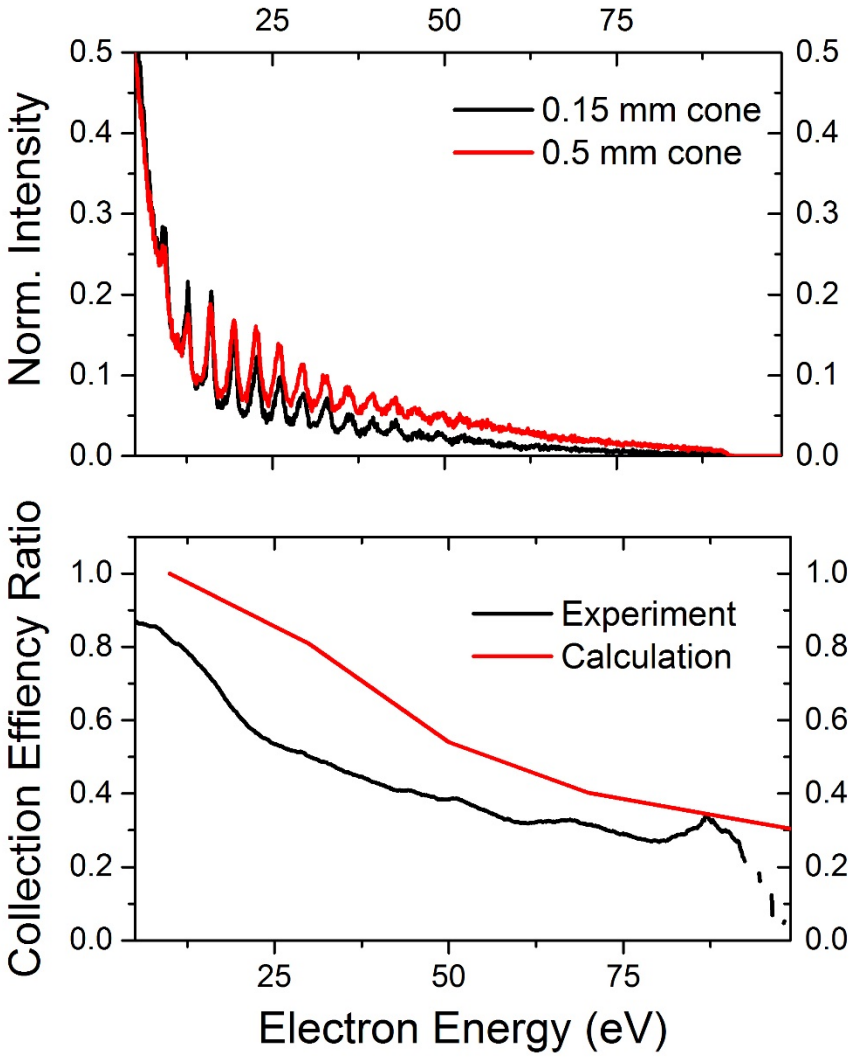

Figure 7.9 Experimental evaluation of the collection efficiency of the 0.15 mm and 0.5 mm cone. (a) The spectra taken with 0.15 mm (black solid) and 0.5 mm (red solid) cone size under the same condition. The 200 nm thick Be filter was used to block the IR and

select the energy range between 0~90eV. (b) The collection efficiency dependence on the electron energy for 0.15 mm. The black line shows the experimental result calculated from (a) and the red line shows the calculation from Fig 7.6.

7.3 Suppressing the Driving Laser with Microchannel Plate

As was discussed in previous chapters, the metallic filters were used to block the remaining driving field while transmitting the XUV photons. Since the conversion efficiency of the HHG is usually on the order of 10^{-4}~10^{-5}, the driving pulse energy is practically unchanged after HHG. Separating the driving pulse from the high-order harmonics is a long-standing problem for the attosecond community.

There have been several other proposals dealing with this issue besides inserting metallic filters. Using conical-shaped driving lasers, specially-designed beam splitters, Si/SiC plates at Brewster's angle, and XUV grating pairs can all successfully separate the IR and the XUV [93]–[96]. However, each one of those schemes has certain shortcomings.

As shown in Fig. 7.10 (a), a metallic filter is usually directly placed after the HHG gas cell to block the driving pulse (red) and transmit the generated XUV (blue). However, metallic filters only transmit the XUV photon within certain energy windows. For example, an Al filter only transmits XUV photons up to 72 eV. A Zr filter cannot transmit the XUV below 60 eV. Using this method, a significant portion of the supercontinuum bandwidth is lost. Moreover, the metallic filters are extremely fragile and easy to break. They are not suitable for blocking driving lasers with a pulse energy of 100 mJ or above.

Using an annular driving beam can perfectly separate the remaining driving laser without the issues posed by metallic filters. It is achieved by blocking the center portion of the incoming beam, and only the outside part is used to generate attosecond pulse, as shown in Fig. 7.10 (b). Obviously this is a huge waste, especially when higher pulse energy is employed in HHG.

It has also been proposed that using specially-designed multilayer beam splitters can solve this issue. However, this method only works for XUV photons below 75 eV. The same limitation applies to using Si/SiC plate at Brewster angle. A grating pair can be used for any photon energy. However, it only works with narrow band spectral range due to the spatial and temporal dispersion introduced. Schematic drawings for those two methods are shown in Fig. 7.10 (c) and (d) separately.

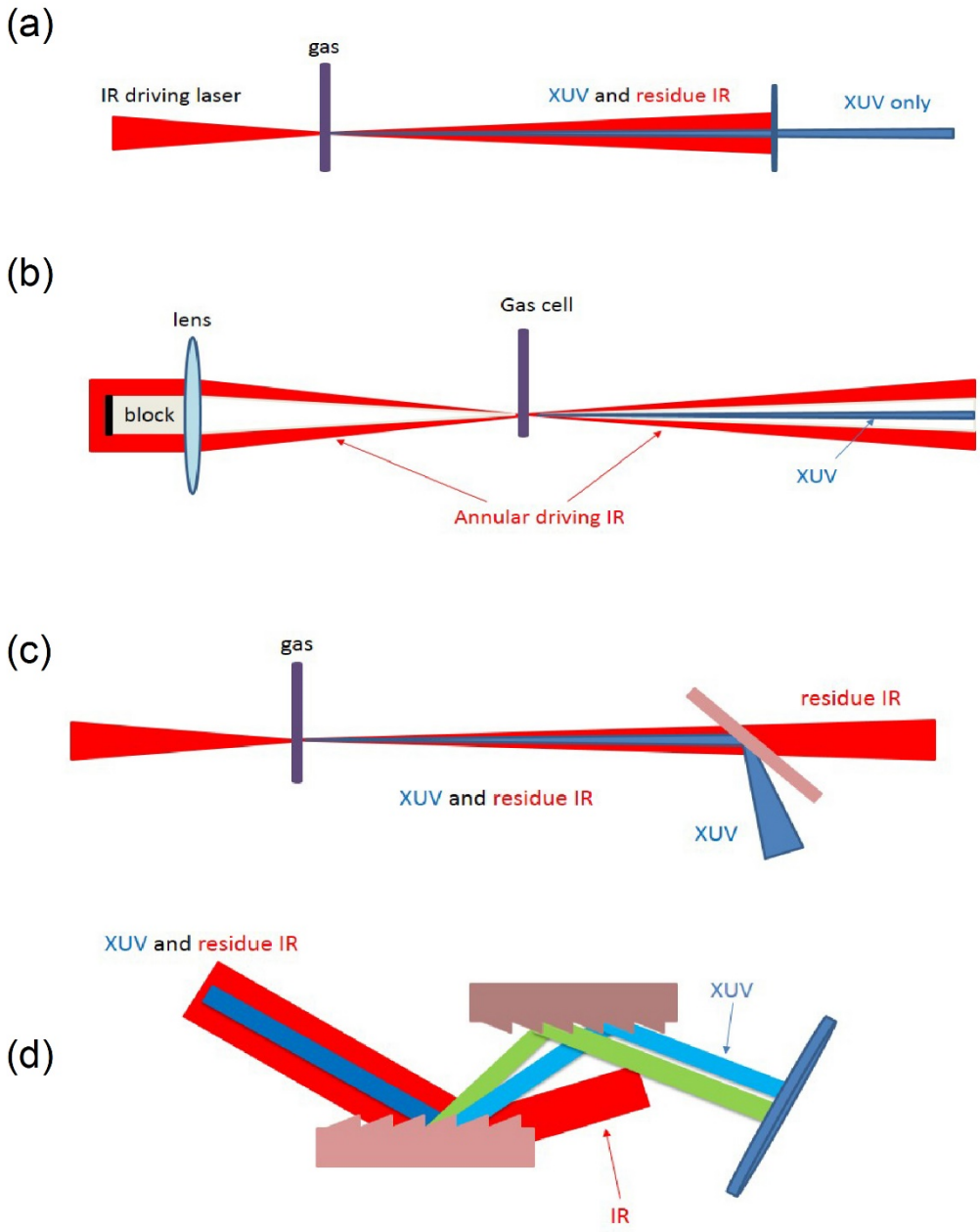

Figure 7.10 Schematic drawings of several common techniques for separating the driving IR and the generated XUV from the HHG. (a) Metallic filter. (b) Annular driving beam (c) multilayer beam splitter or Si/SiC plate on the Brewster Angle (d) Grating pairs.

Here, we propose a new scheme: using a Microchannel Plate as a short-pass filter to suppress the driving infrared laser relative to the XUV photons without any spectral limitation. Essentially an MCP consists of millions of parallel glass capillaries (microscopic channels) leading from one surface to the other [97]. The diameter of each channel inside the MCP is several micrometers, comparable to the wavelength of NIR/MIR but much larger than that of the XUV or soft x-ray photons. As a result, the driving laser experiences a significant diffraction effect after the MCP, while the XUV remains largely unchanged, meaning the transmission of the driving field should be significantly smaller than that of the XUV photons after the MCP. Therefore, the driving pulse is relatively suppressed. A schematic drawing of the principle of the MCP is shown in Fig. 7.11.

In order to demonstrate this new technique, the zero-order transmission of the MCP was measured as a function of wavelength. Three lasers with different wavelengths are available for testing the MCP transmission. The home-built Ti:Sapphire laser has a central wavelength of 750 nm and pulse duration of 23 fs. The MIR output from a commercial TOPAS has a central wavelength of 1.6 μm and pulse duration of 50 fs. A continuous-wave laser with a wavelength at 532 nm is also used. The measured zero-order transmission with these three different wavelengths are plotted in Fig. 7.10, varying from the lowest transmission of 0.4% for 1.6 μm to 11% for 532 nm wavelength. For the Ti:Sapphire laser, which is used for HHG in our current setup, the transmission is about 5%. Obviously the transmission is much larger for shorter wavelengths.

To separate the XUV and the driving pulse effectively, the transmission of the two through the MCP must be largely different. The total MCP transmission in the XUV spectral region has been measured to be as high as 60% for photon energies from 50 eV to 1.5 keV [98],

reaching the upper limit set by the MCP opening ratio. For photons with even higher energy, the transmission should be the same due to their shorter wavelength. In our scenario, only the zero order transmission should be used for studying ultrafast dynamics, and therefore the transmission should be evaluated carefully. Experimentally, we placed the filter in the same position as the metallic filter in our HHG beam line. Higher orders of the diffracted light were blocked by a hole mirror, and eventually only the zero-order transmission contributes to the photoelectron spectrum recorded by the MBES. The measured transmission was also plotted in Fig.7.12.

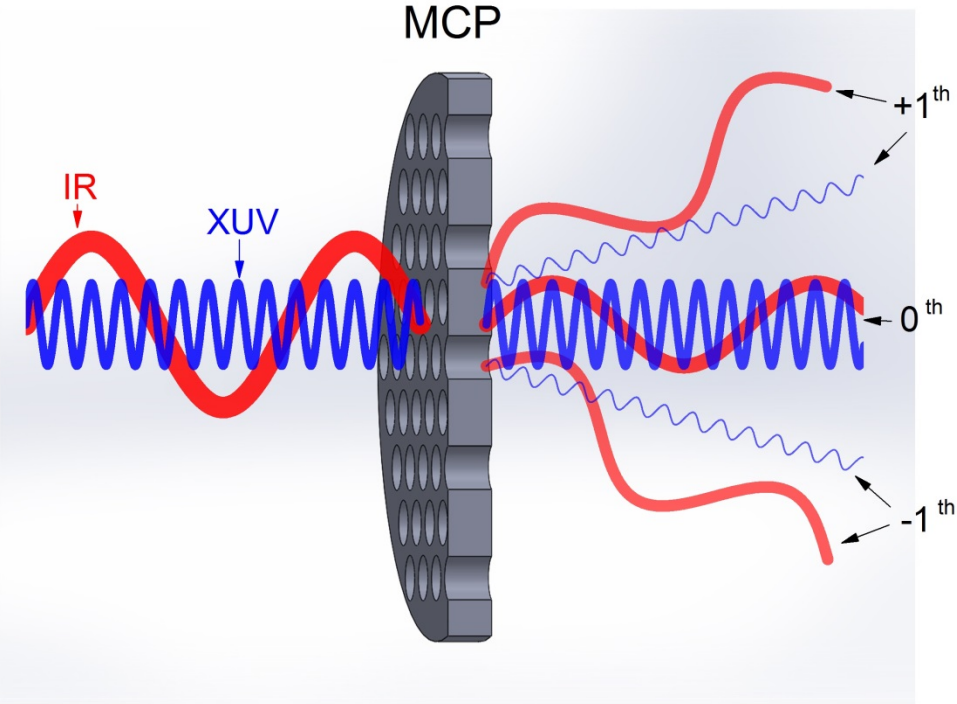

Figure 7.11 Schematic drawing of the principle of the MCP filter. The diameter of each MCP channel is comparable to the wavelength of the IR but much larger than that of the XUV. The red (blue) lines indicate the IR (XUV) beam. The 0th, ±1st order diffractions are labeled by black arrows. (Reprinted from Q Zhang, K. Zhao, J. Li, M. Chini, Y. Cheng, Y. Wu, E. Cunningham, and Z. Chang, "Suppression of Driving Laser in High Harmonic Generation with a Microchannel Plate". Opt. Lett. Vol. **39**, Issue 12, pp. 3670-3673 (2014), http://dx.doi.org/10.1364/OL.39.003670)

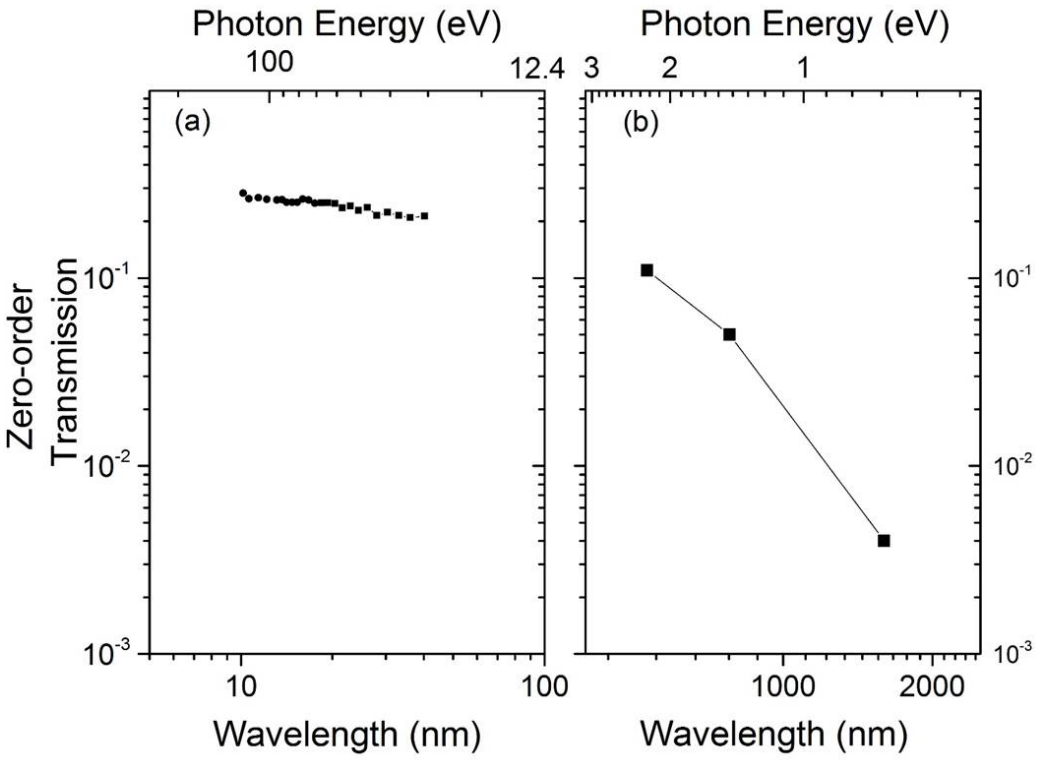

Figure 7.12 The zero-order transmission of the MCP for (a) XUV photons and (b) visible or longer wavelengths. The red line in (a) is the transmission measured with a 300 nm Zr filter and a 300 nm Al filter.

Since only the zero-order of the transmission is used for the attosecond applications, one would not expect any degradation of the spatial or temporal properties of the XUV pulses. To confirm this judgment, a RABITT (Reconstruction of Attosecond Beating By Interference of Two-photon Transitions) scan with an attosecond pulse train was done with and without the MCP filter, as shown in Fig. 7.13 (a) below [42], [99]. Similar to the attosecond streaking, a RABBITT measurement involves an attosecond pulse train and a weak IR beam that are temporally and spatially overlapped, and the photoelectrons generated by the attosecond pulse train can absorb or emit one IR photon energy. Experimentally this means a sideband can be observed in addition to discrete harmonic from the attosecond pulse train. The relative temporal

(delay) position of the sideband maximum on a RABITT spectrogram is determined by the phase difference between the two adjacent odd harmonic orders. More details about RABITT can be found in Chapter 4.1. The delay-dependent signal of the sideband contains the spectral phase information, allowing for the characterization of the attosecond pulses. The black dashed lines in Fig. 7.13 (a) represent the temporal variation for each harmonic order. The slopes determine the group delay of the attosecond pulse train. As can be seen in Fig. 7.13 (b), the group delay are identical for the attosecond pulse trains obtained with and without an MCP filter. This experimental result conclusively demonstrated the dispersion of the attosecond pulse is not affected by the MCP filter. This is a key conclusion for the attosecond community.

The damage threshold is another key factor for the MCP filter to be practically used. In our case, it is difficult to define when the filter is damaged. For example: for a 1 kHz, 750 nm Ti:Sapphire laser, the surface of the MCP shows dark spot several minutes after the incident of laser with peak intensity of 0.2 TW/cm^2. However, the transmission efficiency for the 750 nm laser remained the same even after the surface darkened. This is probably due to the fact that the transmission of the MCP filter only depends on the structure of the multichannel inside the MCP, while the dark spots indicates the surface coating or substrates are damaged. Nevertheless, it is safe to the say that the damage threshold should be at least 0.2 TW/cm^2 for a 1 kHz Ti:Sapphire pump laser. For the same laser but with a 10 Hz repetition rate, the dark spot only shows when the peak intensity reaches 0.6 TW/cm^2. This value is similar to the damage threshold using a Si/SiC plate at Brewster's angle. The latter has been practically used in terawatt-level 10 Hz Ti:Sapphire laser systems for high-flux isolated attosecond pulse generation [100].

To summarize, the comparison of the different schemes of separating the driving pulse and the generated XUV are shown in Table 7.1 and 7.2. The advantages of using MCP filters over other methods can be seen clearly.

Table 7.1 The comparison between different methods for separating the driving laser and the generated XUV from the HHG. (Metallic filter, Annular driving beam, multilayer beam splitter)

	Metallic filter	Conical driving beam	Beam splitter
Damage threshold	Depends on material type	No damage	20 MW/cm^2 at 280 nm
Transmission bandwidth	Al: 20~70 eV ; Zr: 60~200 eV;	No limit	Below 70 eV
GDD	Material GDD	No	Untested
Attenuation of driving pulse	10^{-6} ~ 10^{-7}	0, only use partial energy	1%
XUV transmission	300 nm Al: 60%; 300 nm Zr: 40 %	100%, XUV flux low	40% at 93.3 nm (~ 13 eV)

Table 7.2 The comparison between different methods for separating the driving laser and the generated XUV from the HHG. (Si/SiC plate, Grating pairs, MCP filter)

	Si/SiC plate at Brewster Angle	Grating pair	MCP filter
Damage threshold	0.8 TW/cm^2 (10 Hz, 800 nm laser)	Grazing incident angle	0.6 TW/cm^2 (10 Hz, 750 nm laser)
Transmission bandwidth	Below 120 eV	No limit. Narrow bandwidth	No limit
GDD	No	High due to grating	No
Attenuation of driving pulse	~ 10^{-4}	0	5% for 750 nm, 0.4% for 1.6 μm
XUV transmission	~ 60% at 29.6 nm (~ 42 eV)	20%	Higher than 25 %

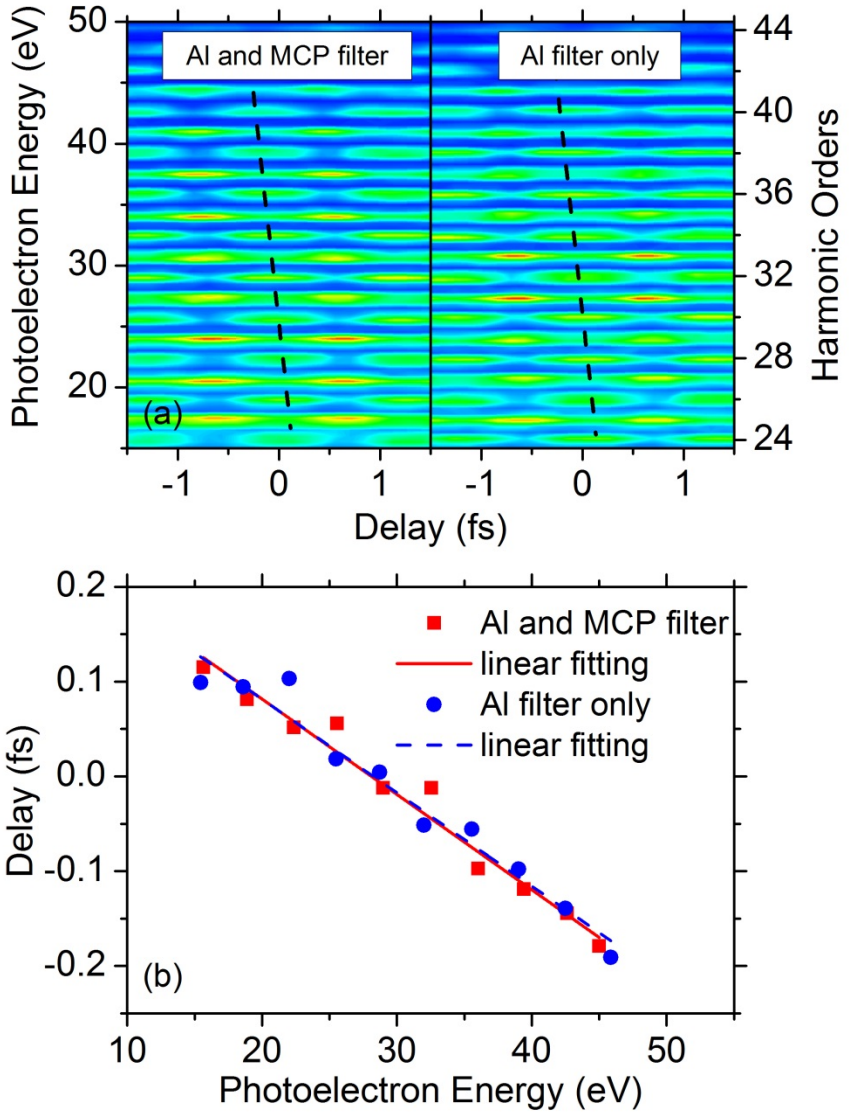

Figure 7.13(a) RABBITT spectrograms with (left) and without (right) MCP filter. (b) The relative delay for sideband maxima as the function of the photoelectron energy. The red squares were taken with Al and MCP filter, and the blue dots were taken with Al filter only. The linear fits for each dataset were plotted in the solid and dashed lines with the same color. (Reprinted from Q Zhang, K. Zhao, J. Li, M. Chini, Y. Cheng, Y. Wu, E. Cunningham, and Z. Chang, "Suppression of Driving Laser in High Harmonic Generation with a Microchannel Plate". Opt. Lett. Vol. **39**, Issue 12, pp. 3670-3673 (2014), http://dx.doi.org/10.1364/OL.39.003670)

CHAPTER 8 CONCLUSIONS AND OUTLOOK

In this thesis, I have presented the generation and characterization of a single isolated 67 as pulse, which is the shortest optical pulse so far. The DOG method was employed to generate a super-broadband continuum spectrum from HHG. The PROOF method was used for ultra-short attosecond pulse characterization. Experimentally, an electron energy spectrometer with high resolution and collection efficiency is built for attosecond streaking experiments. Finally, several important issues regarding a single 25 as pulse have been discussed. The intensity can be improved by using a tight-focus lens, and the bandwidth of the HHG can increase by using a MCP filter to suppressing the remaining driving filed. The resolution of the MBES can be greatly enhanced by placing a pinhole near the entrance of the MBES, leading to the retrieval of the contrast of satellite pulses around the isolated attosecond pulse with 90% accuracy.

For future work, a driving laser centered at longer wavelengths, i.e. a few-cycle mid-infrared femtosecond laser, should be used. As shown in equation 2.9, the cutoff the HHG is proportional to not only peak intensity, but also to the square of the wavelength of the driving laser when the laser intensity is below the saturation intensity [101], [102]. Consequently, at the same intensity level as the current scenario, a cutoff over 200 eV can be easily achieved. More importantly, the attochirp is also inversely proportional to the wavelength. Therefore, using the driving lasers with longer wavelength benefits our goal in both ways.

APPENDIX A: LIST OF PUBLICATIONS

Peer-Reviewed Journal Publications

Q. Zhang, K. Zhao, and Z. Chang, "Determining Time Resolution of Microchannel Plate Detectors for Electron Time-of-Flight Spectrometer", Review of Scientific Instruments 81, 073112, 2010

X. Wang, M. Chini, **Q. Zhang**, K. Zhao, Y. Wu, Dmitry A. Telnov, Shih-I Chu, and Z. Chang, "Mechanism of quasi-phase-matching in a dual-gas multijet array", Physical Review A, 86, pp. 021802, 2012

K. Zhao, **Q. Zhang**, M. Chini, Y. Wu, X. Wang, and Z. Chang, "Tailoring a 67 attosecond pulse through advantageous phase-mismatch", Optics Letters 37(18), pp.3891-3893, 2012

Q. Zhang, K. Zhao, J. Li, M. Chini, Y. Cheng, Y. Wu, E. Cunningham, and Z. Chang, "Suppression of Driving Laser in High Harmonic Generation with a Microchannel Plate", Optics Letters (Accepted)

Q. Zhang, K.Zhao, and Z. Chang, "High resolution electron spectrometers for characterizing the contrast of isolated 25 as pulses", Journal of Electron Spectroscopy and Related Phenomena (Accepted)

Invited Book Chapters

K. Zhao, **Q. Zhang**, M. Chini & Z. Chang, "Route to One Atomic Unit of Time – Development of a Broadband Attosecond Streak Camera", in *Multiphoton Processes and Attosecond Physics* Vol. 125 (eds. K. Yamanouchi & K. Midorikawa), Ch. 19, pg. 109 (Springer, 2012).

Q. Zhang, K. Zhao, M. Chini. Y. Wu and Z. Chang, "Ultrabroadband Coherent Light for Shortest Attosecond Laser Pulse", in The Supercontinuum Laser Source (3rd edition) (to be published)

Conference Presentations

Q. Zhang, K. Zhao, M. Chini, Y. Wu, X. Wang, and Z. Chang, "Generation and characterization of broadband isolated attosecond pulse", American Physical Society, 43rd Annual Meeting of the APS Division of Atomic, Molecular and Optical Physics, June 4-8,2012. (Oral Presentation)

Kun Zhao, **Qi Zhang**, Michael Chini, Sabih D. Khan, Steve Gilbertson, and Zenghu Chang, Isolated 80 as XUV pulses characterized by PROOF, American Physical Society Division of Atomic, Molecular and Optical Physics Annual Meeting, June 13-17, 2011, Atlanta, GA

Q. Zhang, K. Zhao and Z. Chang, "Magnetic-bottle electron spectrometer for measuring 25 as pulses", American Physical Society, 41st Annual Meeting of the APS Division of Atomic, Molecular and Optical Physics Volume 55, Number 5, March 25-29, 2010 (Oral Presentation)

Kun Zhao, Michael Chini, **Qi Zhang**, Steve Gilbertson, Sabih D. Khan, and Zenghu Chang, Isolated 80-Attosecond Pulses Characterized by PROOF, 2010 Attosecond MURI Review (Multidisciplinary University Research Initiative: Attosecond Optical Technology Based on Recollision and Gating), Dec 7, 2010, Orlando, FLChini, M., Wang, H., Mashiko, H., Chen, S., Yun, C., Gilbertson, S. & Chang, Z. Interferometric Delay Control in Attosecond Streaking Experiments. *2nd International Conference on Attosecond Physics*, Manhattan KS (2009).

Patents

Q. Zhang, K. Zhao and Z. Chang, "Microchannel Plate as an effective filter for suppressing infrared light in High-order Harmonic beams", US patent, (2014, pending)

APPENDIX B: COPYRIGHT PERMISSION

From: Qi Zhang
To: rights@aip.org
Cc:
Subject: copyright request
Sent: Mon 6/2/2014 3:56 PM

Dear editor:

My name is Qi Zhang. I am finishing my doctoral thesis at University of Central Florida with title “Generation and Characterization of single isolated sub-70 attosecond pulse”.
I would like to request for permission to reprint in my thesis from the following:

Q. Zhang, K. Zhao, and Z. Chang, "Determining Time Resolution of Microchannel Plate Detectors for Electron Time-of-Flight Spectrometer",. Review of Scientific Instruments **81**, 073112 (2009)

The excerpts to be reprinted includes figure 1-3 and portions of the text.

The requested permission extends to any future revisions and editions of my dissertation, including non-exclusive world rights in all languages. These rights will in no way restrict republication of the material in any other form b you or by others authorized by you.

Your signing of this letter will also confirm that you and your company owns the copyright to the above described material.

If these arrangements meet with your approval, please sign this letter.

Sincerely,

Qi Zhang

PERMISSION GRANTED FOR THE USE REQUESTED ABOVE:

By : _____

Date: _____

From: AIPRights Permissions
To: Qi Zhang
Subject: RE: copyright request
Date: Friday, June 06, 2014 12:00:51 PM
Attachments: image001.png

Dear Dr. Zhang:

Thank you for requesting permission to reproduce material from AIP Publishing LLC publications.

Material to be reproduced:

Figures 1-3 and portions of the text of:
Q. Zhang, K. Zhao, and Z. Chang,
"Determining Time Resolution of Microchannel Plate Detectors for Electron Time-of-Flight Spectrometer"
Review of Scientific Instruments 81, 073112 (2009)

For use in the following manner:

Reproduced in your doctoral thesis for submission to the University of Central Florida.

Permission is granted subject to these conditions:

1. AIP Publishing LLC grants you non-exclusive world rights in all languages and media. This permission extends to all subsequent and future editions of the new work.

2. The following copyright notice must appear with the material (please fill in the information indicated by capital letters):

"Reproduced with permission from [FULL CITATION]. Copyright [PUBLICATION YEAR], AIP Publishing LLC."

When reusing a full article, the copyright notice must be printed on the first page of the reprinted article or book chapter. When reusing figures, photographs, covers, or tables, the notice may appear in the caption, in a footnote, or in the reference list.

In cases where the new publication is licensed under a Creative Commons license, the full copyright notice as stated above must appear with the reproduced material.

3. If the material is published in electronic format, we ask that a link be created pointing back to the abstract of the article on the journal website. This can be accomplished through the use of the article's DOI.
4. This permission does not apply to any materials credited to sources other than the copyright holder.

Please let us know if you have any questions.

Sincerely,
Susann Brailey

Manager, Rights and Permissions
AIP Publishing LLC
1305 Walt Whitman Road
Suite 300
Melville, NY 11747-4300

Tel. +1 516-576-2268
rights@aip.org

From: Qi Zhang [mailto:qizhang@knights.ucf.edu]
Sent: Monday, June 2, 2014 3:56 PM
To: AIPRights Permissions
Subject: copyright request

Dear editor:

My name is Qi Zhang. I am finishing my doctoral thesis at University of Central Florida with title "Generation and Characterization of single isolated sub-70 attosecond pulse".
I would like to request for permission to reprint in my thesis from the following:

Q. Zhang, K. Zhao, and Z. Chang, "Determining Time Resolution of Microchannel Plate Detectors for Electron Time-of-Flight Spectrometer",. Review of Scientific Instruments **81**, 073112 (2009)

The excerpts to be reprinted includes figure 1-3 and portions of the text.

The requested permission extends to any future revisions and editions of my dissertation, including non-exclusive world rights in all languages. These rights will in no way restrict republication of the material in any other form b you or by others authorized by you.

Your signing of this letter will also confirm that you and your company owns the copyright to the above described material.

If these arrangements meet with your approval, please sign this letter.

Sincerely,

Qi Zhang

PERMISSION GRANTED FOR THE USE REQUESTED ABOVE:

By : _____

Date: _____

From: Qi Zhang Sent: Fri 6/6/2014 3:58 PM
To: 'permissionshelpdesk@elsevier.com'
Cc:
Subject: copyright requested

Dear editor:

My name is Qi Zhang. I am finishing my doctoral thesis at University of Central Florida with title "Generation and Characterization of single isolated sub-70 attosecond pulse".
I would like to request for permission to reprint in my thesis from my publications as following:

Zhang, Qi;Zhao, Kun; Chang, Zenghu, "High resolution electron spectrometers for characterizing the contrast of isolated 25 as pulses", Journal of Electron Spectroscopy and Related Phenomena vol. 195 p. 48-54 (2014)

The excerpts to be reprinted includes figures and portions of the text.

The requested permission extends to any future revisions and editions of my dissertation, including non-exclusive world rights in all languages. These rights will in no way restrict republication of the material in any other form b you or by others authorized by you.

Your agree of this letter will also confirm that you and your company owns the copyright to the above described material.

If these arrangements meet with your approval, please confirm by replying this email.

Sincerely,

Qi Zhang

Regards

Qi

/O=EXCHANGELABS/OU=EXCHANGE ADMINISTRATIVE GROUP (FYDIBOHF23SPDLT)/CN=RECII

From: Stingelin, Laura E. (ELS-PHI) <L.Stingelin@elsevier.com>
Sent: Tuesday, June 10, 2014 2:51 PM
To: Qi Zhang
Subject: RE: copyright requested

Dear Qi,

Permission is covered by the rights you retain as an Elsevier journal author as outlined at http://www.elsevier.com/journal-authors/author-rights-and-responsibilities, which include Inclusion in a thesis or dissertation, provided that proper acknowledgement is given to the original source of publication. Should you require any further clarification, please let me know.

Best of luck with your thesis.

Thank you,
Laura

Laura Stingelin
Permissions Helpdesk Associate
Elsevier
1600 John F. Kennedy Boulevard
Suite 1800
Philadelphia, PA 19103-2899
T: (215) 239-3867
F: (215) 239-3805
E: l.stingelin@elsevier.com
Questions about obtaining permission: whom to contact? What rights to request?
When is permission required? Contact the Permissions Helpdesk at:
+1-800-523-4069 x 3808 *permissionshelpdesk@elsevier.com*

From: Qi Zhang [mailto:qizhang@knights.ucf.edu]
Sent: Friday, June 06, 2014 3:58 PM
To: Permissions Helpdesk
Subject: copyright requested

Dear editor:

My name is Qi Zhang. I am finishing my doctoral thesis at University of Central Florida with title "Generation and Characterization of single isolated sub-70 attosecond pulse".
I would like to request for permission to reprint in my thesis from my publications as following:

Zhang, Qi;Zhao, Kun; Chang, Zenghu, "High resolution electron spectrometers for characterizing the contrast of isolated 25 as pulses", Journal of Electron Spectroscopy and Related Phenomena vol. 195 p. 48-54 (2014)

The excerpts to be reprinted includes figures and portions of the text.

The requested permission extends to any future revisions and editions of my dissertation, including non-exclusive world rights in all languages. These rights will in no way restrict republication of the material in any other form b you or by others authorized by you.

Your agree of this letter will also confirm that you and your company owns the copyright to the above described material.

If these arrangements meet with your approval, please confirm by replying this email.

Sincerely,

Qi Zhang

Regards

Qi

ELSEVIER LICENSE
TERMS AND CONDITIONS

Jun 06, 2014

This is a License Agreement between Qi Zhang ("You") and Elsevier ("Elsevier") provided by Copyright Clearance Center ("CCC"). The license consists of your order details, the terms and conditions provided by Elsevier, and the payment terms and conditions.

All payments must be made in full to CCC. For payment instructions, please see information listed at the bottom of this form.

Supplier	Elsevier Limited The Boulevard,Langford Lane Kidlington,Oxford,OX5 1GB,UK
Registered Company Number	1982084
Customer name	Qi Zhang
Customer address	4000 Central Florida Blvd ORLANDO, FL 32816
License number	3403240094260
License date	Jun 06, 2014
Licensed content publisher	Elsevier
Licensed content publication	Journal of Electron Spectroscopy and Related Phenomena
Licensed content title	High resolution electron spectrometers for characterizing the contrast of isolated 25 as pulses
Licensed content author	Qi Zhang,Kun Zhao,Zenghu Chang
Licensed content date	August 2014
Licensed content volume number	195
Licensed content issue number	None
Number of pages	7
Start Page	48
End Page	54
Type of Use	reuse in a thesis/dissertation
Portion	figures/tables/illustrations
Number of figures/tables/illustrations	8
Format	both print and electronic
Are you the author of this Elsevier article?	Yes

Will you be translating?	No
Title of your thesis/dissertation	GENERATION AND CHARACTERIZATION OF SUB-70 ISOLATED ATTOSECOND PULSE
Expected completion date	Jul 2014
Estimated size (number of pages)	150
Elsevier VAT number	GB 494 6272 12
Permissions price	0.00 USD
VAT/Local Sales Tax	0.00 USD / 0.00 GBP
Total	0.00 USD
Terms and Conditions	

INTRODUCTION

1. The publisher for this copyrighted material is Elsevier. By clicking "accept" in connection with completing this licensing transaction, you agree that the following terms and conditions apply to this transaction (along with the Billing and Payment terms and conditions established by Copyright Clearance Center, Inc. ("CCC"), at the time that you opened your Rightslink account and that are available at any time at http://myaccount.copyright.com).

GENERAL TERMS

2. Elsevier hereby grants you permission to reproduce the aforementioned material subject to the terms and conditions indicated.

3. Acknowledgement: If any part of the material to be used (for example, figures) has appeared in our publication with credit or acknowledgement to another source, permission must also be sought from that source. If such permission is not obtained then that material may not be included in your publication/copies. Suitable acknowledgement to the source must be made, either as a footnote or in a reference list at the end of your publication, as follows:

"Reprinted from Publication title, Vol /edition number, Author(s), Title of article / title of chapter, Pages No., Copyright (Year), with permission from Elsevier [OR APPLICABLE SOCIETY COPYRIGHT OWNER]." Also Lancet special credit - "Reprinted from The Lancet, Vol. number, Author(s), Title of article, Pages No., Copyright (Year), with permission from Elsevier."

4. Reproduction of this material is confined to the purpose and/or media for which permission is hereby given.

5. Altering/Modifying Material: Not Permitted. However figures and illustrations may be altered/adapted minimally to serve your work. Any other abbreviations, additions, deletions and/or any other alterations shall be made only with prior written authorization of Elsevier Ltd. (Please contact Elsevier at permissions@elsevier.com)

6. If the permission fee for the requested use of our material is waived in this instance, please be advised that your future requests for Elsevier materials may attract a fee.

/O=EXCHANGELABS/OU=EXCHANGE ADMINISTRATIVE GROUP (FYDIBOHF23SPDLT)/CN=RECII

From: pubscopyright <copyright@osa.org>
Sent: Tuesday, June 10, 2014 4:30 PM
To: Qi Zhang
Subject: RE: copyright permission for disseration

Dear Qi Zhang,

Thank you for contacting The Optical Society.

Because you are the author of the source paper from which you wish to reproduce material, OSA considers your requested use of its copyrighted materials to be permissible within the author rights granted in the Copyright Transfer Agreement submitted by the requester on acceptance for publication of his/her manuscript. It is requested that a complete citation of the original material be included in any publication. This permission assumes that the material was not reproduced from another source when published in the original publication.

Please let me know if you have any questions.

Kind Regards,

Susannah Lehman

Susannah Lehman
June 10, 2014
Authorized Agent, The Optical Society

From: Qi Zhang [mailto:qizhang@knights.ucf.edu]
Sent: Thursday, June 05, 2014 9:35 PM
To: pubscopyright
Subject: copyright permission for disseration

Dear editor:

My name is Qi Zhang. I am finishing my doctoral thesis at University of Central Florida with title "Generation and Characterization of single isolated sub-70 attosecond pulse".
I would like to request for permission to reprint in my thesis from my publications as following:

Kun Zhao, Qi Zhang, Michael Chini, Yi Wu, Xiaowei Wang, and Zenghu Chang, "Tailoring a 67 attosecond pulse through advantageous phase-mismatch" Optics Letters, **37**(18), 3891. (2001) doi:10.1364/OL.37.003891

Qi Zhang, Kun Zhao, Jie Li, Michael Chini, Yan Cheng, Yi Wu, Eric Cunningham, and Zenghu Chang, "Suppression of Driving Laser in High Harmonic Generation with a Microchannel Plate", accepted manuscript ID 206119.

The excerpts to be reprinted includes figures and portions of the text.

1

The requested permission extends to any future revisions and editions of my dissertation, including non-exclusive world rights in all languages. These rights will in no way restrict republication of the material in any other form b you or by others authorized by you.

Your agree of this letter will also confirm that you and your company owns the copyright to the above described material.

If these arrangements meet with your approval, please confirm by replying this email.

Sincerely,

Qi Zhang

LIST OF REFERENCES

[1] T. H. MAIMAN, “Stimulated Optical Radiation in Ruby,” *Nature*, vol. 187, no. 4736, pp. 493–494, Aug. 1960.

[2] A. Schawlow and C. Townes, “Infrared and Optical Masers,” *Phys. Rev.*, vol. 112, no. 6, pp. 1940–1949, Dec. 1958.

[3] A. E. Siegman, *Lasers*. University Science Books, 1986.

[4] *Light and Its Uses*. Scientific American, 1974, pp. 40 – 43.

[5] O. Albert, H. Wang, D. Liu, Z. Chang, and G. Mourou, “Generation of relativistic intensity pulses at a kilohertz repetition rate,” *Opt. Lett.*, vol. 25, no. 15, p. 1125, Aug. 2000.

[6] K. Zhao, Q. Zhang, M. Chini, Y. Wu, X. Wang, and Z. Chang, “Tailoring a 67 attosecond pulse through advantageous phase-mismatch,” *Opt. Lett.*, vol. 37, no. 18, p. 3891, Sep. 2012.

[7] E. Goulielmakis, M. Schultze, M. Hofstetter, V. S. Yakovlev, J. Gagnon, M. Uiberacker, A. L. Aquila, E. M. Gullikson, D. T. Attwood, R. Kienberger, F. Krausz, and U. Kleineberg, “Single-Cycle Nonlinear Optics,” *Science (80-.).*, vol. 320, p. 1614, 2008.

[8] P. Nuernberger, G. Vogt, T. Brixner, and G. Gerber, “Femtosecond quantum control of molecular dynamics in the condensed phase.,” *Phys. Chem. Chem. Phys.*, vol. 9, no. 20, pp. 2470–97, May 2007.

[9] O. Gessner, A. M. D. Lee, J. P. Shaffer, H. Reisler, S. V Levchenko, A. I. Krylov, J. G. Underwood, H. Shi, A. L. L. East, D. M. Wardlaw, E. T. H. Chrysostom, C. C. Hayden, and A. Stolow, “Femtosecond multidimensional imaging of a molecular dissociation.,” *Science*, vol. 311, no. 5758, pp. 219–22, Jan. 2006.

[10] P. H. Bucksbaum, “Chemistry. The first femtosecond in the life of a chemical reaction.,” *Science*, vol. 312, no. 5772, pp. 373–4, Apr. 2006.

[11] F. Seifert, V. Petrov, and M. Woerner, “Solid-state laser system for the generation of midinfrared femtosecond pulses tunable from 3.3 to 10 microm.,” *Opt. Lett.*, vol. 19, no. 23, pp. 2009–11, Dec. 1994.

[12] A. H. Zewail, “Laser femtochemistry.,” *Science*, vol. 242, no. 4886, pp. 1645–53, Dec. 1988.

[13] G. Krauss, S. Lohss, T. Hanke, A. Sell, S. Eggert, R. Huber, and A. Leitenstorfer, “Synthesis of a single cycle of light with compact erbium-doped fibre technology,” *Nat. Photonics*, vol. 4, no. 1, pp. 33–36, Dec. 2009.

[14] M. Yamashita, K. Yamane, and R. Morita, “Quasi-automatic phase-control technique for chirp compensation of pulses with over-one-octave bandwidth-generation of few- to mono-cycle optical pulses,” *IEEE J. Sel. Top. Quantum Electron.*, vol. 12, no. 2, pp. 213–222, Mar. 2006.

[15] M. Hentschel, R. Kienberger, C. Spielmann, G. A. Reider, N. Milosevic, T. Brabec, P. Corkum, U. Heinzmann, M. Drescher, and F. Krausz, “Attosecond metrology.,” *Nature*, vol. 414, no. 6863, pp. 509–13, Nov. 2001.

[16] F. Frank, C. Arrell, T. Witting, W. a Okell, J. McKenna, J. S. Robinson, C. a Haworth, D. Austin, H. Teng, I. a Walmsley, J. P. Marangos, and J. W. G. Tisch, “Invited review article: technology for attosecond science.,” *Rev. Sci. Instrum.*, vol. 83, no. 7, p. 071101, Jul. 2012.

[17] Z. Chang and P. Corkum, “Attosecond photon sources: the first decade and beyond [Invited],” *J. Opt. Soc. Am. B*, vol. 27, no. 11, p. B9, Oct. 2010.

[18] Z. Chang, *Fundamentals of Attosecond Optics*. Boca Raton, Florida: CRC Press, 2011.

[19] S. Nagele, R. Pazourek, J. Feist, K. Doblhoff-Dier, C. Lemell, K. Tőkési, and J. Burgdörfer, “Time-resolved photoemission by attosecond streaking: extraction of time information,” *J. Phys. B At. Mol. Opt. Phys.*, vol. 44, no. 8, p. 081001, Apr. 2011.

[20] J. M. Dahlström, a L’Huillier, and a Maquet, “Introduction to attosecond delays in photoionization,” *J. Phys. B At. Mol. Opt. Phys.*, vol. 45, no. 18, p. 183001, Sep. 2012.

[21] M. F. Kling and M. J. J. Vrakking, “Attosecond electron dynamics.,” *Annu. Rev. Phys. Chem.*, vol. 59, no. November 2007, pp. 463–92, Jan. 2008.

[22] K. Klünder, J. M. Dahlström, M. Gisselbrecht, T. Fordell, M. Swoboda, D. Guénot, P. Johnsson, J. Caillat, J. Mauritsson, a. Maquet, R. Taïeb, and a. L’Huillier, “Probing Single-Photon Ionization on the Attosecond Time Scale,” *Phys. Rev. Lett.*, vol. 106, no. 14, p. 143002, Apr. 2011.

[23] M. Schultze, M. Fiess, N. Karpowicz, J. Gagnon, M. Korbman, M. Hofstetter, S. Neppl, a L. Cavalieri, Y. Komninos, T. Mercouris, C. a Nicolaides, R. Pazourek, S. Nagele, J. Feist, J. Burgdörfer, a M. Azzeer, R. Ernstorfer, R. Kienberger, U. Kleineberg, E. Goulielmakis, F. Krausz, and V. S. Yakovlev, “Delay in photoemission.,” *Science*, vol. 328, no. 5986, pp. 1658–62, Jun. 2010.

[24] E. Goulielmakis, Z.-H. Loh, A. Wirth, R. Santra, N. Rohringer, V. S. Yakovlev, S. Zherebtsov, T. Pfeifer, A. M. Azzeer, M. F. Kling, S. R. Leone, and F. Krausz, "Real-time observation of valence electron motion.," *Nature*, vol. 466, no. 7307, pp. 739–43, Aug. 2010.

[25] H. J. Wörner, J. B. Bertrand, D. V Kartashov, P. B. Corkum, and D. M. Villeneuve, "Following a chemical reaction using high-harmonic interferometry.," *Nature*, vol. 466, no. 7306, pp. 604–7, Jul. 2010.

[26] a L. Cavalieri, N. Müller, T. Uphues, V. S. Yakovlev, a Baltuska, B. Horvath, B. Schmidt, L. Blümel, R. Holzwarth, S. Hendel, M. Drescher, U. Kleineberg, P. M. Echenique, R. Kienberger, F. Krausz, and U. Heinzmann, "Attosecond spectroscopy in condensed matter.," *Nature*, vol. 449, no. 7165, pp. 1029–32, Oct. 2007.

[27] M. Ferray, A. L'Huillier, X. F. Li, L. A. Lompre, G. Mainfray, and C. Manus, "Multiple-harmonic conversion of 1064 nm radiation in rare gases," *J. Phys. B*, vol. 21, p. 31, 1988.

[28] P. Maine, D. Strickland, P. Bado, M. Pessot, and G. Mourou, "Generation of ultrahigh peak power pulses by chirped pulse amplification," *IEEE J. Quantum Electron.*, vol. 24, no. 2, pp. 398–403, Feb. 1988.

[29] D. Strickland and G. Mourou, "Compression of amplified chirped optical pulses," *Opt. Commun.*, vol. 56, no. 3, pp. 219–221, Dec. 1985.

[30] G. Sansone, E. Benedetti, F. Calegari, C. Vozzi, L. Avaldi, R. Flammini, L. Poletto, P. Villoresi, C. Altucci, R. Velotta, S. Stagira, S. De Silvestri, and M. Nisoli, "Isolated single-cycle attosecond pulses.," *Science*, vol. 314, no. 5798, pp. 443–6, Oct. 2006.

[31] H. Mashiko, S. Gilbertson, C. Li, S. D. Khan, M. M. Shakya, E. Moon, and Z. Chang, "Double Optical Gating of High-Order Harmonic Generation with Carrier-Envelope Phase Stabilized Lasers," *Phys. Rev. Lett.*, vol. 100, no. 10, p. 103906, Mar. 2008.

[32] Z. Chang, "Controlling attosecond pulse generation with a double optical gating," *Phys. Rev. A*, vol. 76, p. 051403(R), 2007.

[33] S. Gilbertson, H. Mashiko, C. Li, S. D. Khan, M. M. Shakya, E. Moon, and Z. Chang, "A low-loss, robust setup for double optical gating of high harmonic generation," *Appl. Phys. Lett.*, vol. 92, p. 71109, 2008.

[34] H. Mashiko, S. Gilbertson, M. Chini, X. Feng, C. Yun, H. Wang, S. D. Khan, S. Chen, and Z. Chang, "Extreme ultraviolet supercontinua supporting pulse durations of less than one atomic unit of time," vol. 34, no. 21, pp. 3337–3339, 2009.

[35] P. Corkum, “Plasma perspective on strong field multiphoton ionization,” *Phys. Rev. Lett.*, vol. 71, no. 13, pp. 1994–1997, Sep. 1993.

[36] G. Mainfray and G. Manus, “Multiphoton ionization of atoms,” *Reports Prog. Phys.*, vol. 54, no. 10, pp. 1333–1372, Oct. 1991.

[37] A. Scrinzi, M. Geissler, and T. Brabec, “Ionization Above the Coulomb Barrier,” *Phys. Rev. Lett.*, vol. 83, no. 4, pp. 706–709, Jul. 1999.

[38] L. V. Keldysh, “Ionization in the filed of a strong elecromagnetic wave,” *JETP*, vol. 20, no. 5, p. 1307, 1964.

[39] M. Bellini, C. Lyngå, A. Tozzi, M. Gaarde, T. Hänsch, A. L’Huillier, and C.-G. Wahlström, “Temporal Coherence of Ultrashort High-Order Harmonic Pulses,” *Phys. Rev. Lett.*, vol. 81, no. 2, pp. 297–300, Jul. 1998.

[40] M. Gaarde, F. Salin, E. Constant, P. Balcou, K. Schafer, K. Kulander, and a. L’Huillier, “Spatiotemporal separation of high harmonic radiation into two quantum path components,” *Phys. Rev. A*, vol. 59, no. 2, pp. 1367–1373, Feb. 1999.

[41] K. Varjú, P. Johnsson, T. Remetter, E. Gustafsson, E. Constant, E. Cormier, E. Mével, and A. L. Huillier, “Experimental Studies of Attosecond Pulse Trains,” vol. 15, no. 6, pp. 888–898, 2005.

[42] P. M. Paul, E. S. Toma, P. Breger, G. Mullot, F. Auge, P. Balcou, H. G. Muller, and P. Agostini, “Observation of a train of attosecond pulses from high harmonic generation.,” *Science*, vol. 292, no. 5522, pp. 1689–92, Jun. 2001.

[43] P. Antoine, A. L’Huillier, M. Lewenstein, P. Salières, and B. Carré, “Theory of high-order harmonic generation by an elliptically polarized laser field,” *Phys. Rev. A*, vol. 53, no. 3, pp. 1725–1745, Mar. 1996.

[44] K. Budil, P. Salières, M. Perry, and A. L’Huillier, “Influence of ellipticity on harmonic generation,” *Phys. Rev. A*, vol. 48, no. 5, pp. R3437–R3440, Nov. 1993.

[45] P. B. Corkum, N. H. Burnett, and M. Y. Ivanov, “Subfemtosecond pulses,” *Opt. Lett.*, vol. 19, no. 22, p. 1870, Nov. 1994.

[46] R. Trebino, K. W. Delong, D. N. Fittinghoff, J. N. Sweetser, B. A. Richman, M. A. Krumbu, and D. J. Kane, “REVIEW ARTICLE Measuring ultrashort laser pulses in the time-frequency domain using frequency-resolved optical gating,” vol. 68, no. 9, pp. 3277–3295, 1997.

[47] K. W. DeLong, D. N. Fittinghoff, R. Trebino, B. Kohler, and K. Wilson, “Pulse retrieval in frequency-resolved optical gating based on the method of generalized projections,” *Opt. Lett.*, vol. 19, no. 24, p. 2152, Dec. 1994.

[48] B. Shan, S. Ghimire, and Z. Chang, “Effect of orbital symmetry on high-order harmonic generation from molecules,” *Phys. Rev. A*, vol. 69, no. 2, p. 021404, Feb. 2004.

[49] C. Lyngå, A. L’Huillier, and C.-G. Wahlström, “High-order harmonic generation in molecular gases,” *J. Phys. B At. Mol. Opt. Phys.*, vol. 29, no. 14, pp. 3293–3302, Jul. 1996.

[50] V. T. Platonenko and V. V. Strelkov, “Single attosecond soft-x-ray pulse generated with a limited laser beam,” *J. Opt. Soc. Am. B*, vol. 16, no. 3, p. 435, Mar. 1999.

[51] M. V. Ammosov, N. B. Delone, and V. P. Krainov, “Tunnel ionization of complex atoms and of atomic ions in an alternating electromagnetic field,” *Sov. Phys. JETP*, vol. 64, p. 1191, 1986.

[52] E. Goulielmakis, M. Uiberacker, R. Kienberger, a Baltuska, V. Yakovlev, a Scrinzi, T. Westerwalbesloh, U. Kleineberg, U. Heinzmann, M. Drescher, and F. Krausz, “Direct measurement of light waves.,” *Science*, vol. 305, no. 5688, pp. 1267–9, Aug. 2004.

[53] D. J. Bradley, B. Liddy, and W. E. Sleat, “Direct linear measurement of ultrashort light pulses with a picosecond streak camera,” *Opt. Commun.*, vol. 2, no. 8, pp. 391–395, Jan. 1971.

[54] J. Itatani, F. Quéré, G. L. Yudin, M. Y. Ivanov, F. Krausz, and P. B. Corkum, “Attosecond Streak Camera,” *Phys. Rev. Lett.*, vol. 88, p. 173903, 2002.

[55] R. Kienberger, E. Goulielmakis, M. Uiberacker, A. Baltuska, V. Yakovlev, F. Bammer, A. Scrinzi, T. Westerwalbesloh, U. Kleineberg, U. Heinzmann, M. Drescher, and F. Krausz, “Atomic transient recorder,” *Nature*, vol. 427, p. 817, 2004.

[56] M. Kitzler, N. Milosevic, A. Scrinzi, F. Krausz, and T. Brabec, “Quantum Theory of Attosecond XUV Pulse Measurement by Laser Dressed Photoionization,” *Phys. Rev. Lett.*, vol. 88, no. 17, p. 173904, Apr. 2002.

[57] M. Smolarski, P. Eckle, U. Keller, and R. Dörner, “Semiclassical model for attosecond angular streaking.,” *Opt. Express*, vol. 18, no. 17, pp. 17640–50, Aug. 2010.

[58] Y. Mairesse and F. Quéré, “Frequency-resolved optical gating for complete reconstruction of attosecond bursts,” *Phys. Rev. A*, vol. 71, p. 011401(R), 2005.

[59] K. W. Delong, D. N. Fittinghoff, R. Trebino, B. Kohler, and K. Wilson, “Pulse retrieval in frequency-resolved optical gating based on the method of generalized projections.,” *Opt. Lett.*, vol. 19, no. 24, pp. 2152–4, Dec. 1994.

[60] D. J. Kane, “Principal components generalized projections : a review [Invited] GATING GATING PHASE RETRIEVAL PROBLEM,” vol. 25, no. 6, pp. 120–132, 2008.

[61] M. Chini, S. Gilbertson, S. D. Khan, and Z. Chang, “Characterizing ultrabroadband attosecond lasers.,” *Opt. Express*, vol. 18, no. 12, pp. 13006–16, Jun. 2010.

[62] K. W. Delong, R. Trebino, K. W. Delong, R. Trebino, and S. N. Laboratories, “for frequency-resolved optical gating,” vol. 11, no. 9, pp. 2429–2437, 1994.

[63] M. Chini, H. Mashiko, H. Wang, S. Chen, C. Yun, S. Scott, S. Gilbertson, and Z. Chang, “Delay control in attosecond pump-probe experiments,” *Opt. Express*, vol. 17, p. 21459, 2009.

[64] H. Wang, M. Chini, S. D. Khan, S. Chen, S. Gilbertson, X. Feng, H. Mashiko, and Z. Chang, “Practical issues of retrieving isolated attosecond pulses,” *J. Phys. B At. Mol. Opt. Phys.*, vol. 42, no. 13, p. 134007, Jul. 2009.

[65] M. Chini, H. Wang, S. D. Khan, S. Chen, and Z. Chang, “Retrieval of satellite pulses of single isolated attosecond pulses,” *Appl. Phys. Lett.*, vol. 94, p. 161112, 2009.

[66] P. Kruit and F. H. Read, “Magnetic field paralleliser for 2π electron-spectrometer and electron-image magnifier,” *J. Phys. E*, vol. 16, p. 313, 1983.

[67] A. Matsuda, M. Fushitani, C.-M. Tseng, Y. Hikosaka, J. H. D. Eland, and A. Hishikawa, “A magnetic-bottle multi-electron-ion coincidence spectrometer.,” *Rev. Sci. Instrum.*, vol. 82, no. 10, p. 103105, Oct. 2011.

[68] O. Cheshnovsky, S. H. Yang, C. L. Pettiette, M. J. Craycraft, and R. E. Smalley, “Magnetic time-of-flight photoelectron spectrometer for mass-selected negative cluster ions,” *Rev. Sci. Instrum.*, vol. 58, p. 2131, 1987.

[69] T. Tsuboi, E. Y. Xu, Y. K. Bae, and K. T. Gillen, “Magnetic bottle electron spectrometer using permanent magnets,” *Rev. Sci. Instrum.*, vol. 59, no. 8, p. 1357, 1988.

[70] A. Kothe, J. Metje, M. Wilke, A. Moguilevski, N. Engel, R. Al-Obaidi, C. Richter, R. Golnak, I. Y. Kiyan, and E. F. Aziz, “Time-of-flight electron spectrometer for a broad range of kinetic energies.,” *Rev. Sci. Instrum.*, vol. 84, no. 2, p. 023106, Feb. 2013.

[71] A. M. Rijs, E. H. G. Backus, C. A. de Lange, N. P. C. Westwood, and M. H. M. Janssen, "`Magnetic bottle' spectrometer as a versatile tool for laser photoelectron spectroscopy," *J. Electron Spectrosc.*, vol. 112, p. 151, 2000.

[72] T. Tsuboi, E. Y. Xu, Y. K. Bae, and K. T. Gillen, "Magnetic bottle electron spectrometer using permanent magnets," *Rev. Sci. Instrum.*, vol. 59, p. 1357, 1988.

[73] Q. Zhang, K. Zhao, and Z. Chang, "High resolution electron spectrometers for characterizing the contrast of isolated 25 as pulses," *J. Electron Spectros. Relat. Phenomena*, vol. 195, pp. 48–54, Aug. 2014.

[74] "SATE: Static-field Analysis Toolkit (Educational)." [Online]. Available: http://www.fieldp.com/sate.html. [Accessed: 09-Jun-2014].

[75] "SIMION® Ion and Electron Optics Simulator." [Online]. Available: http://simion.com/. [Accessed: 09-Jun-2014].

[76] D. Kennedy and S. Manson, "Photoionization of the Noble Gases: Cross Sections and Angular Distributions," *Phys. Rev. A*, vol. 5, no. 1, pp. 227–247, Jan. 1972.

[77] Q. Zhang, K. Zhao, and Z. Chang, "Determining time resolution of microchannel plate detectors for electron time-of-flight spectrometers," *Rev. Sci. Instrum.*, vol. 81, p. 73112, 2010.

[78] Z. Chang, A. Rundquist, H. Wang, I. Christov, H. Kapteyn, and M. Murnane, "Temporal phase control of soft-x-ray harmonic emission," *Phys. Rev. A*, vol. 58, no. 1, pp. R30–R33, Jul. 1998.

[79] C. Bourassin-Bouchet, S. de Rossi, J. Wang, E. Meltchakov, a Giglia, N. Mahne, S. Nannarone, and F. Delmotte, "Shaping of single-cycle sub-50-attosecond pulses with multilayer mirrors," *New J. Phys.*, vol. 14, no. 2, p. 023040, Feb. 2012.

[80] R. López-Martens, K. Varjú, P. Johnsson, J. Mauritsson, Y. Mairesse, P. Salières, M. Gaarde, K. Schafer, A. Persson, S. Svanberg, C.-G. Wahlström, and A. L'Huillier, "Amplitude and Phase Control of Attosecond Light Pulses," *Phys. Rev. Lett.*, vol. 94, no. 3, p. 033001, Jan. 2005.

[81] D. H. Ko, K. T. Kim, and C. H. Nam, "Attosecond-chirp compensation with material dispersion to produce near transform-limited attosecond pulses," *J. Phys. B At. Mol. Opt. Phys.*, vol. 45, no. 7, p. 074015, Apr. 2012.

[82] D. H. Ko, K. T. Kim, J. Park, J. Lee, and C. H. Nam, "Attosecond chirp compensation over broadband high-order harmonics to generate near transform-limited 63 as pulses," *New J. Phys.*, vol. 12, no. 6, p. 063008, Jun. 2010.

[83] “CXRO X-Ray Interactions With Matter.” [Online]. Available: http://henke.lbl.gov/optical_constants/. [Accessed: 09-Jun-2014].

[84] A. L. Huillier, M. Lewenstein, P. Salieres, and P. Balcou, “High-order harmonic-generation cutoff,” vol. 48, no. 5, pp. 69–72, 1993.

[85] B. Carr and A. L. Huillier, “Influence of atomic density in high-order harmonic generation,” vol. 13, no. 1, pp. 148–156, 1996.

[86] H. Dachraoui, T. Auguste, A. Helmstedt, P. Bartz, M. Michelswirth, N. Mueller, W. Pfeiffer, P. Salieres, and U. Heinzmann, “Interplay between absorption, dispersion and refraction in high-order harmonic generation,” *J. Phys. B At. Mol. Opt. Phys.*, vol. 42, no. 17, p. 175402, Sep. 2009.

[87] D. Descamps, L. Roos, C. Delfin, A. L’Huillier, and C.-G. Wahlström, “Two- and three-photon ionization of rare gases using femtosecond harmonic pulses generated in a gas medium,” *Phys. Rev. A*, vol. 64, no. 3, p. 031404, Aug. 2001.

[88] E. Constant, D. Garzella, P. Breger, E. Mével, C. Dorrer, C. Le Blanc, F. Salin, and P. Agostini, “Optimizing High Harmonic Generation in Absorbing Gases: Model and Experiment,” *Phys. Rev. Lett.*, vol. 82, no. 8, pp. 1668–1671, Feb. 1999.

[89] Y. Tamaki, J. Itatani, M. Obara, and K. Midorikawa, “Optimization of conversion efficiency and spatial quality of high-order harmonic generation,” *Phys. Rev. A*, vol. 62, no. 6, p. 063802, Nov. 2000.

[90] H. Kim, I. Kim, D. Lee, K.-H. Hong, Y. Lee, V. Tosa, and C. Nam, “Optimization of high-order harmonic brightness in the space and time domains,” *Phys. Rev. A*, vol. 69, no. 3, p. 031805, Mar. 2004.

[91] S. Kazamias, F. Weihe, D. Douillet, C. Valentin, T. Planchon, S. Sebban, G. Grillon, F. Augé, D. Hulin, and P. Balcou, “High order harmonic generation optimization with an apertured laser beam,” *Eur. Phys. J. D*, vol. 21, no. 3, pp. 353–359, Dec. 2002.

[92] M. a. Porras, Z. L. Horvath, and B. Major, “On the use of lenses to focus few-cycle pulses with controlled carrier–envelope phase,” *Appl. Phys. B*, vol. 108, no. 3, pp. 521–531, May 2012.

[93] J. Peatross, J. L. Chaloupka, and D. D. Meyerhofer, “High-order harmonic generation with an annular laser beam.,” *Opt. Lett.*, vol. 19, no. 13, pp. 942–4, Jul. 1994.

[94] R. W. Falcone and J. Bokor, “Dichroic beam splitter for extreme-ultraviolet and visible radiation.,” *Opt. Lett.*, vol. 8, no. 1, pp. 21–3, Jan. 1983.

[95] F. Frassetto, P. Villoresi, and L. Poletto, “Beam separator for high-order harmonic radiation in the 3-10 nm spectral region.,” *J. Opt. Soc. Am. A. Opt. Image Sci. Vis.*, vol. 25, no. 5, pp. 1104–14, May 2008.

[96] E. J. Takahashi, H. Hasegawa, Y. Nabekawa, and K. Midorikawa, “High-throughput, high-damage-threshold broadband beam splitter for high-order harmonics in the extreme-ultraviolet region,” *Opt. Lett.*, vol. 29, no. 5, p. 507, 2004.

[97] J. Ladislas Wiza, “Microchannel plate detectors,” *Nucl. Instruments Methods*, vol. 162, no. 1–3, pp. 587–601, Jun. 1979.

[98] Z. Cao, F. Jin, J. Dong, Z. Yang, X. Zhan, Z. Yuan, H. Zhang, S. Jiang, and Y. Ding, “Soft x-ray low-pass filter with a square-pore microchannel plate.,” *Opt. Lett.*, vol. 38, no. 9, pp. 1509–11, May 2013.

[99] H. G. Muller, “Reconstruction of attosecond harmonic beating by interference of two-photon transitions,” *Appl. Phys. B*, vol. 74, no. S1, pp. s17–s21, Apr. 2014.

[100] Y. Wu, E. Cunningham, H. Zang, J. Li, M. Chini, X. Wang, Y. Wang, K. Zhao, and Z. Chang, “Generation of high-flux attosecond extreme ultraviolet continuum with a 10 TW laser,” *Appl. Phys. Lett.*, vol. 102, no. 20, 2013.

[101] B. Shan and Z. Chang, “Dramatic extension of the high-order harmonic cutoff by using a long-wavelength driving field,” *Phys. Rev. A*, vol. 65, no. 1, p. 011804, Dec. 2001.

[102] A. L’Huillier, M. Lewenstein, P. Salières, P. Balcou, M. Ivanov, J. Larsson, and C. Wahlström, “High-order Harmonic-generation cutoff,” *Phys. Rev. A*, vol. 48, no. 5, pp. R3433–R3436, Nov. 1993.